Flexible and Tunable Split Ring Resonators

A thesis submitted in fulfilment of the requirements for the degree of Doctor of Philosophy

Robiatun Adayiah Awang

B.Eng. (Hons), M. Eng. in Communication and Computer, UKM

School of Electrical and Computer Engineering

College of Science Engineering and Health

RMIT University

JUNE 2016

DECLARATION

I certify that except where due acknowledgement has been made, the work is that of the author alone; the work has not been submitted previously, in whole or in part, to qualify for any other academic award; the content of the thesis is the result of work which has been carried out since the official commencement date of the approved research program; any editorial work, paid or unpaid, carried out by a third party is acknowledged; and, ethics procedures and guidelines have been followed.

Robiatun Adayiah Awang

29 November 2016

ACKNOWLEDGEMENTS

The completion of this thesis was impossible without the help and support of many people after the will of Allah. First, I would like to express my gratitude to my senior supervisor Associate Professor Wayne Rowe, for his patient guidance, valuable advice, encouragement and support throughout the duration of my PhD candidature. I would also like to thank my secondary supervisor Associate Professor Sharath Sriram whose supervisory inputs and contributions have been valuable in realizing the goals of this research.

I also wish to extend my appreciation to the current and former researchers and students within the School of Engineering: Dr. Thomas Baum, Dr. Francisco J. Tovar-Lopez, Dr. Mahyar Nasabi, Dr. Kyle Berean, Ms. Sarah Masoumi, Mr. Sipei Zhao, Mr. Xutao Tang, Dr. Ahmad Sabirin Zoolfakar, Dr. Rozina Abdul Rani, Dr. Rosmalini Ab Kadir, Mrs. Norhazlin Khairudin, Mrs. Dharma Aryani, Mrs. Syazilawati Mohamed, Mrs. Yusnira Husaini, Dr. Muhammad Farid Abdul Khalid, Dr. Saidatul Norlyana Azemi, Mrs. Harita Jamil, Mrs. Nurul Hajar Mohd Fuad, Ms. Aditi Upadhyay, Dr. Physhar Yi, Mr. Wei Zhang and Ms. Manal Alsaif for their support, invaluable help and for providing an excellent research atmosphere.

The state-of-the-art equipment and facilities provided by RMIT University, has played a major part in achieving my research goals. As such, I would like to thank the people and technical staff who work hard to keep these facilities operational. Specifically, Mr. David Welch, Mr. Yuxun Cao, Mr. Paul Jones and Ms. Chiping Wu for their technical

expertise and assistance throughout the duration of my candidature.

My research work would not have been possible without the financial support by the Ministry of Higher Education of Malaysia and Universiti Teknologi MARA.

Finally, special thanks to my beloved husband Mr. Norhazly Amit, my son Abdul Mu'iz & Abdul Halim, my understanding mother & parent-in law as well as my family for their endless encouragement, sacrifices, prayers and support in the time of need.

Last but not the least, I would like to thank everybody who was involved directly or indirectly in successful completion of the present work. Thank you so much!

Dedication

To my beloved Abang Ly, Muiz, Halim and Mak, for their love and support.

ABSTRACT

The recent development of flexible electronic technologies has created a strong need for flexible/stretchable electromagnetic (EM) components such as resonators, antennas, filters and oscillators. Flexible electronic technologies require devices and structures to reside on non-planar, conformal and elastic surfaces platform. Thus, an ideal solution is to realise the EM components on flexible/stretchable materials or substrates. The ability to bend and stretch EM components enables a new dimension of manipulating electromagnetic waves and promises new potential functionalities of the devices.

The scope of this PhD research is to investigate microfluidic flexible/tunable liquid metal Split Ring Resonators (SRRs) in elastomeric polymer. A rigid substrate is replaced with an elastomeric substrate Polydimethylsiloxane (PDMS), and the conventional metal conductor is substituted with the liquid metal alloy Galinstan. By employing PDMS and liquid metal, it is expected to obtain tunable/stretchable and reversely deformable characteristics in the designed resonators without electrode cracking.

First, a mechanically tolerant fluidic SRR meta-atom that can be stretched, mechanically strained, and reversibly deformed (bent, stretched and twisted) is presented. Applying mechanical deformation to the SRR results in minimal deviation of the transmission response. The frequency response remained within 3% of its original value under strains of up to 18%, 1 cm radius curvatures and 45° degree twisting. This offers a stable and predictable response for flexible electronic applications where mechanical deformation or conformity is inherent.

Second, a fluidic SRR is developed to achieve frequency tunability. A built-in microfluidic channel in between the gaps of the fluidic SRR is employed to harness pneumatic tuning by air injection/suction. A frequency tuning of 3% have been achieved. Further, a contactless and fully integrated PDMS microfluidic sensor based on a meta-atom SRR is proposed for dielectric characterization applications. The integrated microfluidic sensing channel is internally designed through a dual gap SRR as this area provides significantly sensitive to dielectric changes. Thus, exploiting the electric field sensitivity of the devices can be used to predict the dielectric properties of liquid samples. This microfluidic sensor offers a potential lab-on-chip solution for liquid dielectric characterization without external electrical connections.

As PDMS may be limited by its significantly high dielectric loss at microwave frequencies, application flexible composite solution is explored. The challenges associated with creating PDMS-Alumina and PDMS-PTFE composites to form flexible-low loss materials are studied in terms of their structural, mechanical and electrical properties. The incorporation of either low dielectric loss filler in the PDMS matrix (up to 50 wt% filler loading) is shown to reduce the dielectric loss by 25% while maintaining the flexibility of the host matrix. The fillers can also control the permittivity of the composite, either increasing or decreasing the relative permittivity from that of PDMS (~2.7) in the range of 2.4 to 3.7. Such low-loss composites offer a promising solution for flexible microwave substrate applications.

TABLE OF CONTENTS

LIST OF TABLES

Table Number **Page**

LIST OF FIGURES

Figure Number **Page**

LIST OF ABBREVIATIONS AND DEFINITIONS

List of Abbreviations

ε	Dielectric permittivity
PDMS	Polydimethylsiloxane
PMMA	Polymethyl methacrylate
RF	Radio frequency
SEM	Scanning electron microscope
SRRs	Split-ring resonators
tan δ	Loss tangent

List of Definitions

flexible	The material or device can be bent and twisted at different angles and will return to its original state when the altering force is removed.
stretchable	The material or device can be elongated along a particular axis and will return to its original state when the altering force is removed.
tunable	The resonance frequency response of the microwave device can be adjusted by applying an external force.

CHAPTER 1

INTRODUCTION

1.1 MOTIVATION

In recent years, flexible/stretchable electronic systems have gained increasing attention from scientific communities because of their wide variety of applications. Next generation devices such as flexible displays, flexible electromagnetic (EM) devices and interconnects, flexible sensing, energy harvesting and biomedical monitors [1-8] all exploit this advancing technology. To realise these devices, they must be fabricated on lightweight, flexible and/or stretchable substrates/materials, as opposed to the rigid, brittle, and planar materials typically used in electronics. The mechanical flexibility enables new applications previously incompatible with conventionally integrated circuits to be developed. Research in this direction began several decades ago, initially driven by interest in flexible, paper-like displays [6]. Recent work in flexible electronics that have the capability to bend around curved surfaces and create ergonomic designs have potential applications in the biomedical device field [5, 8-10], especially for personal health monitoring systems and bio-inspired device design. The flexible electronic devices must not only bend, but also stretch, compress, twist and deform into curvilinear shapes whilst maintaining their performance.

The revolutionary flexible/stretchable electronic devices of the future [11] are likely to incorporate EM devices into the flexible platform. EM devices such as resonators, antennas, filters and oscillators operating from microwave to terahertz frequencies have been demonstrated in a diverse range of applications. EM metamaterials have also generated a tremendous amount of research interest due to their extraordinary response to electromagnetic waves, such as in the area of cloaking [12, 13], sensing [14-16], lenses [17, 18], concentrators and absorbers [19], and energy harvesting [20].

Metamaterials realised on flexible and stretchable substrates/materials have the ability to bend, twist, stretch, compress, roll and integrate into arbitrary shapes thereby enabling applications that would be impossible offered by the rigid materials. Applying these features to flexible/stretchable EM components adds a new dimension to manipulating electromagnetic radiation and responses. For example, tuning the EM behaviour via mechanical deformation could overcome the limitations of the narrowband frequency operation of metamaterials and control its quality factor. Moreover, in applications related to non-planar/conformal surfaces and moving/vibrating electronic environments, it is advantageous for flexible/stretchable EM device performance to remain stable or only predictably change whilst mechanical deformation is encountered. The split-ring resonator (SRR) is a popular building block of metamaterial-based resonant devices in the microwave regime [21-25]. The microwave frequency range occupies a part of the electromagnetic spectrum extending from 300 MHz to 30 GHz.

The motivation of this research lies in the utilisation of a flexible polymer substrate supporting a mechanically tolerant conductor to realise EM SRRs at microwave frequencies for strain tolerance, tuning and sensing applications. The use of microfluidic technologies is also explored and integrated into the design to reveal interesting engineered electromagnetic responses from the metamaterial-based EM devices.

1.2 THESIS OBJECTIVES AND SCOPE

This study embarks on the following objectives:

1. To realize a fluidic SRR that can efficiently utilize the flexibility of PDMS without significant performance degradation.
2. To study and investigate the efficient microfluidic tuning mechanism using air pressure in a flexible/tunable resonator.
3. To create a microfluidic sensor from an SRR meta-atom for dielectric properties characterization.
4. To conceive a low loss tangent PDMS composite by mixing PDMS with micro/nanoparticles.

1.3 THESIS OUTLINE

This thesis is primarily dedicated to the realisation of flexible meta-atom SRR structures from elastomeric PDMS for strain tolerance, tunability and sensing applications. Mechanical deformation will be used to demonstrate mechanically tolerant SRRs; air pressure will be applied to tune the resonance of a flexible SRR; and an SRR-based sensor for dielectric property characterization will be realised. In conjunction with this, an investigation into the creation of PDMS composites that are more appropriate for

realising flexible microwave circuits is also conducted. An outline of the major sections of this thesis is as follows:

Chapter 2: Several suitable flexible materials to realise the flexible/tunable electromagnetic components are reviewed. Previous and current research related flexible polymer micro-nanocomposites for microwave applications, particularly composites comprised Alumina/PTFE as fillers and PDMS as matrix are examined. An overview of SRRs and their applications is followed by a review of various SRR tuning mechanisms, ranging from substrate deformation to addition of external non-linear components. The application area of microfluidic metamaterial sensors will also be explored.

Chapter 3: This chapter discusses the mechanically tolerant fluidic SRR that can be stretched, mechanically strained, and reversibly deformed (bent, stretched and twisted) without degrading its electrical performance. A conventional microfabrication processes is utilised to realise a patterned SRR on an elastomeric PDMS substrate. The performance of the mechanically tolerant SRR meta-atom is described and validated experimentally.

Chapter 4: The fluidic SRR via microfabrication process is extended to realise frequency tunability and sensing capability in the meta-atom. Fluidic SRRs with a built-in microfluidic channel in between the capacitive gaps are explored to harness tuning by mechanical deformation through air injection/suction. Further, a modified SRR structure is investigated to demonstrate dielectric characterization of fluids through EM sensing.

Chapter 5: This chapter presents a method for reducing dielectric loss (tan δ) of the polymeric substrate material by forming PDMS composites loaded with various concentrations of either alumina (Al2O3) or polytetrafluoroethylene (PTFE) particles. The structural, mechanical and electrical properties of the composites are also investigated. Such low-loss composites offer a promising material system for flexible microwave substrate applications.

Chapter 6: The final chapter presents concluding remarks and possibilities for areas of future research.

1.4 LIST OF PUBLICATIONS

A list of journal and conference publication arising from this research is presented below:

Journals:

J1: **R. A. Awang**, T. Baum, K. J. Berean, P. Yi, K. Kalantar-zadeh, S. Sriram, W. S. T. Rowe, "Elastomeric Composites for Flexible Microwave Substrates", Journal of Applied Physics, vol. 119, pp. 124109, 2016.

J2: P. Yi, **R. A. Awang**, W. S. T. Rowe, K. Kalantar-zadeh and K. Khoshmanesh, "PDMS Nanocomposites for Heat Transfer Enhancement in Microfluidic Platforms," Lab on a Chip, vol. 14, pp. 3419-3426, 2014.

J3: **R. A. Awang**, T. Baum, M. Nasabi, S. Sriram, W. S. T. Rowe, "Mechanically Tolerant Fluidic Split Ring Resonators", Smart Materials and Structures, vol. 25, pp. 075023, 2016.

J4: **R. A. Awang**, F. J. Tovar-Lopez, T. Baum, S. Sriram, W. S. T. Rowe, "Fully Integrated Microfluidic Sensor for Liquid Dielectric

Characterisation", Submitted to Sensors Journal, IEEE.

Conferences:

C1: R. A. Awang, T. Baum, S. Sriram, W. S. T. Rowe "Dielectric Measurements of PDMS composites at X-Band Frequencies", Australian Microwave Symposium, (AMS), 2014.

1.5 ORIGINAL SCIENTIFIC CONTRIBUTION

This thesis has contributed a significant amount of information to the field of flexible fluidic SRRs operating at microwave frequencies. In addition, this research contributed to the development of PDMS micro/nanocomposites for microwave applications. A summary of the contribution to the body of knowledge is listed below:

- A mechanically tolerant fluidic meta-atom SRR is presented, which exhibits no significant change of transmission coefficient and resonant frequency under bending, stretching, twisting and reversible deformation experiments [J3]. A maximum recorded frequency shifts of less than ~3% for all cases was recorded. Thus the proposed SRR is well suited to applications with non-planar/conformal surfaces, and/or moving/vibrating flexible electronic environments that require elements to withstand mechanical strain whilst maintaining electrical performance.
- A fluidic SRR meta-atom which is tunable via air injection/suction is reported. A resonant frequency tuning of 3% was observed from a small deflection in the SRR gap. A fully integrated PDMS sensor is proposed for dielectric characterization applications [J4]. The SRR meta-atom sensor contains a built-in microfluidic sensing channel which traverses through a dual gap SRR,

providing significant sensitivity to dielectric changes. No additional external microwave connections are required, unlike other reported research. The sensor system offers contactless, reusable, non-invasive, label-free sensing solution that has the potential to be implemented in a lab-on-a-chip system.

- A comprehensive study of flexible PDMS/Alumina and PDMS/PTFE composites is presented, analysing their structural, dielectric and mechanical properties [J1, J2, C1]. A tailored relative permittivity and reduced dielectric loss can be achieved whilst maintaining flexibility characteristics by utilizing filler concentration up to 50 wt%. For the first time, PTFE is shown to be a capable filler in a PDMS matrix to establishing an elastic, low dielectric loss microwave substrate. Such substrates are a critical foundation for future flexible/stretchable microwave circuit and device design.

CHAPTER 2

LITERATURE REVIEW

2.1 INTRODUCTION

Flexible/stretchable EM components are receiving significant attention from the research groups due to their tremendous potential to enhance the emerging field of flexible electronics. In conventional electromagnetic component design, rigid materials like solid metals for conductors and rigid dielectric materials for mechanical support are used [26-29]. However, these stiff substrates have undesirable mechanical properties when it comes to their application to flexible electronics systems. This is especially the case when the structures must conform to a complex surface topology or where dynamic bending and stretching is required. Therefore, flexible materials/substrates are necessary to achieve full conductivity, functionality and mechanical stretchability of the devices.

Each material/substrate has a unique set of electromagnetic characteristics that are dependent on its dielectric properties, such as loss tangent and permittivity. Accurate measurements of these properties provide scientists and engineers with valuable information which can be incorporated into its intended application for more accurate designs. It is important to note that these properties change with frequency and variations in the material composition. Hence, suitable flexible material/substrate with having significant low dielectric losses are required to realise the selected flexible/tunable electromagnetic components.

Various flexible EM components such as resonators, antennas, absorbers and filters [30-34] are being studied at microwave frequencies using concepts derived from the metamaterials field. Metamaterials are artificially created materials composing of sub-wavelength resonant elements which can manipulate an electromagnetic field. The advantage of metamaterials over natural materials is the ability to engineer and tune their properties as desired, which depends on its structural size and arrangement. Significant effort has been devoted to demonstrate this concept with existing structures from microwave to optical frequency ranges, for potential applications such as sensing, cloaking, super-lensing and switching [17, 18, 35, 36]. The split-ring resonator (SRR) is a popular fundamental building block of many metamaterial-based resonant devices in the microwave regime [30, 37, 38]. However, these resonant devices often have a limited bandwidth, thus implying the demand for further research on dynamically tuning of their frequency response.

2.2 FLEXIBLE MATERIALS FOR ELECTROMAGNETIC COMPONENTS

A large amount of research has been focussed on using flexible materials to demonstrate diverse electromagnetic components operating from microwave to optical frequencies. Key features of an ideal flexible microwave material are having an excellent mechanical flexibility and also low dielectric loss properties. Flexible materials play a very important role in demonstrating resonant frequency tunability of electromagnetic components through their natural ability to response with mechanical deformation. Low dielectric loss properties are essential to provide maximum signal transmission through materials, or to propagate along electromagnetic structures.

2.2.1 Flexible substrates

Over the past few decades, the core advancements in electronics devices relied on semiconductor materials, especially using a silicon wafer. A silicon wafer is brittle and rigid material. However, silicon in other form such as nanoscale ribbons, wires, or membranes are flexible [11, 39]. Generally, any material in sufficiently thin form is flexible and its flexibility decreases linearly with thickness. Unfortunately, this material is still expensive, thus limits its usage.

Polymers such as silicone rubber, butyl rubber and fluoro-polymer are a preferred substrate material in many microwave and electronic applications mainly due to their flexible nature and low cost. A wide range of flexible polymers with varying mechanical and electrical properties have been investigated to realise flexible devices, including Kapton polyimide [40-42], polyethylene naphthalate (PEN) [43, 44] and polydimenthylsiloxane (PDMS) [45, 46]. These flexible polymers can be easily processed using standard spin-coating and curing procedures as well as other well-established microfabrication techniques, realising a substrate suitable for electromagnetic components.

Among of these polymers, PDMS is particularly attractive as a flexible substrate, as it offers advantages of fabrication ease, biocompatibility, excellent flexibility and controlled elasticity properties [47, 48]. PDMS possesses superior mechanical elasticity (up to ~120% stretchability) [47, 49], makes it a promising substrate for tuning applications through mechanical deformation. Additionally, it has a very low Young's modulus compared to Kapton polyimide and PEN [49] which can retain higher

mechanical strain with excellent reversible and repeatable deformity. Thus, it is well suited to be incorporated with non-planar/conformal surfaces, crucial properties for sensing applications. Furthermore, it has been extensively used in microfluidic-based devices [50, 51] and bio-sensing areas [52, 53] due to its biocompatibility. A detailed explanation on microfluidic tuning is presented in Section 2.4.3. The aforementioned attributes make PDMS a suitable substrate for designing flexible/tunable electromagnetic devices. PDMS has been extensively used to fabricate stretchable microwave devices like resonators, antennas, switches, filters and oscillators [1, 45, 54].

2.2.2 Polymer-composites materials

It is very difficult to identify a homogeneous material which possesses flexibility and at the same time offer low-loss electromagnetic properties. Polymer-ceramic composites are commonly proposed as a solution, as most polymers offer excellent flexibility at low cost, while several ceramics have low dielectric loss properties [55-59]. A micro/nano-composite can be created with almost similar mechanical properties to the intrinsic form of its host matrix.

Ceramics are inorganic, non-metallic, often crystalline oxide, nitride or carbide materials. Many researchers have studied the effects of ceramic filler materials such as SiO_2 [58-60], MgO [61], Al_2O_3 [55, 61, 62], TiO_2 [58], $MgTiO_3$ [56, 63], TeO_2 [64], BZT [65] and $CaTiO_3$ [66] for dielectric substrate applications. These ceramics are commonly used owing to their variety dielectric constant and significantly low loss tangent. Hence controlled mixtures with the polymer of choice can be exploited to tailor the permittivity of the formed composite, generally to higher values.

The challenges associated with creating polymer-ceramic composites to form flexible-low loss materials often stem from inhomogeneous distribution of the fillers within the polymer host-matrix, and compatibility between the fillers and the polymer [67]. PDMS polymer nanocomposites have also been employed for many other diverse functions and applications [68-71]. In general, the dielectric properties of the composite depend on structure, size, morphology and concentration of filler loadings [60, 62]. However, pure PDMS exhibits considerable dielectric loss at microwave frequencies which limits its application as a flexible dielectric material.

Numerous other polymer-ceramic composites have been reported to demonstrate flexible substrates [54, 56, 57, 61, 62, 66, 72]. Koulouridis et al. presented flexible substrates for antenna and filter design at microwave frequencies made from composites of PDMS and various ceramic powders, namely barium titanate (BT: $BaTiO_3$), Mg-Ca-Ti (MCT), and Bi-Ba-Nd-titanate (BBNT) [54]. At 1 GHz, the loss tangent of the BT/PDMS composite was comparatively higher (tan δ of 0.04) than the loss tangent of MCT/PDMS and BBNT/PDMS composites (tan δ <0.009) for 0.25 volume fraction of the ceramic. A microwave antenna and filter were constructed using the developed composites. However, the structural performance of these composites has not been quantified.

Namitha et al. recently studied the effect of particles size on the microwave properties of silicone rubber-alumina composites [62]. Nano-size Al_2O_3 (alumina) fillers were shown to produce increasingly higher dielectric loss with respect to the filler loading, which contradicts perceived trends about such mixtures. The increment of dielectric loss was reported to be due to higher moisture contents and the large interface area of

the nano-alumina particles. In addition, the nano-size alumina-filled silicone rubber composite produced better mechanical properties than micro-sized alumina fillers. However, the investigation is limited to a relatively low volume fraction (0.05%) of nano-alumina filler due to issues with the mixing process for higher filler loadings.

Polytetrafluoroethylene (PTFE) has been extensively used as matrix polymer and mixed with several ceramic fillers to form microwave dielectric composites [56, 61, 66]. A comparison of alumina- and magnesia-filled PTFE composites in terms of dielectric, structural, microstructure and moisture absorption properties was reported by Murali *et al.* [61]. Alumina and magnesia were chosen because of their almost identical dielectric properties. The loss tangent of both composites also showed an increasing trend with respect to filler loading up 60 wt%, with PTFE/magnesia composites exhibiting high loss tangent values compared to the corresponding PTFE/alumina composite. No measurements have been conducted to study the mechanical properties and flexibility of the proposed composites.

2.2.3 Conductive materials

Thin metal films (e.g. gold and silver) have been adhered to flexible substrates to fabricate microwave components such as antennas [73], metamaterials [74] and switches [45]. However, the integration of thin metalllic films with flexible materials leads to the formation of micro-cracks during bending and stretching, which result in electrical open circuits [45, 75]. Thin films of gold deposited on a PDMS substrate have exhibited micro-cracks with lengths in the micrometer range[45] . These films have relatively high electrical resistivity, but are very stretchable/flexible. In [45], a 3 μm gold conductive metal layer was deposited on PDMS substrate to realise a flexible

coplanar waveguide (CPW) for characterizing the broadband RF properties of the PDMS substrate. However conductive metal layer micro cracking increases the electrode resistance, and affects the RF characterization process. Gold strips were fabricated directly on a 1 mm thick PDMS substrate in [46], and a uniform test protocol was followed to observe changes in film structure. An SEM study identified the mechanism of elastic stretchability of the films, and the resulting micro-cracks can be observed in Figure 2.1. Li et al. [74] presented planar arrays of I-shaped resonant elements made up of a thin gold layer encapsulated between two PDMS substrate layers to tackle micro-crack formation. The structures were designed to have full recovery when relaxed, and can be repeatedly deformed without degradation with greater than 8 % of tuning range.

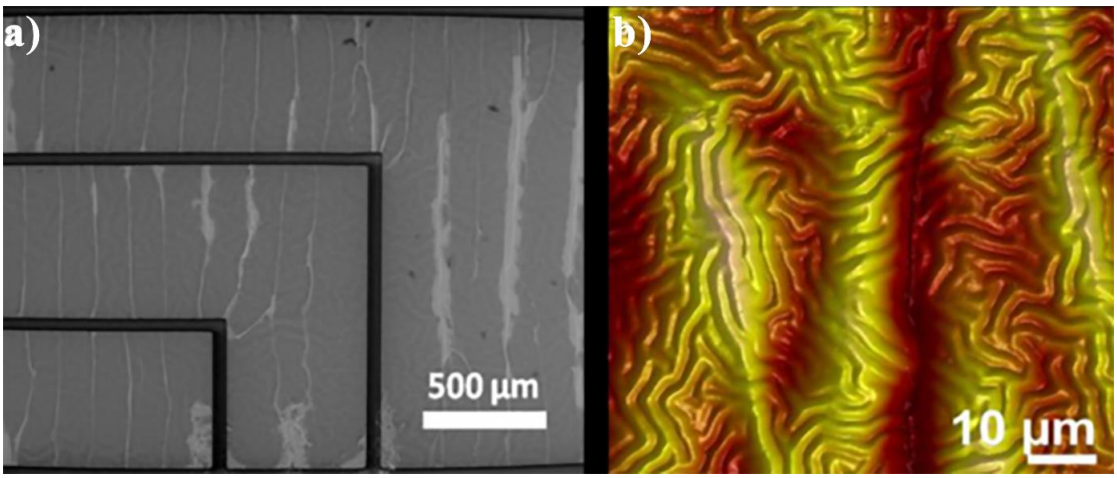

Figure 2.1 : (a) Electron micrograph of micro-cracked morphology, and (b) atomic force microscope scan showing surface micro-cracks [45]. Copyright 2012 IEEE.

Replacing the thin metal film with a fluidic conductor (for example: eutectic gallium indium (EGaIn), Galinstan, or mercury) can be extremely beneficial in alleviating micro-cracking as their liquid nature retains continuous conductivity when deformed.

Recently, EGaIn and Galinstan have been employed due to their high electrical conductivity and low toxicity when compared to mercury [76, 77]. As they are liquids at room temperature, it is possible implement reconfigurable liquid metal components and circuits as examined in the next section.

2.3 FLEXIBLE/STRETCHABLE EM COMPONENTS

Various flexible/stretchable EM components like resonators, antennas, switches, filters and oscillators [1, 45, 54] have been reported for diverse applications especially in the electronics, communications, biomedical and industrial areas. Integrating flexible substrates with fluidic liquid metal as conductor component can be employed in realising flexible/stretchable EM components. Normally, the liquid metals are encapsulated in flexible substrates which resulting tolerance changes caused by external bending/stretching force. For stretchable devices, liquid metals are suitable chosen materials because they will not forming micro-cracks when stretched repeatedly and also exhibited some self-healing properties [78].

Stretchable RF devices have been proposed using liquid metal to alleviate the rigidity issue of the metallic layer [78, 79]. So *et al.* [78] presented a fluidic dipole antenna. The liquid metal alloy EGain is injected into PDMS microfluidic channel. The fluidic antenna was mechanically tunable, reversibly deformable and sensitive to strain. Thus, it is suitable to be implemented as a strain sensor. A flexible liquid metal alloy (EGaIn) microstrip patch antenna with multi-layer construction was developed by Hayes *et al.* [79] for conformal applications. The patch antenna showed good performance when conformed to a curved surface. However no stretching, twisting, or other deformation mode investigations were performed to determine its suitability for a wide range of flexible electronic applications. Flexible antennas with some degree of mechanical

tolerance have also been presented in [31, 32]. Cheng *et al.* [32] presented a foldable and stretchable planar inverted cone antenna (PICA) operating at frequency ranges of 3.1-10.6 GHz for ultrawideband (UWB) applications. The antenna can be folded, twisted and stretched up to 40% along any axis without inducing any mechanical damage. Huang *et al.* [31] proposed serpentine antennas for mechanically adaptive frequency modulation. The antenna can be deformed (bending, stretching and twisting) whilst the resonance frequency showed a stable response in up to 50% applied strain.

As antennas are only a small subset of RF components, an analysis of mechanically tolerant generic RF building blocks is desired. Liu *et al.* investigated a flexible single element SRR as one such building block [30]. However this work focused on tunability rather than tolerance, and was restricted to mechanical stretching. By stretching the single element SRR, the resonance frequency can be tuned continuously over more than 70% of the whole X-band frequency range. The study describes a simple building block for realizing mechanically tunable metamaterials. Filters design [80, 81] based on liquid metals have been proposed to make them switchable or tunable, but flexibility was not the main focus. In [80], a tunable coupled SRR bandpass filters is presented by altering the length of the resonator through a flowing liquid metal which causing frequency changes. Khan *et al.* [81] proposed a fluidic microstrip open stub resonator bandstop filter. The frequency can be tuned by applying a certain pressure to achieve a desired physical length of the open stub. The open stub remains fixed with releasing the given pressure, thus the device also can perform as a pressure sensor.

2.4 TUNING MECHANISMS

In many electromagnetic devices, especially in metamaterial applications, the resonance of constituent elements exhibits a narrowband frequency response. A common technique to overcome this problem is to introduce a tunable narrowband response to extend the frequency coverage. Several tuning approaches have been proposed, and a review of these is presented in the following sections grouped according to their overarching operational mechanism.

2.4.1 External devices

Introducing external devices like capacitors, varactors and radio frequency micro electromechanical systems (RF MEMS) into a resonator element has been proposed to tune the frequency response. A simple resonator is often loaded with a variable element in the existing resonator loop [82, 83]. The resonant frequency can be tuned by changing the values of the loaded capacitor as shown in Figure 2.2 (a). A varactor diode positioned across the gap of a resonator can achieve desired frequency tuning by adjusting the bias voltage [84-88]. Normally, this method usually attains a wide range frequency tunability. For example, Nesimoglu *et. al* [87] proposed a varactor diode to tune metamaterial S-shaped resonator up to 28%. In [88], Zhu *et. al* presented 31% tunability of SRR antenna at low frequency as shown in Figure 2.2 (b). However, the presence of varactors device in the resonator introduces biasing circuitries into the structure resulting in additional losses/reflections/coupling. Moreover, it will interfere with the RF signal and can limit the performance of the resonators. Furthermore, this also leads to the fabrication complexity and scalability limitations.

RF-MEMS components incorporated into EM devices to achieve frequency tunability has also been demonstrated [89-91]. As in Figure 2.2 (c), Bouyge *et. al* [89] presented a SRR-based bandstop filter which can digitally control bandwidth due to frequency shift by on-off state of RF MEMS switches. In [91], RF MEMS cantilevers controlled antenna radiation patterns by ± 30 degrees with a fixed frequency band. A metamaterial filter is electrostatically actuated by moving up or down a cantilever RF-MEMS bridge capacitor as in [90] causing a large frequency tunability. Despite of having a very fast switching speed, fabrication of RF-MEMS is quite complex especially for the case of metamaterial arrays which a huge number of RF MEMS is required.

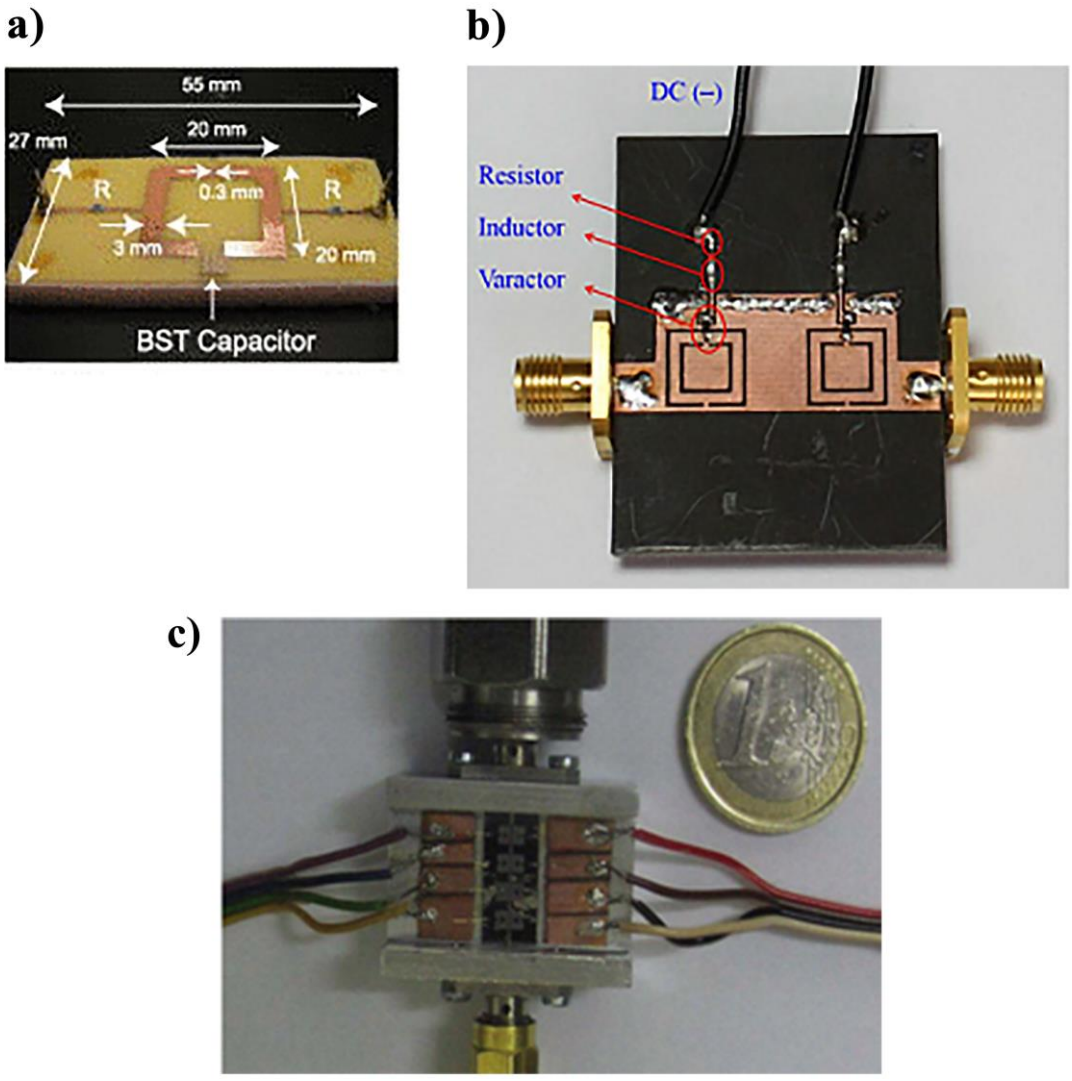

Figure 2.2 : Tuning by the external devices. (a) SRR capacitor loaded [83], (b) Varactor diode [84] and (c) RF MEMS switches [89]. Copyright 2007, 2010 IEEE; Copyright 2013 John Wiley and Sons.

The abovementioned tuning method requires integration with rigid materials, therefore they are not suitable and not fully compatible with flexible electronics systems.

2.4.2 Mechanical/Structural deformation

Another method to realize tunability within resonant electromagnetic components is by utilizing flexible materials/substrates. Flexible substrates are of special interest because

of their natural ability to achieve large frequency tunability through mechanical deformation. A stretching/bending/twisting force placed across the substrate can alter the intra-and/or inter-component capacitance and consequently changes the resonance frequency of the resonator [1, 73, 74, 78].

Figure 2.3 shows a stretchable microstrip patch antenna composed of AgNW/PDMS flexible conductor which has been used to demonstrate mechanically tuning by bending, twisting and rolling. With applied strain of 15%, a ~5% of frequency tuning can be achieved with an excellent reversibility deformability [73]. Liquid metal antennas [1, 78, 79] enclosed in elastomeric microfluidic channels which exhibit tunability via substrate deformation have also been discussed in Section 2.3.

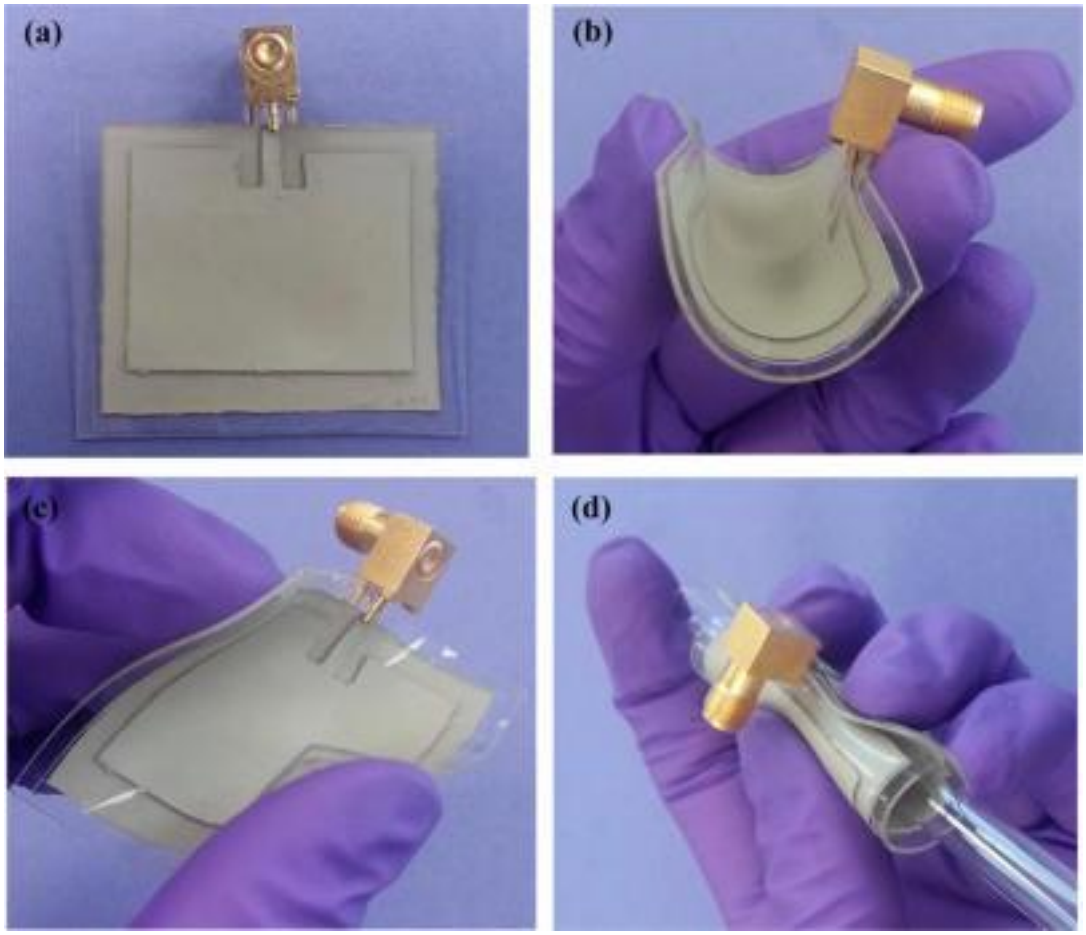

Figure 2.3 : Tuning by the substrate deformation [73]. Photographs of a stretchable microstrip patch antenna composed of AgNW/PDMS flexible conductor: (a) relaxed, (b) bent, (c) twisted, and (d) rolled. Copyright 2014 American Chemical Society.

Structural tuning of metamaterials by mechanically shifting lattice layers have also been studied [92, 93]. By altering the alignment between the split ring resonator layers, a shift in resonant frequency has been reported by Shadrivov *et al.* [92]. Lapine *et al.* [93] demonstrated a dramatic frequency tuning via a lateral displacement of the metamaterial layers, resulting a shift in the alignment of resonators with respect to x and/or y directions as shown in Figure 2.4. This tuning approach appears to allow significant modification to the frequency response of the metamaterials.

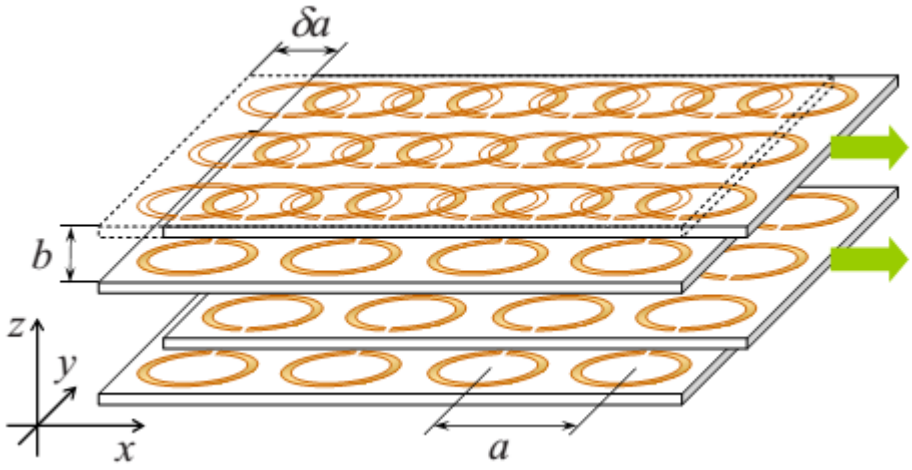

Figure 2.4 : Lattice displacement of metamaterial. Reprinted with permission from [93]. Copyright 2009 AIP Publishing LLC.

Mechanical deformation tuning is a promising approach to produce tunable components without adding any further complexity to the design and fabrication of the structures. This technique allows dynamic tuning without additional circuitry like bias voltage lines and nonlinear components.

2.4.3 Microfluidic/pneumatic method

Recently there has been a lot of progress on the incorporation of microfluidic technology as tuning mechanism in EM components. Microfluidics is a technology that can process or manipulate small amounts of fluid, using channels with dimensions of tens to hundreds of micro-meters [94]. The materials of choice for microfluidic systems are typically optically-transparent materials like silicon, glass, metals, ceramics, hard plastics, and elastomeric polymers. Fabrication in elastomeric polymers like PDMS is easier, more flexible and much less expensive than in silicon or glass, and can conform to and replicate feature sizes of less than 0.1 micron. In addition, its low surface free energy makes it easily lifted from moulds and reversibly sealed to other materials.

The tuning of liquid metal based SRRs has been demonstrated by changing the air pressure within microfluidic channels via pneumatic valves as shown in Figure 2.5 [95]. However, the tuning and reversible response relies on the position of the liquid metal within the channel, and may not return to a consistent state when air pressure is removed. A tunable microstrip bandstop filter incorporating a fluidic transmission line and open stub resonator section has been presented [81]. The fluidity of EGaIn allows the open stub resonator to change its length, hence change the frequency response of the filter in accordance with applied pressure. But, this tuning also has similar issue as the previous work where the length of the stub may not have consistent length versus applied pressure.

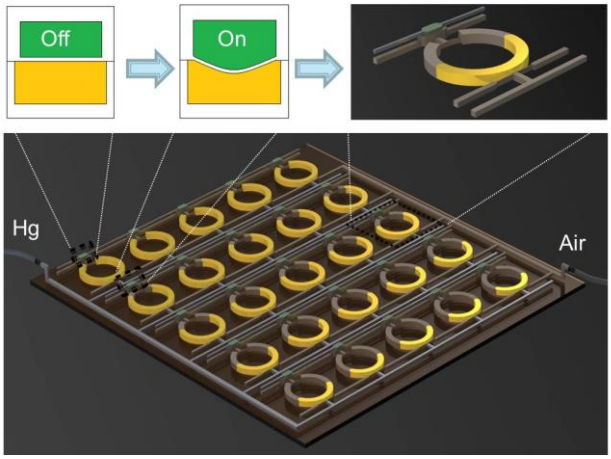

Figure 2.5 : Tuning by the microfluidic/pneumatic method. The yellow parts represent the liquid metal which is controlled by pneumatic valves within the channels [95].

In [17, 96], a pneumatic actuation concept has been proposed to tune the resonant frequency of the metamaterials by adding a secondary thin flexible dielectric membrane layer with the existing metamaterial structures. With no vacuum is applied, an opened switch state can be realised. With the application of a vacuum, the secondary layer can be pressed on top of the metamaterial layer to form a closed switch state. This consequently induces a resonant frequency variance. However, the secondary flexible membrane was manually aligned and sealed to the metamaterial layer, thus, the positioning of the layer may influence the accuracy of the structure.

2.5 MICROFLUIDIC SENSOR

Various metamaterial-based sensors have been studied at microwave frequencies for chemical and biosensing applications [14, 97, 98] as they offer label-free measurement, less time time-consuming sample preparation, low fabrication cost and suitability for lab-on-a-chip implementation. The metamaterial-based structures have also been extensively employed for many other diverse range of sensing applications such as displacement sensing [29, 99], thin-film sensing [100, 101] and strain sensing [102, 103].

As they demonstrate a sharp resonant behaviour at microwave frequencies, metamaterial structures based on SRRs are commonly used to develop chemical and bio-sensors [14, 104, 105]. Torun *et al.* [14] proposed an antenna-coupled SRR-based sensor to study the probing interaction between fibroblast growth factor 2 (FGF-2) and heparin which produce sensing sensitivity of 3.7 MHz/(µg/ml) with respect to changes in concentration of heparin. Rawat *et al.* [105] presented complementary SRR sensor to detect the shift in resonant frequency of different concentrations of water, petrol and ethanol solutions.

The above mentioned sensors encountered many drawbacks as the droplets of the test samples are manually exposed directly to the sensing area of the device. This contributes to unwanted surrounding contamination and is also inappropriate for samples having high volatility. Alternatively, the integration of microfluidic methods with sensors have been proposed, allowing precise fluid flow in a confined area, thus give extra room for sample manipulation and avoiding any undesirable sample handling issues.

A metamaterial-based microfluidic sensor with fluid infiltration has been demonstrated [106]. The fluid alters the resonance frequency of the metasurface array, but no evaluation of fluidic property sensing was conducted. The concept of applying microfluidic techniques to determine the complex permittivity of a fluid sample has also been reported [107-109]. Double split ring resonators (DSRR) micro-milled to accommodate quartz tube capillary passing through the two gaps have been proposed for determining the dielectric permittivity of water, hexane, chloroform, ethanol and methanol [109]. Microfluidic planar SRR-based sensors with coupled microstrip line have been presented to determine complex permittivity of either water-ethanol mixtures or water-methanol mixtures [107, 108] as shown in Figure 2.6. The PDMS microfluidic channel was manually aligned and mechanically sandwiched onto the sensing area, and the positioning of the channel may influence the measurement accuracy. Most studies have been limited by the microfluidic sensing channel design itself, where it has been attached separately from the non-microfluidic device sensor. In another words, it is not a fully integrated microfluidic sensor design. This major impediment makes them impractical and inefficient when employed as a stand-alone microfluidic sensor for lab-on chip applications. Furthermore, the designs also require physical electrical

connectors to evaluate the dielectric properties, making them cumbersome to use.

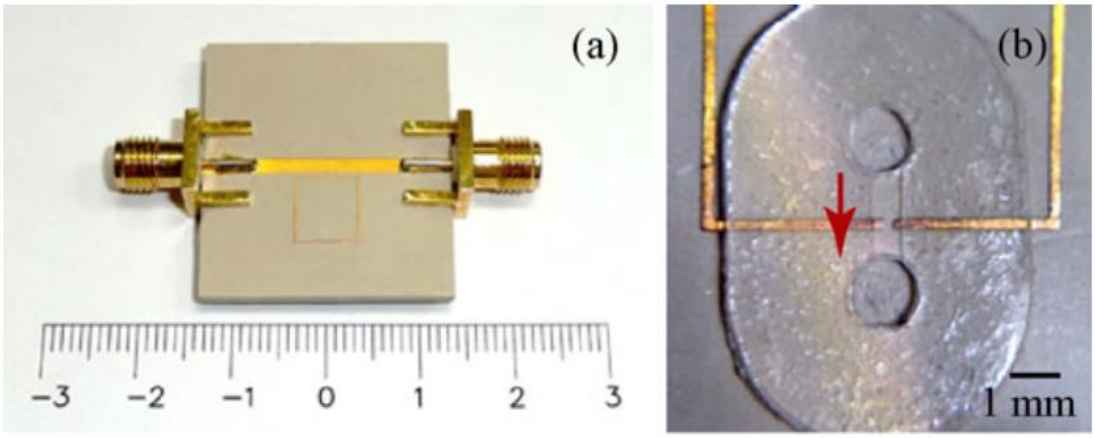

Figure 2.6 : Microfluidic sensing utilising the SRR gap. (a) Fabricated microstrip-coupled SRR. (b) A zoom-in showing the microfuidic chamber attached to the SRR [107]. Copyright 2013 Elsevier.

2.6 DIELECTRIC PROPERTIES MEASUREMENT METHODS

For electromagnetic components to be efficiently designed on flexible substrates, the material properties need to be determined at the microwave frequency range. Dielectric properties measurement methods can be divided into two main categories [110]:

- transmission-reflection methods (e.g. measuring in coaxial line, waveguide, and free-space, or with open ended coaxial line) and
- resonant methods

For selecting the most suitable method for the dielectric properties measurement, several significant factors including frequency range, accuracy, material properties, form of material, sample size restrictions, destructive or non-destructive, contacting or non-contacting and cost need to be taken into consideration.

The notable difference between the transmission-reflection method and the resonant method is the ability of the transmission-reflection method to measure dielectric properties at broadband frequency ranges, whilst, the resonance method can measure only at a single frequency [111]. However, the resonant methods have higher accuracy than the transmission-reflection method, particularly for the loss tangent determination. The differences of the methods are summarised as in Table 2.1.

Table 2.1 : Summary of the dielectric measurements method [110].

Method	**Measured parameters**	**Descriptions**
Coaxial probe	ε_r	Broadband, convenient, non-destructive Best for lossy MUTs; liquids or semi-solids
Transmission line	ε_r and μ_r	Broadband Best for lossy to low loss MUTs; Machineable solids
Free space	ε_r and μ_r	Non-contacting Best for high temperature; Large, flat samples
Resonant cavity	ε_r and μ_r	Accurate Best for low loss MUTs: small samples
Parallel plate	ε_r	Accurate Best for low frequencies: Thin, flat sheets

The resonant perturbation method [112] can measure low dielectric loss samples as well as having a very simple calculation and measurement procedure. As this method cannot measure over large frequency ranges, it can be used in conjunction with the broader band waveguide method to study the dielectric properties over a wider range (e.g. X-band frequencies).

2.7 PROCESSING AND FABRICATION METHODS

Several well-established methods have been demonstrated to pattern the electromagnetic components onto flexible substrates, such as soft-lithography [113], shadow mask lithography [114] and 3D imprint lithography [115]. In the fabrication of microfluidic devices using PDMS, typically soft lithography techniques are employed. Soft lithography involves the replication of a defined structure on a master in a soft elastomer, and the replication process also can be repeated multiple times. Hence, soft lithography offers rapid, simple and inexpensive fabrication process for microfluidics devices. Additionally, this method is suitable for a wide range of structure sizes and enable patterning on non-planar surfaces [49]. Figure 2.7 illustrates the details of fabrication process using soft lithography which have been discussed by McDonald *et al.* in [116]. The soft lithography process typically starts with photolithography process to pattern defined structure on a silicon 'master' substrate. PDMS is then poured/spin coated on the patterned master, followed by curing and lift-off to produce an inverse replica of the master. Subsequently, the replica is sealed to a substrate of choice to enclose the channels.

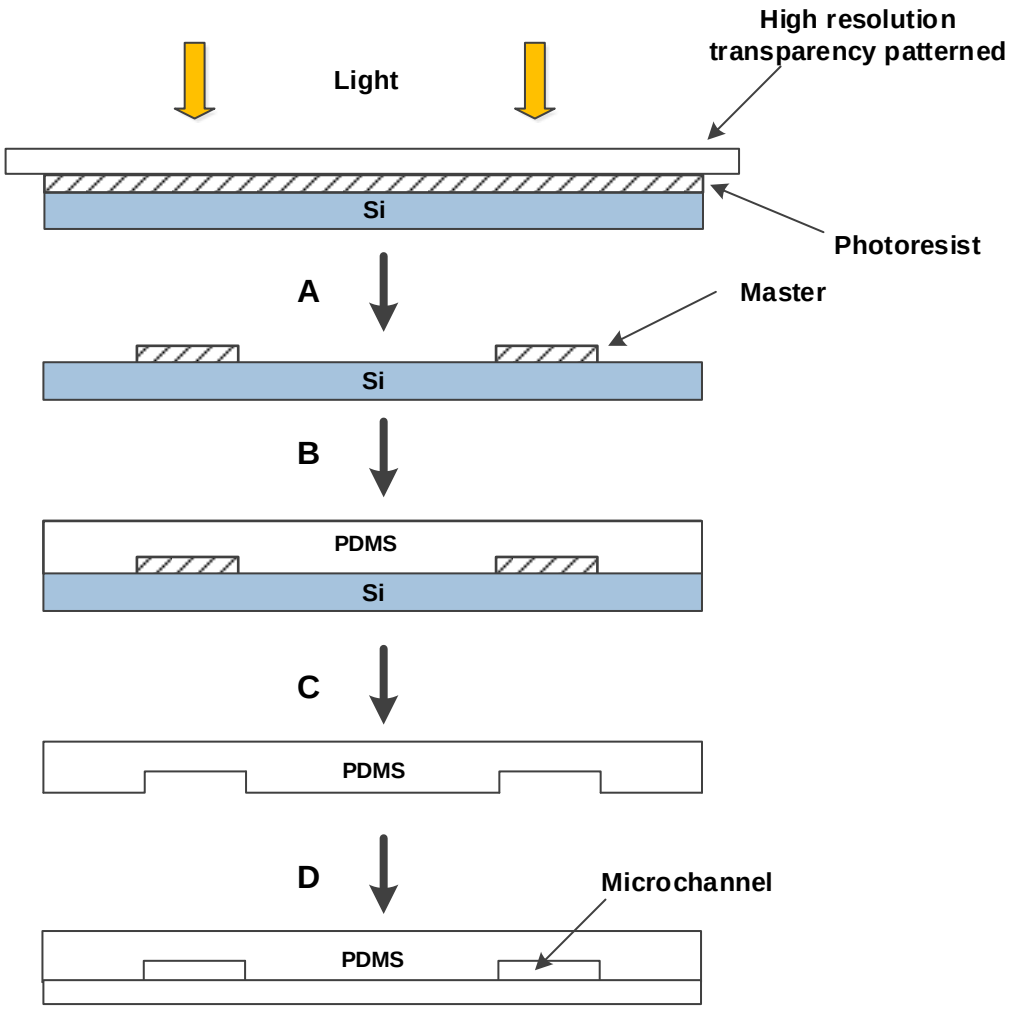

Figure 2.7 : Soft Lithography process. Adapting from ref. [116]: (A) Perform photolithography to pattern defined structure on a silicon 'master' substrate (B) Casting of PDMS with subsequent curing (C) Replica moulding and (D) Transferring and sealing.

2.8 SUMMARY AND OUTLOOK

Electromagnetic devices realised on flexible materials/substrates allow ease of integration with non-uniform surfaces, making them advantageous for flexible electronic environments. They can be made substantially sensitive to mechanical deformation, opening up new possibilities for dynamic tuning and engineering resonances. Mechanical deformation tuning by employing microfluidic/pneumatic methods is a very promising method to create tunable electromagnetic devices. It allows

dynamic tuning without bias voltage circuits and nonlinear components that can interfere with the electromagnetic response. Thus, it also will reduce design and fabrication complexity. This method has the potential to be implemented in a wide range of sensing applications such as mechanical, chemical and biomedical sensing.

Elastomeric materials doped with low-loss fillers are receiving significant attention from the scientific community due to their tremendous potential as flexible microwave substrates. A key feature of an ideal flexible microwave substrate is having excellent flexibility and also low dielectric loss properties. However, it is very difficult to identify a homogeneous material which possesses these desired properties. The search for these crucial characteristics has led to the incorporation of micro/nano particles as fillers in the flexible host matrix, e.g. polydimethylsiloxane (PDMS). The manipulation of the dielectric properties of PDMS is highly desirable as it can create tremendous opportunities for flexible/stretchable microwave devices such as resonators, antennas, switches, filters and oscillators.

CHAPTER 3

MECHANICALLY TOLERANT FLUIDIC SPLIT RING RESONATOR

3.1 INTRODUCTION

Flexible resonators are a crucial electromagnetic component for non-planar, conformal and curved/movable surfaces in flexible electronic environments. In most applications (apart from mechanical tuning and sensing systems), the frequency response of the flexible circuit is fixed and ideally should not vary. Thus, it is important to realize a simple and versatile design that can allow resonator to have stable resonance frequency under mechanical deformation.

In this chapter, a fluidic SRR which can be stretched, mechanically strained, and reversibly deformed (bent, stretched and twisted) is demonstrated. Galinstan (a eutectic alloy of 68.5% Ga, 21.5% In and 10.0% Sn) was impregnated into a microfluidic channel formed from two PDMS layers to realise the fluidic SRR. The Galinstan in its liquid state flows within the channel in response to large stresses and deformations, and reverts to its base state under relaxation. Cycling the stressed and relaxed state is shown to have minimal impact on the performance of the SRR. The fluidic SRR has the potential to be implemented in flexible electronic environments, especially for non-planar, conformal and curved/movable surfaces, and provide a predictable and stable response.

3.2 SPLIT RING RESONATOR (SRR) DESIGN

Resonator structures like the Split Ring Resonator (SRR) are widely used as building blocks to form metamaterials [117-119]. The SRR structure was first introduced by Pendry in 1999 [120]. Figure 3.1(a) shows a single SRR structure where *R* is the inner radius, *w* is the thickness, *g* is the gap width and *h* is the height. It also can be represented as an equivalent *LC* circuit where the gap is associated with the capacitance (*C*) and the current path is related with the inductance (*L*) as depicted in Figure 3.1(b).

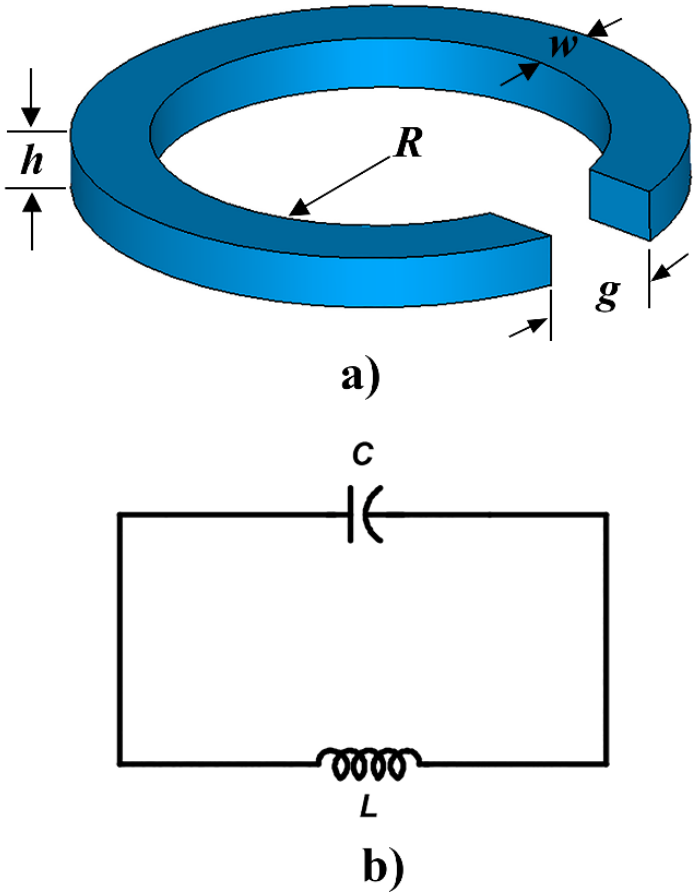

Figure 3.1 : a) A single SRR structure, and b) an equivalent circuit.

The resonance frequency (ω_o) of the electric and magnetic SRR can be calculated by:

$$\omega_o = \sqrt{\frac{1}{LC}} \tag{3.1}$$

The values of capacitance and inductance can be calculated by using the following equations [121]:

$$L = \mu_o \mu_r R_m \left(\log \frac{8R_m}{h+w} - \frac{1}{2} \right) \tag{3.2}$$

$$C = \varepsilon_o \varepsilon_r \left(\frac{hw}{g} + (h+w+g) \right) + \frac{2\varepsilon_o \varepsilon_r (h+w)}{\pi} \left(\log \frac{4R}{g} \right) \tag{3.3}$$

where h is the height of the SRR, $R_m = R + \frac{w}{2}$, μ_o is the free space permeability, μ_r is the relative permeability of the substrate material, ε_o is the free space permittivity and ε_r is the permittivity of the substrate material.

3.2.1 Development of Tolerant Fluidic SRR

In this work, the SRR structure consists of patterned fluid metal Galinstan encapsulated in a PDMS microfluidic channel. An SRR structure was chosen to characterise resonant shifts under various distortion states due to its simplicity and well-established design. The geometric parameters of the proposed SRR structure as shown in Figure 3.2(a) are w = 2.2 mm, R = 6.4 mm, l_1 = 22 mm and l_2 = 22 mm. The height of the microfluidic channel, and hence, the thickness of the liquid metal layer (h) was approximately 0.2 mm, sandwiched between PDMS layers with total thickness (t) of around 0.7 mm. The SRR also incorporates two cylindrical metallic pillars near the open ends of the ring: a by-product of the method used to fill the microfluidic channel with Galinstan. These pillars are accounted for in the simulation of the SRR performance, and contribute an extra capacitive component which is accounted for in the gap capacitance.

The SRR is simulated in a WR-284 rectangular waveguide environment as shown in Figure 3.2(b) using CST Microwave Studio software. The rectangular waveguide

measurement setup was employed to create a stable and controllable environment for testing the SRR properties, particularly important during the stretching and conformity experiments.

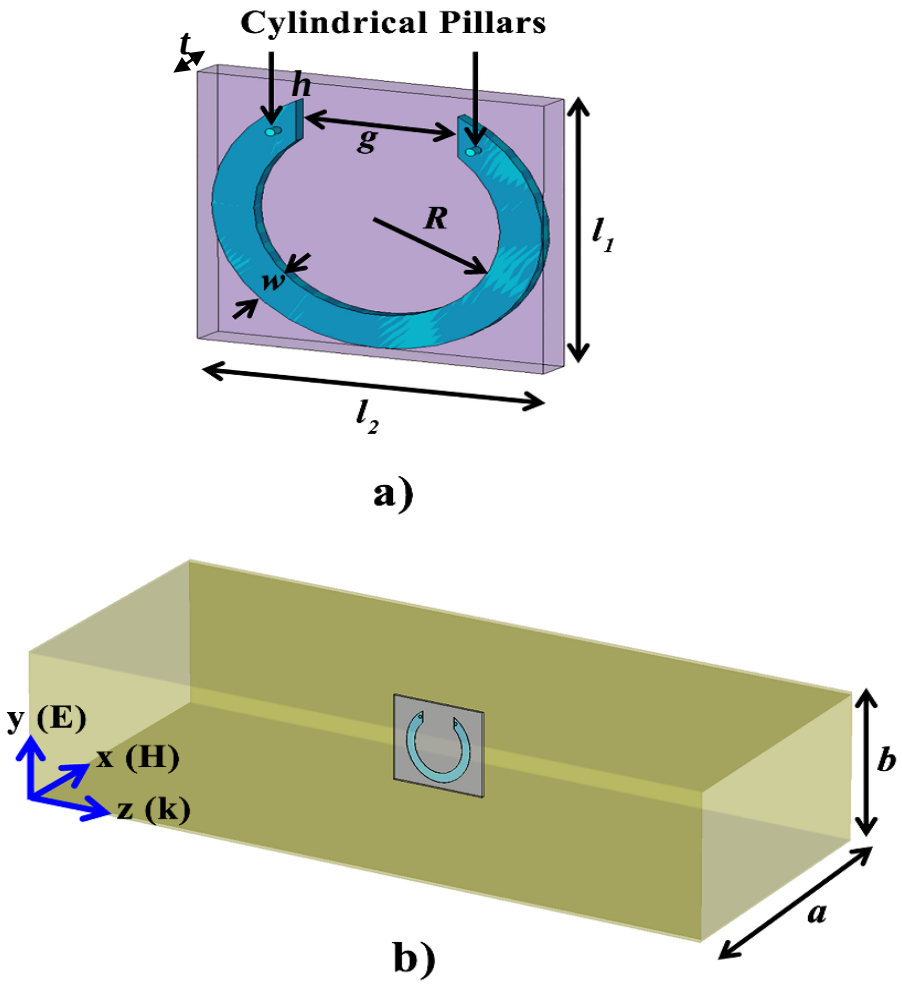

Figure 3.2 : a) Schematic of the SRR and b) the SRR in a WR-284 rectangular waveguide. Parameters: w = 2.2 mm, R = 6.4 mm, h = 0.2 mm, t = 0.7 mm, l_1 = 22 mm, l_2 = 22 mm, a = 72.136 mm, and b = 34.036 mm.

The gap of the ring as its associated with the capacitance, $C = \frac{\varepsilon A}{g}$ of the circuit primarily determines the resonant frequency. This is general rules of thumb for designing a SRR. Studies have shown that a smaller gap results in a lower resonance frequency than a

wider gap [122, 123]. Hence, most studies normally consider or use smaller gap in their designs.

The dependence of the transmission response of fluidic SRR on the variation of gap width is studied with an aim of examining the tolerance of the component to mechanical deformation. As noted above, an increase of the gap width causes a shift to higher resonant frequencies. By changing the gap width of the SRR in Figure 3.2 from 0.8 mm to 8.4 mm with all other parameters kept constant, the resonant frequency shifted to 2.3 GHz to 3.2 GHz, respectively (shown in Figure 3.3(a)). The depth of the resonance also increases slightly with increasing gap width.

To investigate the effect of the gap width on the mechanical tolerance of the fluidic SRR, of the two extreme values, g = 0.8 and 8.4 mm are chosen. If a 5% mechanical strain applied to the overall fluidic SRR structure, an increment in the gap region of 0.42 mm results. To make a basic representation of this strain, the wide gap SRR has a "stretched" value of $g = 8.4 + 0.42 = 8.82$ mm. Accordingly, the same strain increment is applied to the gap width of 0.8 mm, giving the new value of $g = 0.8 + 0.42 = 1.22$ mm. The transmission response of these variations are shown in Figure 3.3(b) and Figure 3.3(c). The variation of gap width from 8 mm to 8.82 mm produces only 1% of resonant frequency shift, but for the narrower gap width variation from 0.8 mm to 1.2 mm the resonant frequency shifts up to 5%. These results are summarised in Table 3.1. Thus it can be concluded that an SRR with a wider gap has a less significant effect on the resonance frequency when a deformation due to mechanical strain is applied, and is more suitable architecture for designing a mechanically tolerant SRR. Therefore, to realise tolerant SRR, a gap width of 8.4 mm is selected.

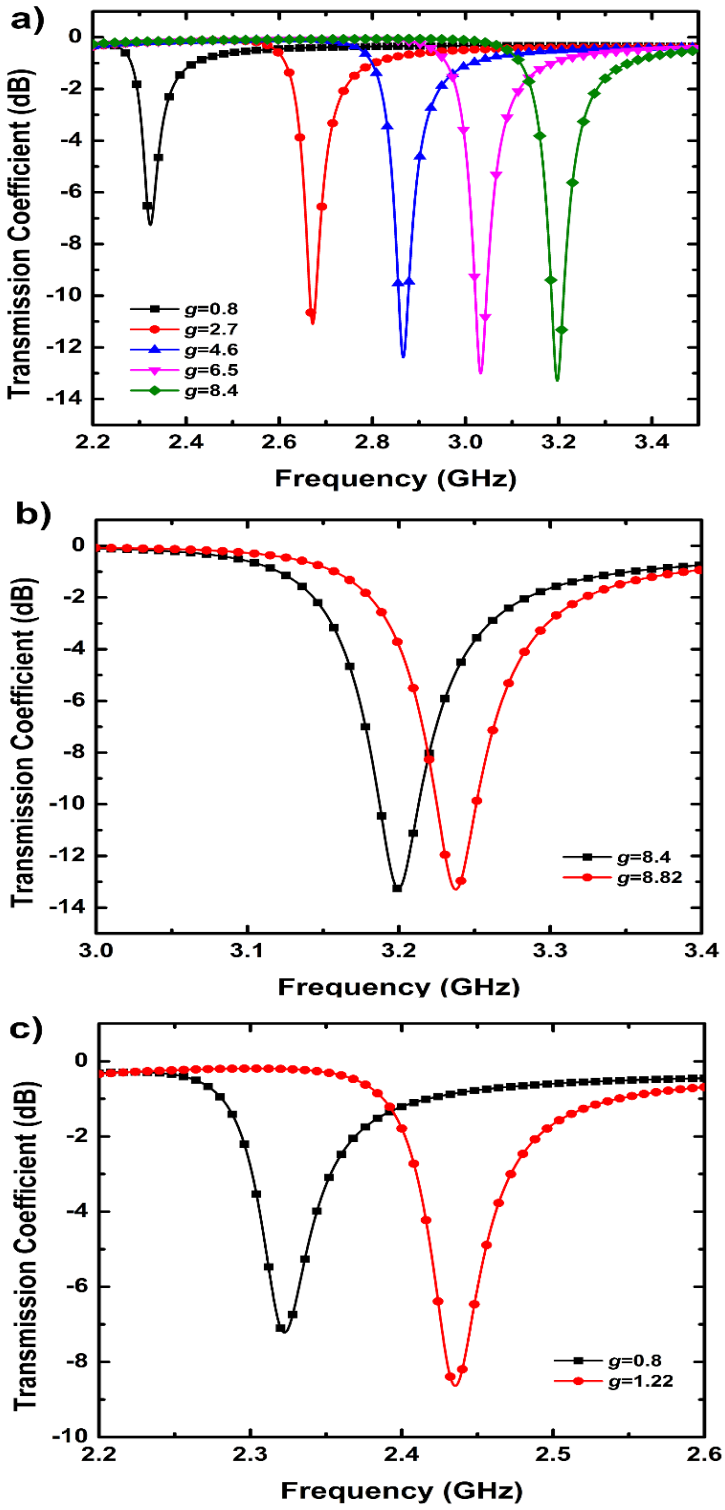

Figure 3.3 : Transmission coefficient response of the fluidic SRR with different gap widths (*g*) in mm a) parametric variation of the gap width b) representation of mechanical deformation of the narrow gap width, and c) representation of mechanical deformation of the wider gap width.

Table 3.1 : Summary of mechanical tolerance for different gap width SRRs

Gap width, *g* (mm)	Frequency (GHz)	$\|S_{21}\|$ (dB)	% shift
8.40	3.199	-13.255	-
8.82	3.238	-13.304	1%
0.80	2.322	-7.220	-
1.22	2.435	-8.637	5%

Apart of gap width, other parameters like *w* and *h* also play a significant role in the determination of the resonant frequency. The width *w* of the liquid metal channel is varied whilst keeping the radius of the ring and all other parameters constant. From Figure 3.4, increasing ring width creates a corresponding increase in the resonant frequency, albeit only a small variation. The depth of the resonance also increases slightly with increasing ring width.

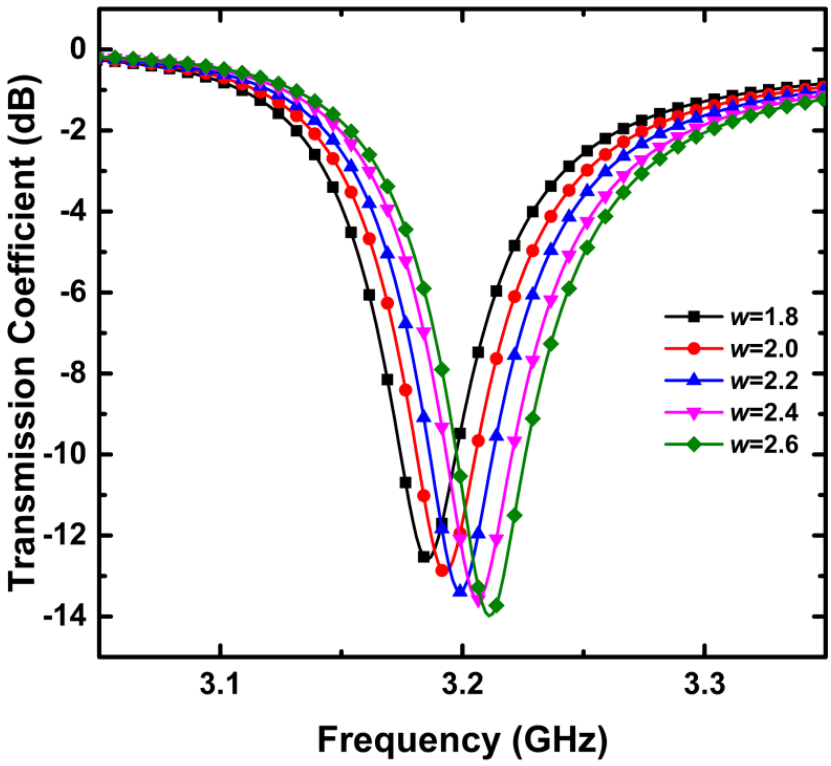

Figure 3.4 : Transmission coefficient with different ring width (*w*) in mm.

Figure 3.5 shows the transmission coefficient of the single element SRR structures when the ring height is varied from 0.1 mm to 0.5 mm, and all other parameters are kept constant. As the ring height is increased, the frequency and depth of the resonance both increase. A summary of the selected SRR parameters for fabrication are listed in Table 3.2.

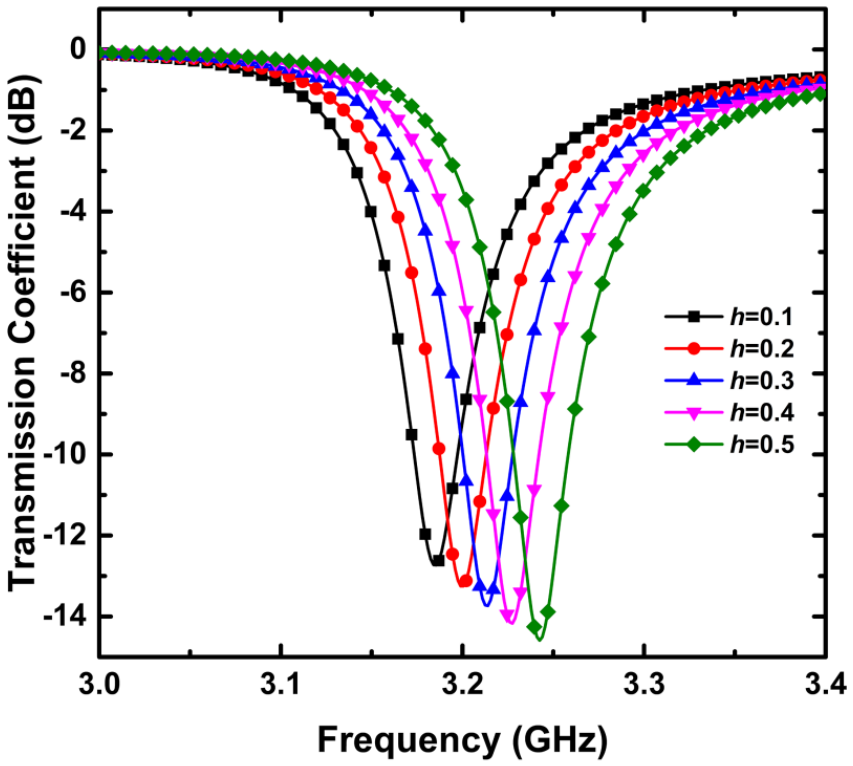

Figure 3.5 : Transmission coefficient with different ring height (*h*) in mm.

Table 3.2 : Geometric parameters of the fabricated fluidic SRR

Parameter (mm)	Value (mm)
w	2.2
R	6.4
g	8.4
h	0.2

3.3 FABRICATION OF SRR

There are two intersecting procedures involved in realising the SRR microfluidic channel, which employ standard micro-fabrication techniques as shown in Figure 3.6. First, a 'master' pattern of the SRR is generated on a polymethylmethacrylate (PMMA)

material using an isel-CNC CPM 3020 micro-miller. The PDMS (Sylgard 184, Dow Corning Corporation) is prepared utilising the proprietary crosslinker at a 10:1 ratio and the mixture is degassed for 30 min. Then the PDMS mixture is spin-coated on the patterned master at 350 rpm for 30 s to obtain ~450 µm thickness, followed by curing and lift-off to produce an inverse replica of the master. The inlet and outlet hole to the channel is defined using a standard 0.75 mm diameter surgical punch. Second, a ~250 µm flat PDMS layer is created on silicon (Si) wafer by spin coating at 440 rpm for 30 s and half-curing on hotplate for 8 min at 70 °C. It is then brought into contact with the microfluidic channel patterned PDMS. Subsequently, the stack of layers is placed in the oven at 70 °C for 10 min to complete the bonding and curing process and permanently seal the channels. The fluid Galinstan is injected into the microchannel, and the inlet and outlet of the microfluidic channel are sealed by placing a half-cured drop of PDMS over the hole after the injection process is complete.

Finally, the liquid metal SRR encapsulated in PDMS is carefully peeled off from the silicon carrier wafer to realise the flexible SRR as seen in Figure 3.7. This fabrication method allows for rapid prototyping, and a single ‘master’ can be reused to produce many identical SRRs.

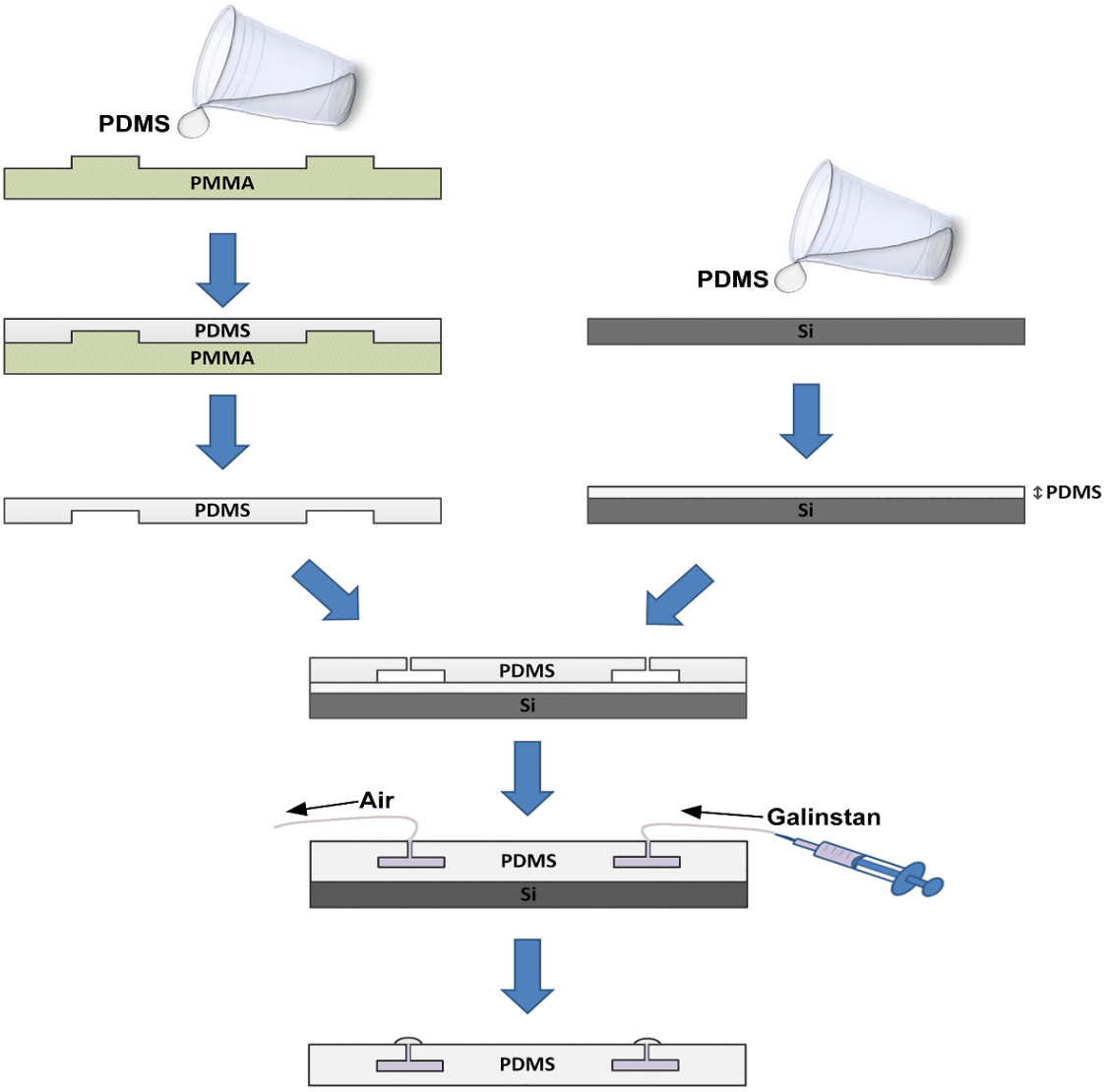

Figure 3.6 : Schematic illustration showing the sequence for SRR fabrication.

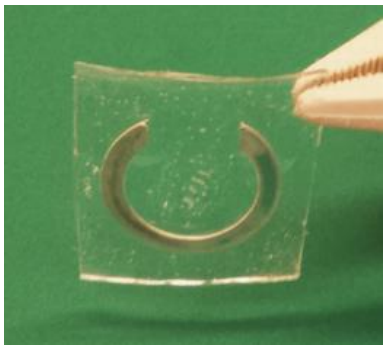

Figure 3.7 : A fabricated flexible SRR

3.4 TESTING/MEASUREMENT SET-UP

The measurement of the SRR transmission properties is carried out using the WR-284 rectangular waveguide as shown in Figure 3.8. An Agilent E5071B ENA series vector network analyser was calibrated according to the standard Thru-Reflect-Line (TRL) procedure. The SRR was adhered to a flat foam substrate, and also curved-foam blocks, to assist in locating it in the middle of the waveguide. The effect of the foam on the transmission response has been eliminated during the calibration process of the waveguide. The flat SRR provides a baseline measurement and comparison to simulation. The curved SRR is used to study the effect of bending the flexible SRR structure on the transmission response. The SRR is excited by the magnetic field perpendicular to the element plane, as indicated in Figure 3.2b).

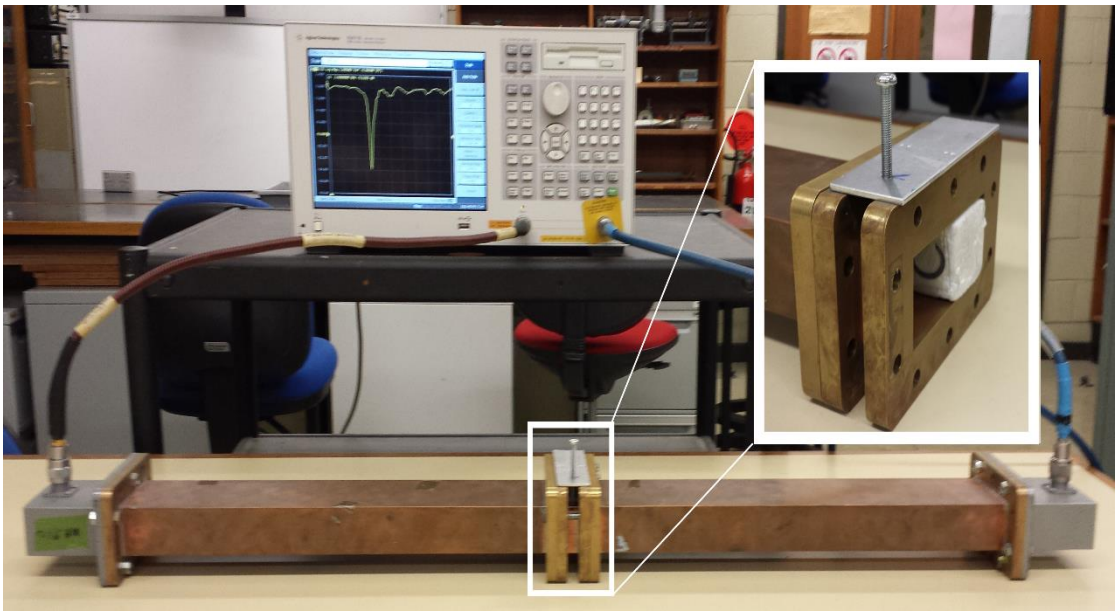

Figure 3.8 : Measurement set-up

To test the performance of the SRR under strain, a custom-made jig made from an acrylonitrile butane styrene (ABS) plastic consisting of two clamps guided by a vertical frame is placed in the waveguide. The clamps are affixed to two ends of the SRR structure: the bottom clamp is static, but the upper clamp is designed to slide upward via two strings chained out of the waveguide through tiny holes. The strings are fastened to a screw to manually control the stretching process. A picture of the clamping device can be observed in Figure 3.9.

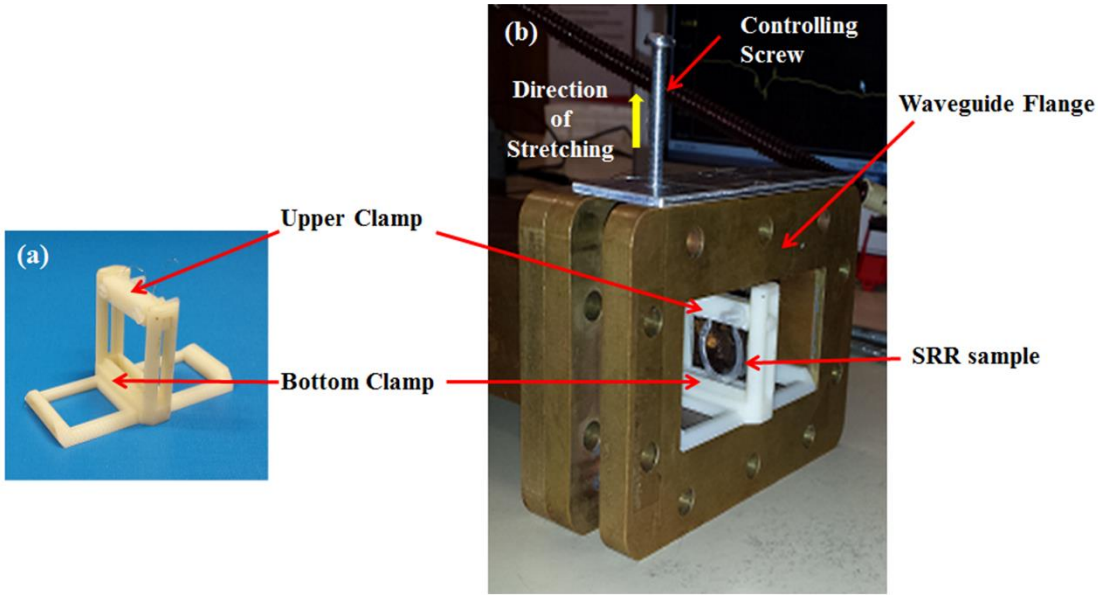

Figure 3.9 : Photographs of the custom-made device used to stretch the SRR. (a) Two clamps to mount each end of the SRR. Upper clamp can slide upwards for stretching test, whilst bottom clamp is static position. (b) The SRR framed in the device and located in the testing waveguide. The screw applies the required force to stretch the SRR in a controlled manner.

The stretching projection can be portrayed as in Figure 3.10. When the strain is applied, the SRR will be elongated to a certain strain level (Δl). Thus, the percentage of the strain can be calculated using:

$$\% \text{ of strain} = \frac{\Delta l}{l} \times 100\% \tag{3.4}$$

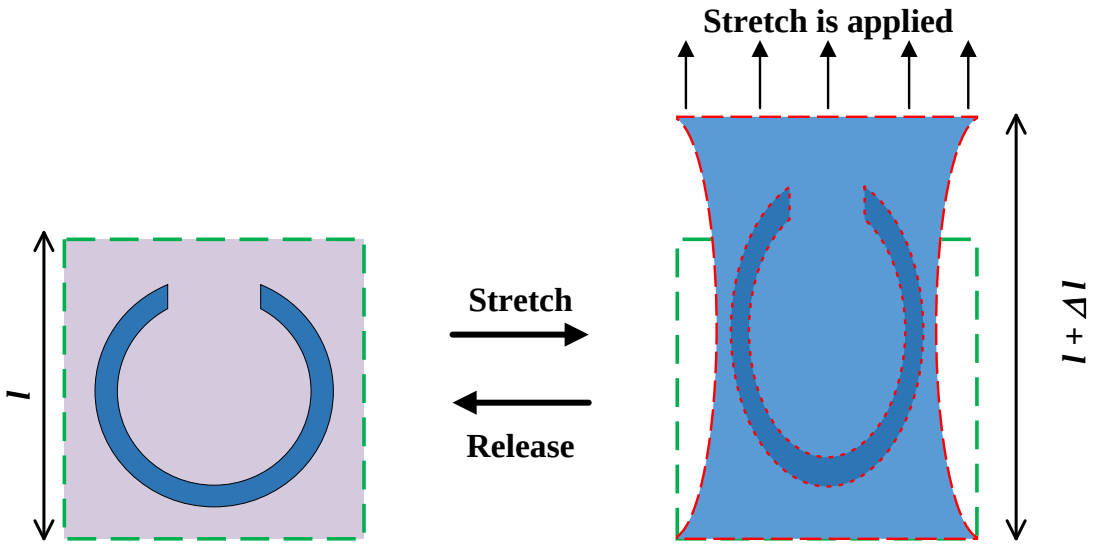

Figure 3.10 : A schematic of SRR before and after being stretch. (a) The initial SRR, and (b) The strained SRR.

3.5 RESULTS AND DISCUSSION

3.5.1 Non-deformed

Four different orientations of the SRR are examined in a non-deformed state, represented by the rotation of the split towards all four sides of the waveguide. The four orientations correspond to the 0°, 180°, 90° and 270° locations of the split with respect to the y-z plane in Figure 3.2b). For measurement, the SRR was adhered to a flat foam substrate as shown in Figure 3.11. These orientations are henceforth referred to as OR0°, OR180°, OR90° and OR270°.

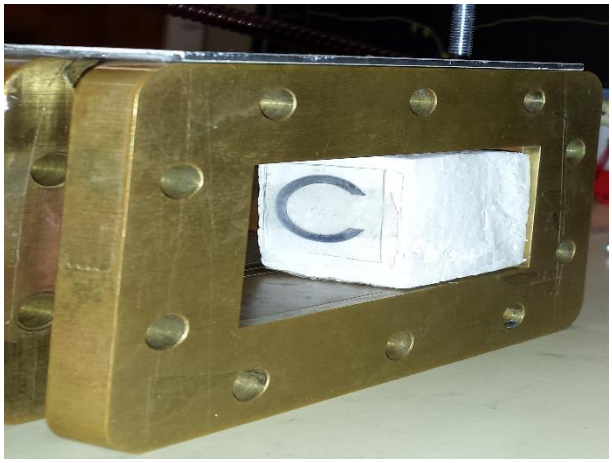

Figure 3.11 : Flat SRR in rectangular waveguide indicating the non-deformed state

Figure 3.12 shows the simulated and measured results of the SRR in a non-deformed state. Simulation results of OR0° and OR180° exhibit resonant dips at 3.0 GHz and OR90° and OR270° resonate at 3.1 GHz. The calculated value of the resonant frequency of the SRR based on equations 1 and 2 is 3.287 GHz, exhibiting reasonable correspondence to the simulated and measured values.

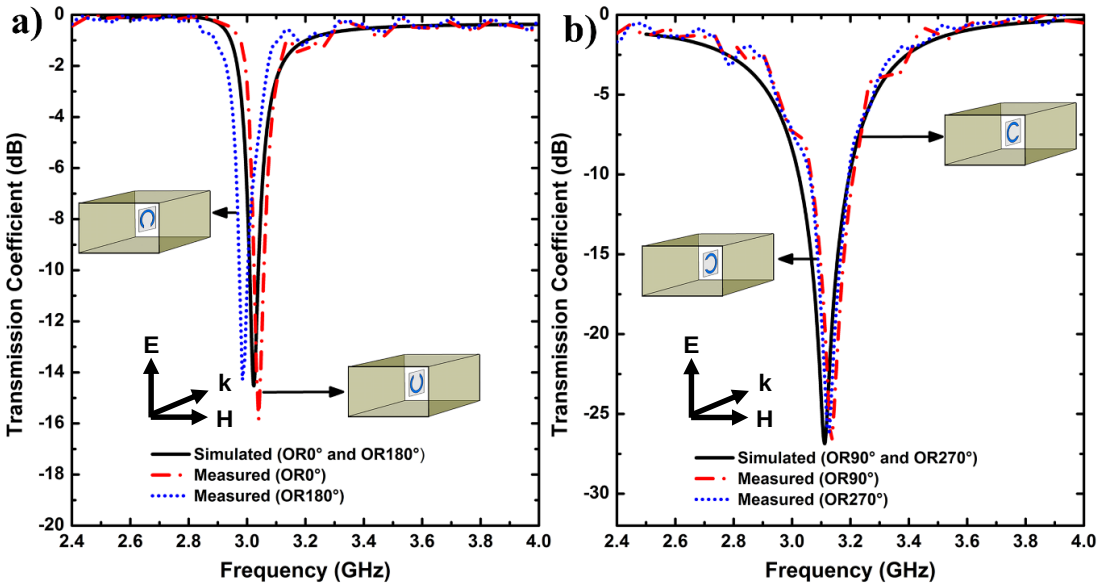

Figure 3.12 : Simulated and measured transmission coefficient results for the flat SRR: a) OR0° and OR180°, and b) OR90° and OR270°.

3.5.2 Bending

Several measurements were taken to demonstrate the tolerance of the SRR to bending, stretching and twisting. To study the effect of bending, three different curved-foam blocks with 2.7 cm radius, 1.7 cm radius, and 1.0 cm radius were used as in Figure 3.13. Figure 3.14 shows the measured results of the SRR at these curvatures. The transmission response exhibits good similarity compared to the flat SRR, with the resonance varying less than ±72 MHz (<2.4%). OR0° and OR180° are particularly tolerant. This signifies the suitability of the SRR to be implemented on curved/conformal surfaces or structures movable or flexing parts.

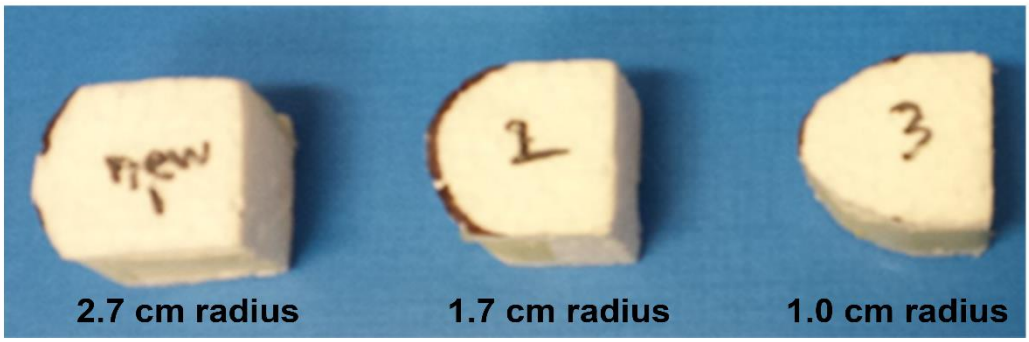

a)

b)

Figure 3.13 : a) Photograph of three different curved-foam blocks used for bending measurements, and b) curved-SRR in the waveguide.

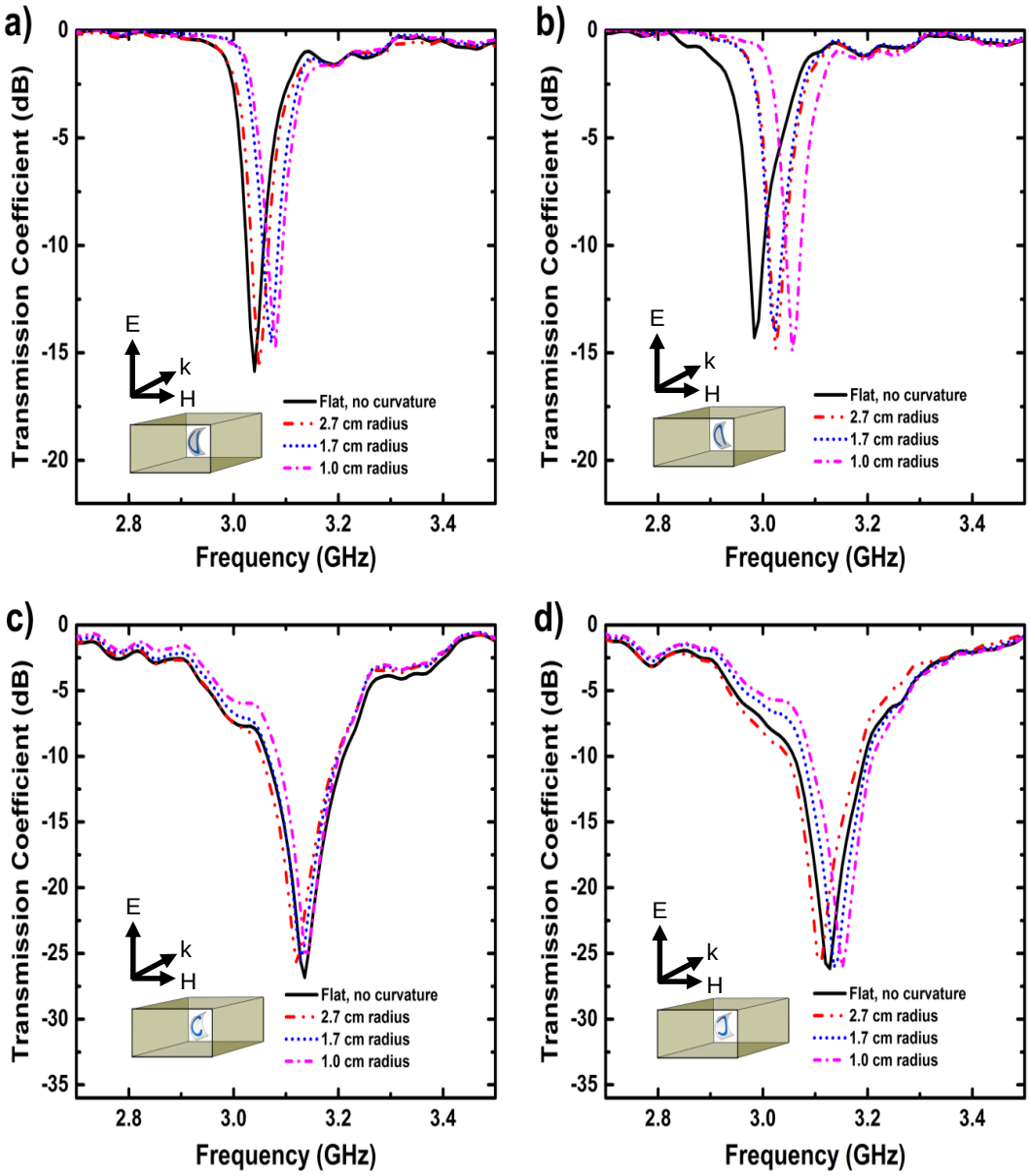

Figure 3.14 : Measured transmission coefficient of the SRR at various bending radii: a) OR0°, b) OR180°, c) OR90° and d) OR270°.

3.5.3 Stretching

Figure 3.15 shows the transmission response of the SRR under mechanical stretching along the *y*-axis for OR0° and OR90° (Note: due to similarity in their resonant responses, OR180°and OR270° were not investigated). The initial resonance of OR0°

at its relaxed position is equal to 3.042 GHz, as depicted in Figure 3.15(a). When a stretching force is applied up to 18% strain, the resonant frequency lowers by only 86 MHz or about 3%. Inducing strains along the *y*-axis for OR90° results in an increasing SRR gap, and very similar transmission coefficient responses can be observed as presented in Figure 3.15(b) with the frequency response shifting by less than 0.6%. The results suggest that performance variation of the stretchable fluidic resonator was minor under levels of stretching up to 18%.

To characterise the repeatability and reversibility of the stretchable SRR, the process of stretching and releasing was repeated five times. Initially, the SRR was stretched with 5% strain and then relaxed to the original position. The same process is repeated for 9%, 14% and 18% strains. The investigation results are presented in Figures 3.15(c) and 3.15(d), indicating that good repeatability is achieved for both orientations. Upon releasing/relaxing the strain, the fluidic resonator almost returned to its initial resonant frequency with a difference of <0.2%, exhibiting excellent reversible deformity.

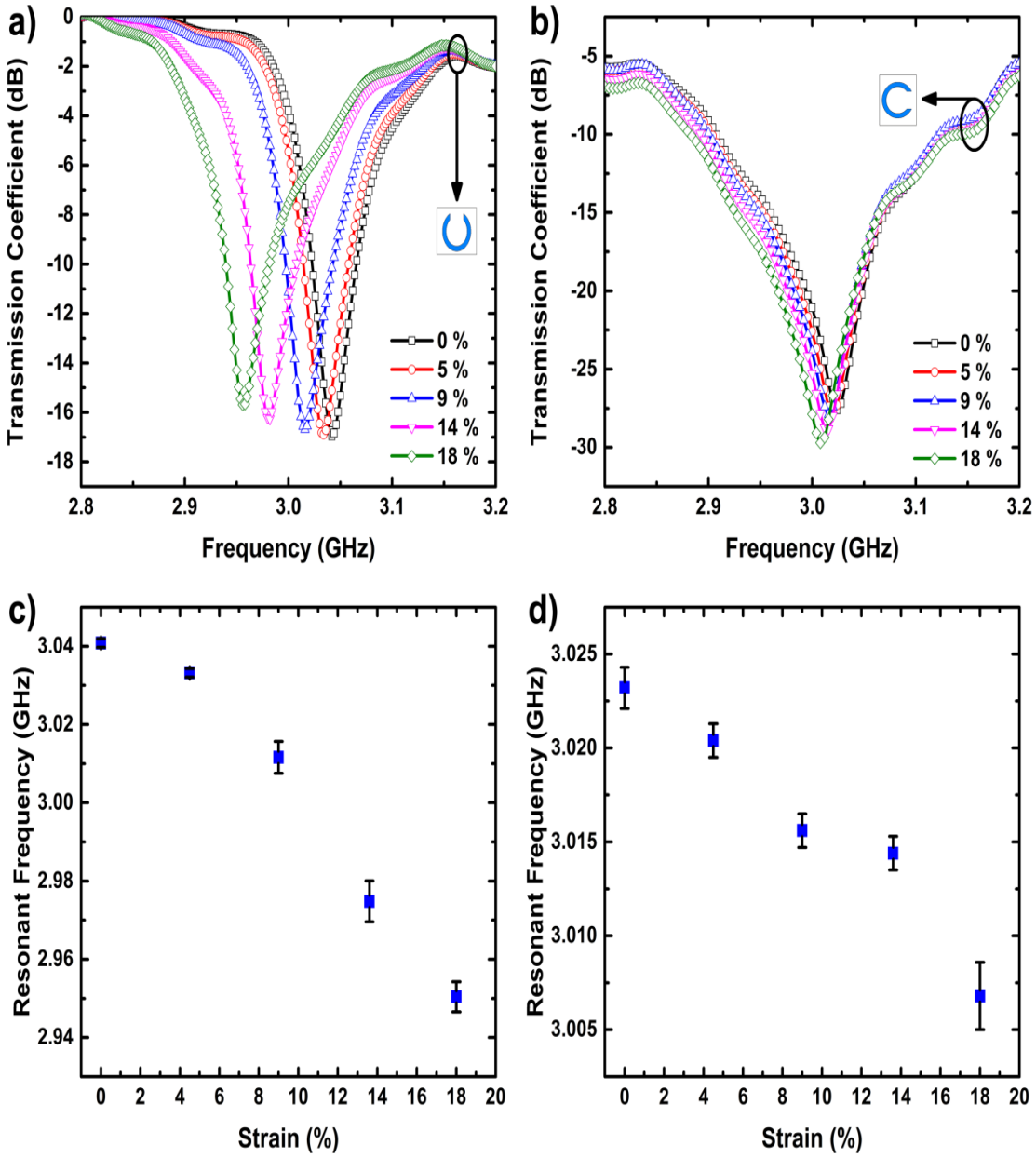

Figure 3.15 : Measured transmission coefficient for the SRR under strain for: a) OR0° b) OR90°. Resonant frequency as a function of strain for: c) OR0° d) OR90°.

3.5.4 Twisting

The transmission coefficient of the single element SRR was also investigated when twisted ±25º and ±45º from the z-axis in the custom made stretching jig. As in Figure 3.16, the twisting angle is defined according to the position of the top clamp after

twisting process while the bottom clamp remained static. Figure 3.17 displays a photograph of the significantly twisted element. The stretching results are depicted in Figure 3.18. Once again no significant changes in the resonant frequency are observed, with only ~0.53% difference for OR0° and <2% difference for OR90°.

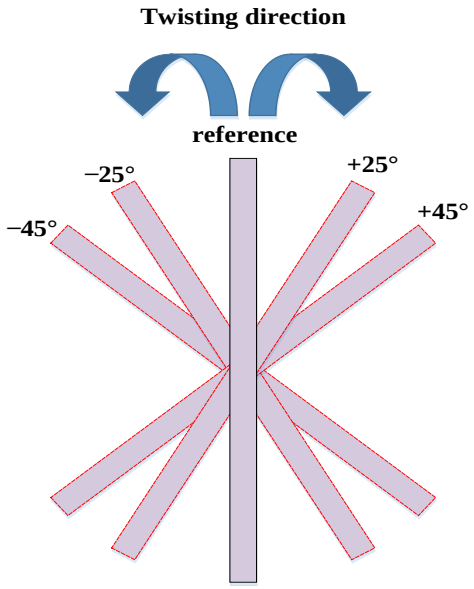

Figure 3.16 : Top view of the top clamp of the custom made test jig which define the twisting angle.

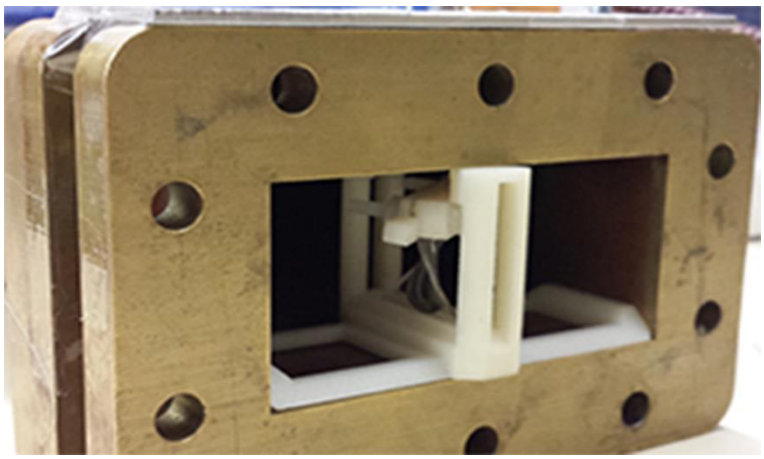

Figure 3.17 : Twisted SRR in the rectangular waveguide.

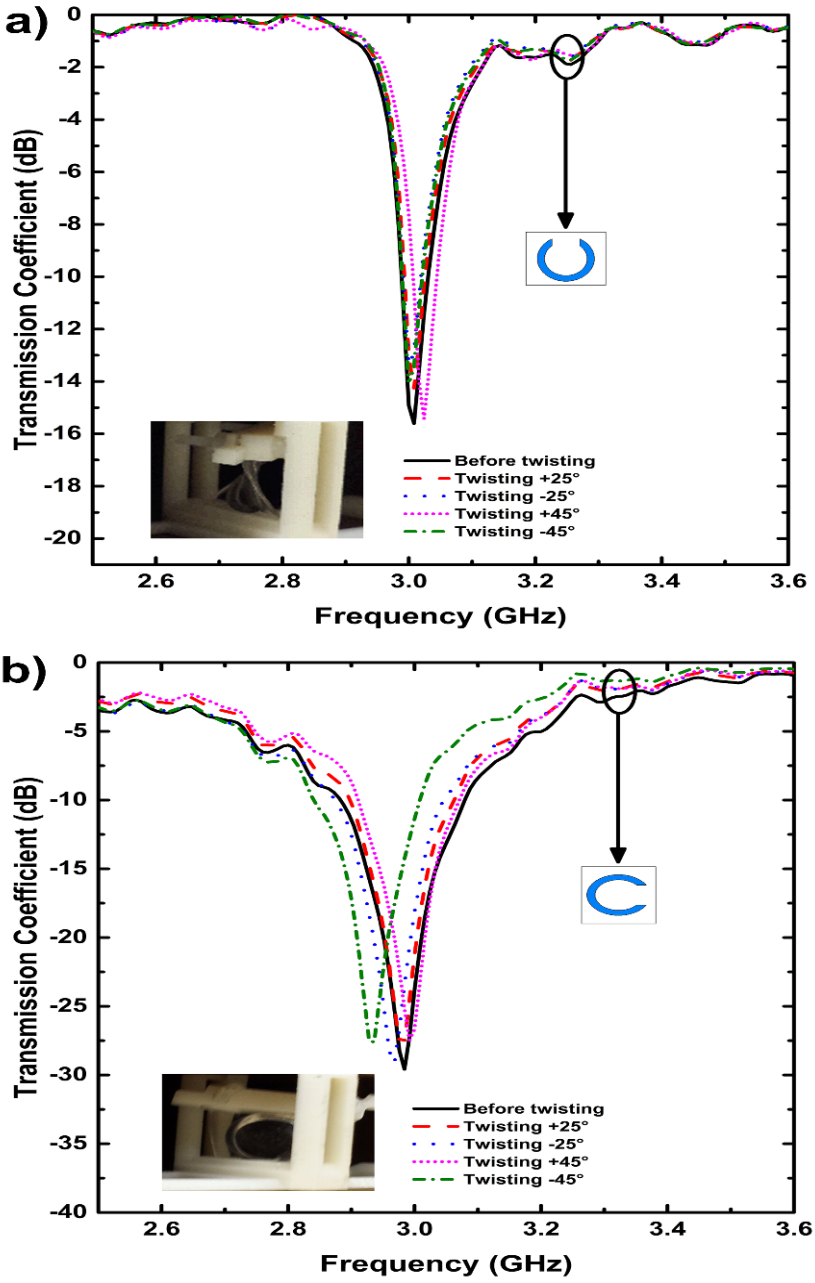

Figure 3.18 : Measured transmission coefficient of the twisted SRR from the z-axis: a) OR0° and b) OR90°.

3.6 SUMMARY AND OUTLOOK

This chapter has demonstrated that a wide gap flexible SRR can exhibit mechanically tolerance to being bent, stretched, twisted and reversibly deformed. Infiltrating liquid metal Galinstan into a microfluidic channel formed in PDMS allows the resonator to be

deformed significantly and reversibly without loss of electrical continuity. Under the mechanical deformation no significant change of transmission response and resonant frequency was recorded, with maximum recorded frequency shifts less than ~3% for all cases. Thus the proposed SRR is well suited to applications with non-planar/conformal surfaces, or moving/vibrating flexible electronic environments that require elements to withstand mechanical strain.

CHAPTER 4

TUNING AND SENSING WITH MICROFLUIDIC SRRs

4.1 INTRODUCTION

In the previous chapter it was observed that flexible split-ring resonator (SRR) meta-atoms exhibit electromagnetic effects that are mechanically tolerant to bending, stretching and twisting without compromising its electrical performance. The SRRs are arguably the most common element used in forming the basic microstructure of metamaterials. The fundamental resonance of SRRs can be considered to behave like an LC oscillatory circuit that contains an inductance in series with a capacitance, produced by the capacitive gap of the SRR. There are numerous ways in which the resonant frequency of the SRRs can be altered or tuned, as discussed in Chapter 2. A simple way is by altering the gap capacitance as this plays a significant role in determining the resonant frequency of the structure.

In this chapter, a fully integrated PDMS microfluidic of meta-atom SRR with a dual-gap structure is presented. A microfluidic channel is positioned in the gaps of the SRR, exploiting the electric field sensitivity for tuning and sensing applications. A single inlet port can be used to apply pneumatic pressure/suction to the microfluidic channel, altering the geometry of the SRR gaps. This structure exhibits a tunable resonant frequency due to expanding/deflating channel in the gaps. This proposed architecture offers integrated tuning capability without the use of external DC bias networks. Modifying the same structure so that the microfluidic channel yields two inlet/outlet

ports allows a liquid sample to be injected between the SRR gaps, resulting in a resonance frequency shift. The dielectric properties of the liquid sample can be predicted by employing an empirical relation between the SRR sensor resonance characteristics and the complex permittivity of the sample. The fabricated sensor has been evaluated and tested with water-ethanol and water-methanol mixtures, with good congruence to previously reported values in the literature. However, this microfluidic sensor offers a potential lab-on-chip solution for liquid dielectric characterization at microwave frequencies without external electrical connections.

4.2 PNEUMATIC TUNING OF A MICROFLUDIC SRR

The resonant frequency of a SRR is sensitive to any deformation of the structure especially in the gap area. This property has been exploited in this section with a fluidic SRR on an elastomeric PDMS substrate. Modification of the gap areas is enabled via microfluidic techniques, tuning the response using air injection and suction.

4.2.1 Tunable SRR Design

A meta-atom SRR structure with two gaps consists of patterned fluid metal Galinstan encapsulated in a PDMS microfluidic channel as shown in Figure 4.1. The SRR structure is chosen as a fundamental building block due to its simplicity and well-established design [1, 2]. The fluidic metal Galinstan is used as conductor for the SRR circuit, eliminating issues of conductor micro-cracking [124]. The SRR can be represented as an equivalent *LC* circuit where the gaps are associated with the capacitance (C_g) and the current path is related to the inductance (L) as in Figure 4.1(b).

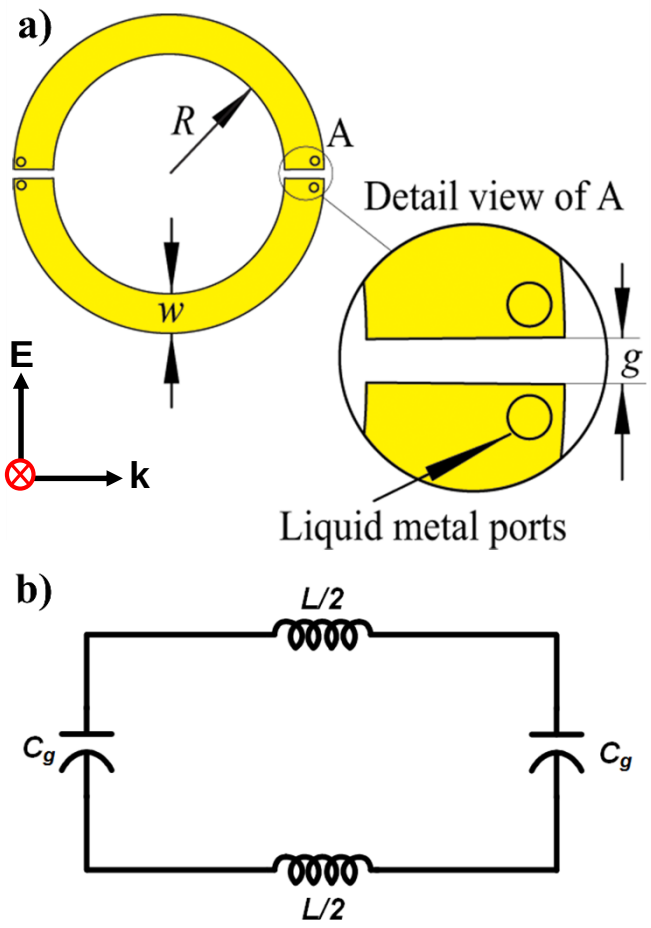

Figure 4.1 : a) Schematic of the SRR and b) its equivalent circuit.

The SRR was designed, optimized and simulated in CST microwave studio software in a WR-284 waveguide environment (covering S-band). The dimensions of the SRR are as follows: gap (g) = 0.8 mm, ring width (w) = 2.2 mm, radius of inner ring wall (R) = 6.4 mm. Figure 4.2 shows the simulated transmission response of the dual-gap SRR with a resonant dip at 3.2 GHz. Its corresponding electric field density is presented in the inset of Figure 4.2 with the gap regions exhibiting the highest localized electric field density.

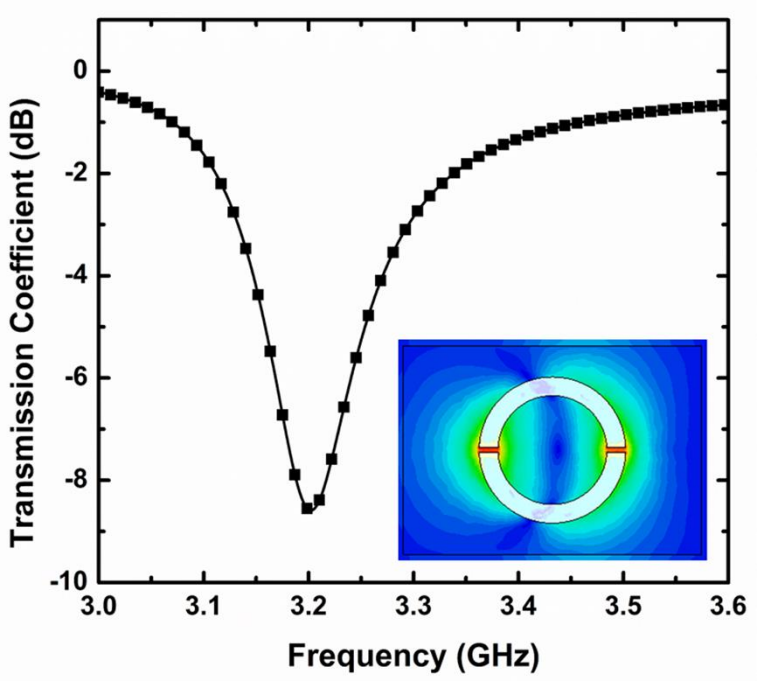

Figure 4.2 : Simulated resonance of the dual gap SRR of Fig. 4.1. (Inset) A strong electric field density at 3.2 GHz in between the gaps.

In order to make the resonant frequency of the SRR sensitive to structurally induced changes, a microfluidic channel with a width (w_f) of 0.4 mm is placed in between the gaps as shown in Figure 4.3 (a). The two gap SRR design enables the microfluidic channel to pass directly through the electromagnetic tuning structure. The corresponding simulation response is presented in Figure 4.3(b). The resonance frequency is shifted by 2.3% to a higher frequency of 3.27 GHz with the addition of the air filled microfluidic channel.

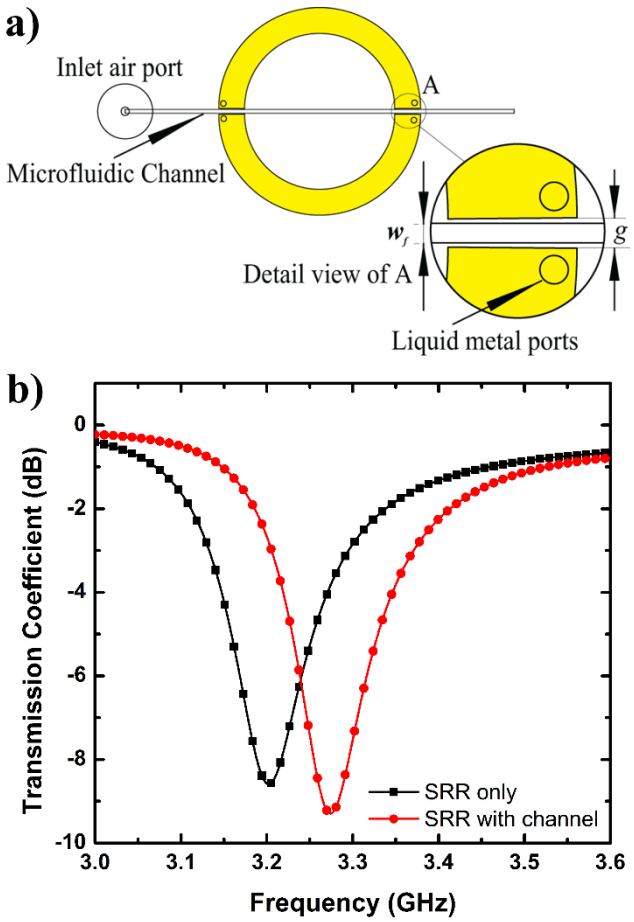

Figure 4.3 : (a) SRR with microfluidic channel, and (b) comparison simulated result with and without the microfluidic channel.

4.2.2 Fabrication process

The SRR micro-channels were fabricated in an elastomer, polydimethylsiloxane (PDMS Sylgard), using photolithography. A 4-inch silicon wafer was spin coated with a photoresist (SU-8 3050 MicroChem Corp.) using a spread cycle of 300 rpm and 100 rpm/s for 10 s and a development cycle of 500 rpm and 300 rpm/s for 30 s to get approximately 150 µm thickness. An edge-bead removal step was used as a second

stage for 30 s using edge-bead removal solvent.

The SU-8 coated wafer was soft-baked by first ramping the temperature at 110 ºC/hr starting from 23 ºC and holding at 65 ºC for 30 minutes and then second ramping the temperature at 50 ºC/hr and holding at 95 ºC for 30 minutes to dry out the solvent phase of the resist. This process was repeated two times, in order to achieve a film of approximately 300 µm thickness with good uniformity. Once the SU-8 film was baked, it was exposed with a pre-designed mask pattern of the SRR geometry for 3 min of UV on a MJB3 contact mask aligner with a wavelength of 360 nm and a power of 8 mW/cm^2. The mask was fabricated on a printed film (2400 dpi), using in-house Python scripts. After the UV exposure process, the polymeric cross-link process was finished by baking the sample on a hotplate for 1 min at 65 ºC and 15 min at 95 ºC. Then the sample was slowly cooled to room temperature. The unexposed SU-8 was developed for 30-45 min with periodic manual and gentle agitation to remove the unexposed material. After developing the SU-8 pattern, the wafer was cleaned with isopropanol and then rinsed with deionised (DI) water. A final step of hard bake was performed by leaving the sample to 120 ºC for 3 h. This process was done in order to improve and strengthen the cross-linked SU-8 pattern and extend the service life. The SU8 pattern was then ready for use as a mould for casting polymeric PDMS channels in series.

For fabrication of the SRR, standard microfabrication techniques for flexible device fabrication have been adapted as shown in Figure 4.4. The PDMS (Sylgard 184, Dow Corning Corporation) and its proprietary cross-linking agent were mixed at a ratio 10:1 ratio and degassed for 30 min. Then the PDMS mixture is spin-coated on the previously fabricated SU-8 patterned mould at 350 rpm for 30 s to obtain ~450 µm thickness, followed by the curing process.

When the PDMS is three-quarters cured, the 6 mm diameter of cylindrical PDMS blocks for the inlet/outlet connection to the syringes tube were added to each of the microfluidic channel edges. The curing process was continued and then peeled-off to produce an inverse replica of the mould. An inlet/outlet hole for the SRR patterns was made using a 0.75 mm biopsy punch. For the inlet/outlet connection to the syringes tubes, a 1 mm biopsy punch was used. Subsequently, the peeled-off structure was bonded onto another ~250 µm half-cured flat PDMS layer to form a stack microstructured channel. Then, the embedded microstructured was thermally-sealed on a hotplate at 70 °C for 20 min. Galinstan is injected into the SRR microchannel, and the inlet and outlet of the microfluidic channel are sealed by placing a drop of PDMS over the hole after the injection process is complete. Finally, the liquid metal SRR encapsulated in PDMS is carefully peeled off from the silicon carrier wafer to realise the flexible SRR as in Figure 4.5. This fabrication method allows for rapid prototyping, and a single ‘master’ can be re-used to produce many identical SRRs.

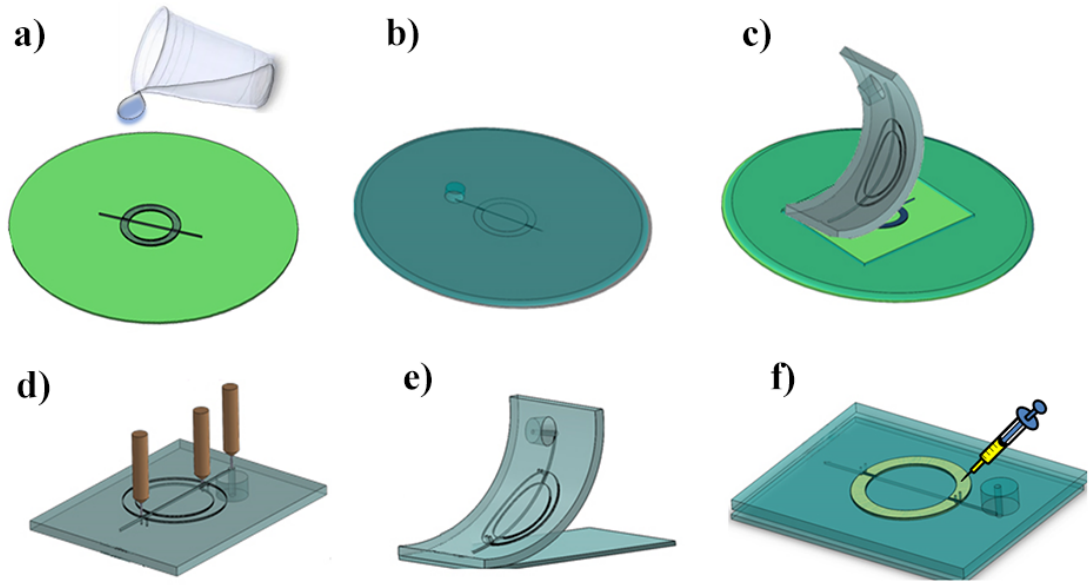

Figure 4.4 : Process illustration representing the sequence of the microfluidic SRR sensor fabrication: a) Photo-lithographically fabricated mould, b) PDMS layer over the mould with integrated PDMS-inlet air ports, c) Cut and peel off from the mould, d) Punch holes (air ports, liquid metal ports), e) Assembly with PDMS layer, and f) Final SSR device with liquid metal.

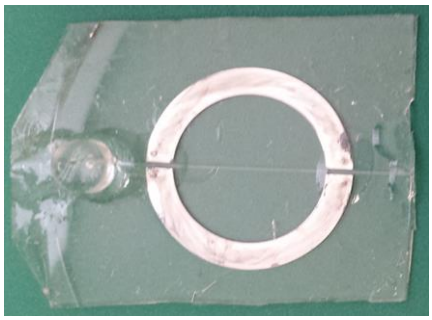

Figure 4.5 : A microfluidic, galinstan-filled and pneumatically tunable SRR.

4.2.3 Measurement Setup

The measurement of the SRR transmission coefficient response was carried out using WR-284 rectangular waveguides. Waveguides are connected to the two port of the network analyzer Agilent E5071B ENA through coaxial cables. The SRR was adhered to a flat foam substrate to assist in locating it in the middle of the waveguide flange as

in Figure 4.6. The waveguide has a tiny hole for allowing a Teflon tube to be attached to the SRR structure for the air injection and suction process.

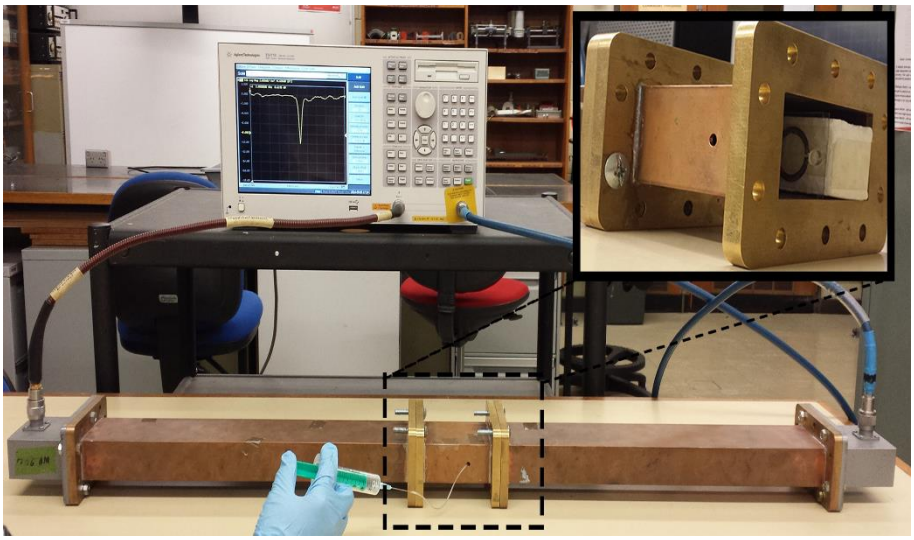

Figure 4.6 : The tuning measurement setup.

4.2.4 Experimental Validation

Figure 4.7 shows the measured transmission response for the corresponding applied air injection/suction. The relaxed microfluidic channel resonates at 3.295 GHz. Injection of 3 ml and 8 ml of air into the microfluidic channel, expanding the region between the gaps, shifting the resonant frequency higher. Under the maximum air injection, the resonant frequency is shifted approximately 2 %. With 6 ml air is sucked out from the microfluidic channel, deflating the channel/gap, the resonance shifted by 1 % to a lower frequency. This simple demonstration shows that pneumatic pressure in the microfluidic channel can tune the resonance frequency by 3 % (750 MHz). The results are summarized in Table 4.1.

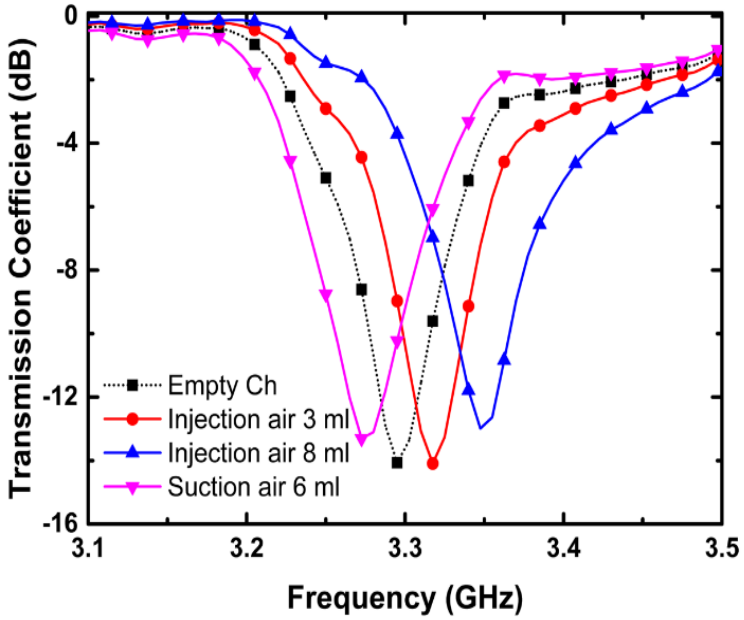

Figure 4.7 : Measured transmission coefficient for the dual gap SRR with air injection/suction.

Table 4.1 : Frequency tuning using air injection/suction.

	Frequency (GHz)	S_{21} (dB)	Changes of frequency (%)
Empty Channel	3.2950	-14.0666	-
Injection by 3 ml air	3.3175	-14.0924	~1 %
Injection by 8 ml air	3.3475	-12.9915	~2 %
Suction by 6 ml air	3.2725	-13.3048	~1 %

4.3 NON-CONTACT DIELECTRIC SENSOR

In this section, a fully-integrated of PDMS microfluidic sensor based on a meta-atom SRR is presented. The built-in microfluidic sensing channel is designed to pass internally through the SRR gaps, as this region is sensitive to dielectric changes. No additional external microfluidic channel is attached to the SRR. The sensor determines the complex permittivity of a liquid sample based on the change of the measured resonant frequency and peak attenuation. As the proposed sensor is also directly excited by an incident electromagnetic field without physical connections, the sensor system offers contactless, reusable, non-invasive, label-free sensing solution that has the potential to be implemented in a lab-on-a-chip system.

4.3.1 Theory

Figure 4.8(a) shows a SRR structure representing a main component of the proposed microfluidic sensor. The structure of this sensor is similar to the microfluidic SRR in Section 4.2.1, however an extra outlet port is accessed for the purpose of dielectric fluid characterisation. The microfluidic channel with width (w_f) of 0.4 mm is purposely patterned between the gaps of the SRR. As a liquid flows through this patterned channel its dielectric property will shift the SRR natural resonance allowing for a measurement of the fluids permittivity. The SRR can be modelled as an equivalent *LC* circuit where the gap is associated with the capacitance (C_g) and the current path is related to the inductance (L) as in Figure 4.8(b). The two gap design also permits the realisation of an integrated meta-surface SRR sensor to increase sensitivity as illustrated in Figure 4.8(c), and allows free space measurement techniques to be employed to rapidly evaluate samples.

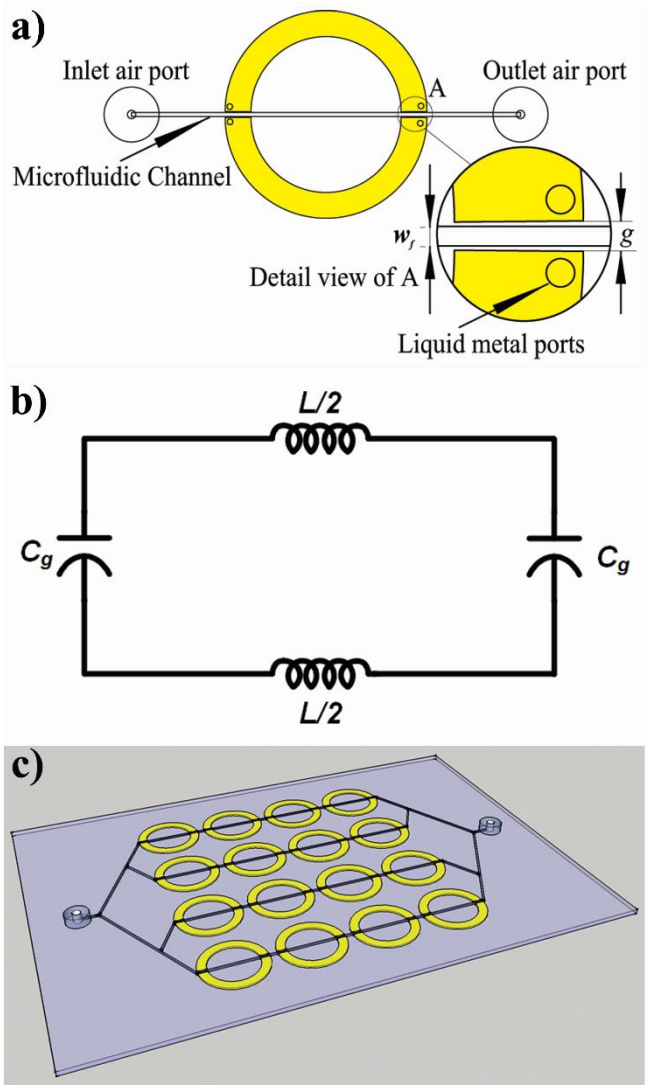

Figure 4.8 : a) Schematic of the meta-atom SRR sensor, b) its equivalent circuit, and c) an integrated meta-surface SRR sensor Parameters: g = 0.8 mm and w_f = 0.4 mm

The values of effective capacitance are influenced by the dielectric materials around the gaps, and can be approximately estimated by [107] :

$$C_g = C_o + \varepsilon_{sam} C_c \tag{4.1}$$

where C_o is the capacitance due to the dielectric separation between the microfluidic channel and the SRR. The term $\varepsilon_{sam}C_c$ describes the contribution from the loaded liquid sample with C_c being the capacitance of an empty channel, and $\varepsilon_{sam} = \varepsilon'_{sam} + j\varepsilon''_{sam}$ the complex permittivity of the sample.

The resonant frequency (f_o) of the SRR can be defined as:

$$f_o = \frac{1}{2\pi\sqrt{L(C_g)}} \tag{4.2}$$

And the quality factor (Q) of the resonance is:

$$Q = \frac{1}{R}\sqrt{\frac{L}{C_g}} \tag{4.3}$$

Therefore, from equations (4.1) - (4.3), the resonance frequency and the quality factor will be functions of the liquid sample permittivity or

$$f_o = F_1\left(\varepsilon'_{sam}, \varepsilon''_{sam}\right) \text{ and } Q = F_2\left(\varepsilon'_{sam}, \varepsilon''_{sam}\right) \tag{4.4}$$

This indicates that the resonance characteristics of the SRR are also influenced by the complex permittivity of a liquid sample. Thus, the complex permittivity of an unknown liquid sample can be determined simply by measuring the transmission resonance characteristics.

4.3.2 Fabrication and Measurement setup:

The fabrication process is the same as described in Section 4.2.2, with an additional outlet port on the microfluidic channel for liquid sample infiltration, as seen in Figure 4.9.

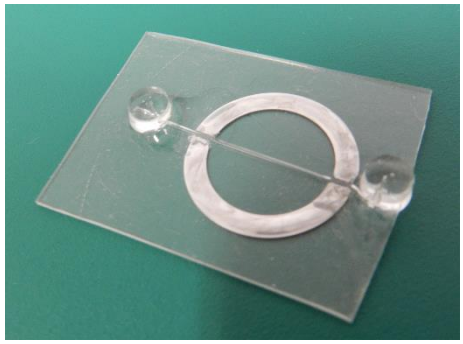

Figure 4.9 : A microfluidic, galinstan-filled SRR sensor.

The sensing experimental setup is shown in Figure 4.10. The measurement of the SRR transmission properties was carried out using a WR-284 rectangular waveguide and an Agilent E5071B ENA series vector network analyser. The SRR was adhered to a flat foam substrate to assist in locating it in the middle of the waveguide. The SRR is excited by the magnetic field perpendicular to the element plane, as indicated in inset of Figure 4.10.

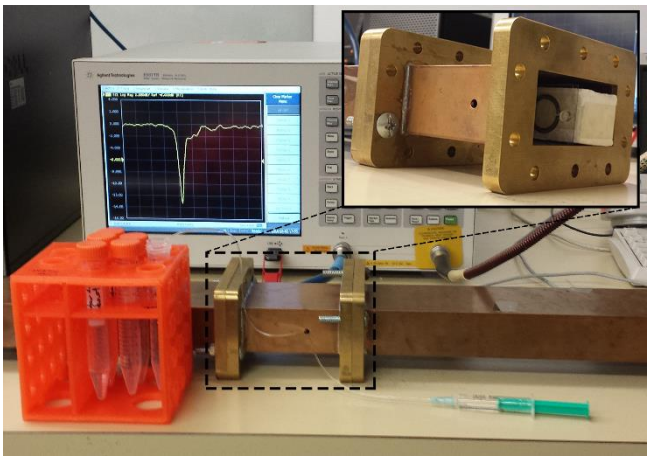

Figure 4.10: The complete experimental sensing setup.

In a similar method to Ref. [107, 108], the sensing measurements are performed based on a stop-flow technique. A binary solution of deionized (DI) water-ethanol mixture and water-methanol mixture are used as fluid sample for testing since it provides a broad range of the complex permittivity at the low microwave frequency range [125]. Teflon tubes are connected to the inlet and outlet of the microfluidic channel. The microchannel is filled with the liquid sample via attached syringe and then the flow is stopped for measurement. A very low pressure is applied to the syringe to avoid channel deformation. Subsequently, the resonance frequency and peak attenuation parameters are recorded to characterize the liquid test samples.

The empty microfluidic channel between the gaps of the SRR provides a baseline measurement and comparison to simulation. The maximum value of resonance frequency and peak attenuation are recorded when the empty microchannel channel is measured as highlight in Figure 4.11. The measured results exhibit a slightly lower resonant frequency compared to simulation by ~1.1%. The differences in the transmission coefficient between the simulation and experimental results are caused by fabrication tolerances and the location accuracy inside the waveguide.

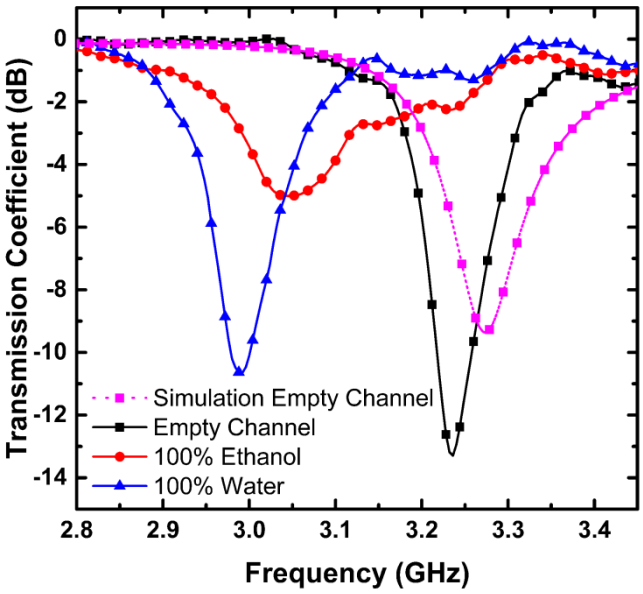

Figure 4.11: Measured transmission response of the sensor in different conditions.

4.3.3 Sensor Characteristics:

As mentioned earlier, the complex permittivity of the test sample contributes to the changes of the resonance frequency and Q factor of the SRR. For characterizing the complex permittivity of the samples, a set of experiments have been performed using binary mixtures of DI water-ethanol. The dielectric properties of water-ethanol and water-methanol mixtures studied in [125] are used as reference. Figure 4.12 depicts the complex permittivity of the water–ethanol mixture at 3 GHz obtained by curve fitting to the literature values in [125]. Dispersion is not taken into account, since the resonance shift is within a narrow frequency band.

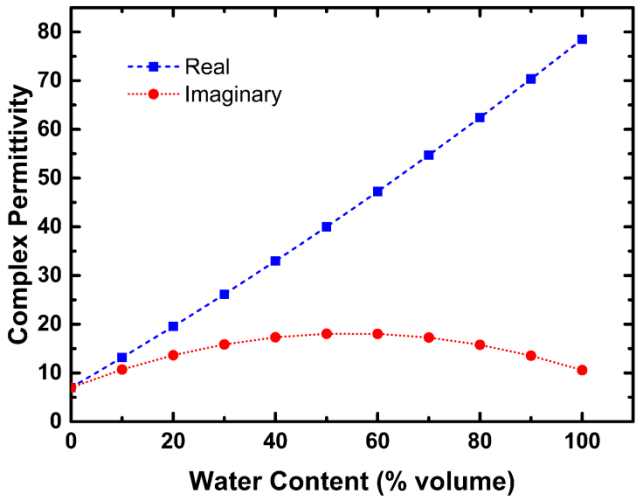

Figure 4.12: Complex permittivity of water–ethanol mixture. The mixture permittivity at 3 GHz is shown as a function of the water content. The values are taken from [125] with polynomial fitting to smooth the curves within the confidence interval.

In similar manner [107, 108], the simplified model that relates changes in the complex permittivity to variations in the resonance frequency and peak attenuation can be expressed in the matrix form as:

$$\begin{bmatrix} \Delta f_0 \\ \Delta|S_{21}| \end{bmatrix} = \begin{bmatrix} m_{11} & m_{12} \\ m_{21} & m_{22} \end{bmatrix} \begin{bmatrix} \Delta\varepsilon'_{sam} \\ \Delta\varepsilon''_{sam} \end{bmatrix} \tag{4.5}$$

where $\Delta\varepsilon'_{sam} = \varepsilon'_{sam} - \varepsilon'_{ref}$, $\Delta\varepsilon''_{sam} = \varepsilon''_{sam} - \varepsilon''_{ref}$, $\Delta f_{Osam} = f_{Osam} - f_{Oref}$, and $\Delta|S_{21}| = |S_{21}|_{sam} - |S_{21}|_{ref}$, with the subscript 'sam' for the sample and 'ref' for the reference mixture. The values for $|S_{21}|_{sam}$ and $|S_{21}|_{ref}$ in the matrix are determined at f_{Osam} and f_{Oref} respectively. Here, the mixture with a 50% water fraction is considered as the reference.

The complex permittivity values of the test fluid samples extracted from Figure 4.12 are summarized in Table 4.2. For the first set of measurements, the volume fraction of water is changed from 10% to 90% with a step size of 20% at each step, the resonance frequency and peak attenuation of the sensor are recorded giving a data set of 5 samples. The measurement results of the resonance frequency and maximum attenuation for the 5 test samples are shown in Figure 4.13. The resonance frequency is shifted from 3.05 GHz down to 2.99 GHz as the water volume fraction increases from 10% to 90%. The peak attenuation will be minimum for pure ethanol, or when the water volume fraction is 0%.

Table 4.2 : Complex permittivity of the water–ethanol mixture at 3 GHz [125]. The volume fraction of water is changed from 10% to 90% for device testing.

Water Fraction %	ε'	ε''	Δε'	Δε''
10	13.2	10.7	-26.8	-7.3
30	26.1	15.8	-13.9	-2.2
50	40.0	18.0	0.0	0.0
70	54.7	17.3	14.7	-0.8
90	70.3	13.5	30.4	-4.5

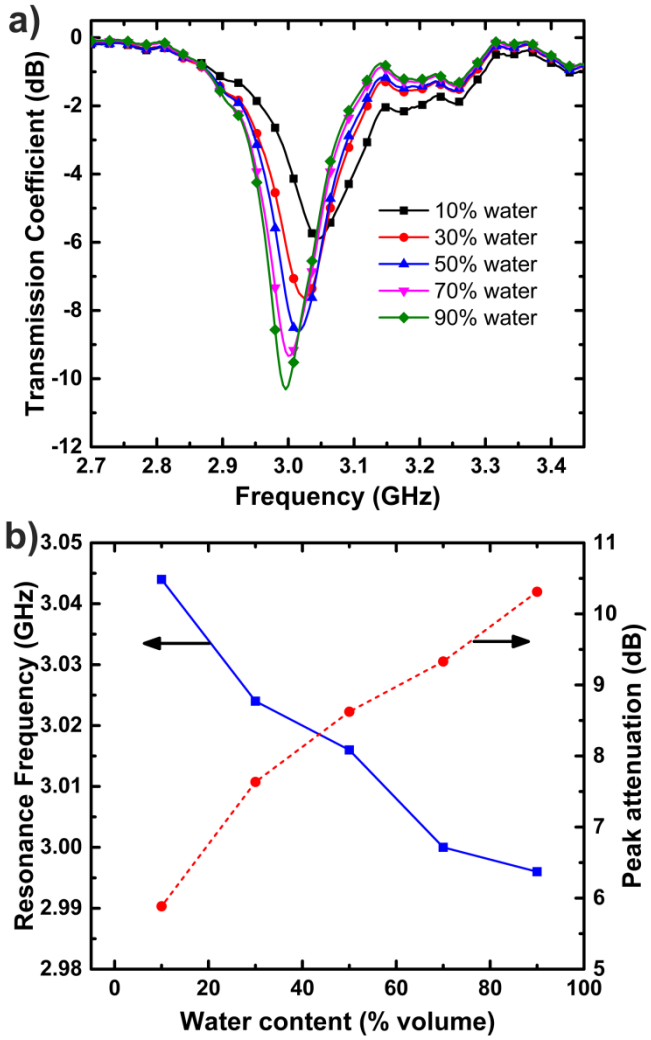

Figure 4.13 : The measured transmission response of the water–ethanol test samples for calibration of the sensor. The water volume fraction is changed from 10% to 90% with the step size of 20%. (b) Corresponding resonance frequency and peak attenuation at different steps.

The unknown coefficients of the model in equation (4.5) are over determined by test datasets. The least-squares method explained in Ref. [107] can be used to approximate the unknown coefficients. The benefit of this model is that all the fabrication tolerances of the device are fully taken into account. Three matrices are set up from the reported complex permittivity in Table 4.2 [125], measured resonance frequency, and measured S_{21}, as:

$$X = \begin{bmatrix} \Delta\varepsilon'_{sam1} & \Delta\varepsilon''_{sam1} \\ \Delta\varepsilon'_{sam2} & \Delta\varepsilon''_{sam2} \\ \vdots & \vdots \\ \Delta\varepsilon'_{sam5} & \Delta\varepsilon''_{sam5} \end{bmatrix}, Y_1 = \begin{bmatrix} \Delta f_1 \\ \Delta f_2 \\ \vdots \\ \Delta f_5 \end{bmatrix} \; and \; Y_2 = \begin{bmatrix} \Delta|S_{21}|_{sam1} \\ \Delta|S_{21}|_{sam2} \\ \vdots \\ \Delta|S_{21}|_{sam5} \end{bmatrix} \quad (4.6)$$

The unknown coefficients can be calculated from:

$$[m_{11} \quad m_{12}]^T = (X^T X)^{-1} X^T Y_1 \quad (4.7)$$

$$[m_{21} \quad m_{22}]^T = (X^T X)^{-1} X^T Y_2 \quad (4.8)$$

These equations yield the characteristic matrix that relates the complex permittivity of the liquid under test with the resonance properties as:

$$\begin{bmatrix} \Delta f_0 \\ \Delta|S_{21}| \end{bmatrix} = \begin{bmatrix} -0.0008 & 0.0007 \\ -0.0025 & -0.3861 \end{bmatrix} \begin{bmatrix} \Delta\varepsilon'_{sam} \\ \Delta\varepsilon''_{sam} \end{bmatrix} \quad (4.9)$$

The sensor module can be exclusively described by this set of equations, which fully takes into account deviations in the dimensions and properties of constructing materials. Through the matrix inversion, equation (4.9) yields:

$$\begin{bmatrix} \Delta\varepsilon'_{sam} \\ \Delta\varepsilon''_{sam} \end{bmatrix} = \begin{bmatrix} -1257.12 & 2.27917 \\ 8.1399 & -2.60476 \end{bmatrix} \begin{bmatrix} \Delta f_0 \\ \Delta|S_{21}| \end{bmatrix} \quad (4.10)$$

This empirical model can be used to determine the complex permittivity of unknown liquid samples just simply measuring the resonance characteristics.

4.3.4 Experimental Validation

To demonstrate the validity of the presented sensor model in equation (10), firstly, the water-ethanol mixture with the volume fraction of water is changed from 0% to 100% with the step size of 20% giving 6 data sets of measurement are used. The measured transmission responses of the sensor for these sets of samples are shown in Figure 4.14

together with the extracted resonance frequency and peak attenuation. The resonance frequencies shift to higher frequency and the Q factors decrease by increasing the ethanol concentrations in water mixtures.

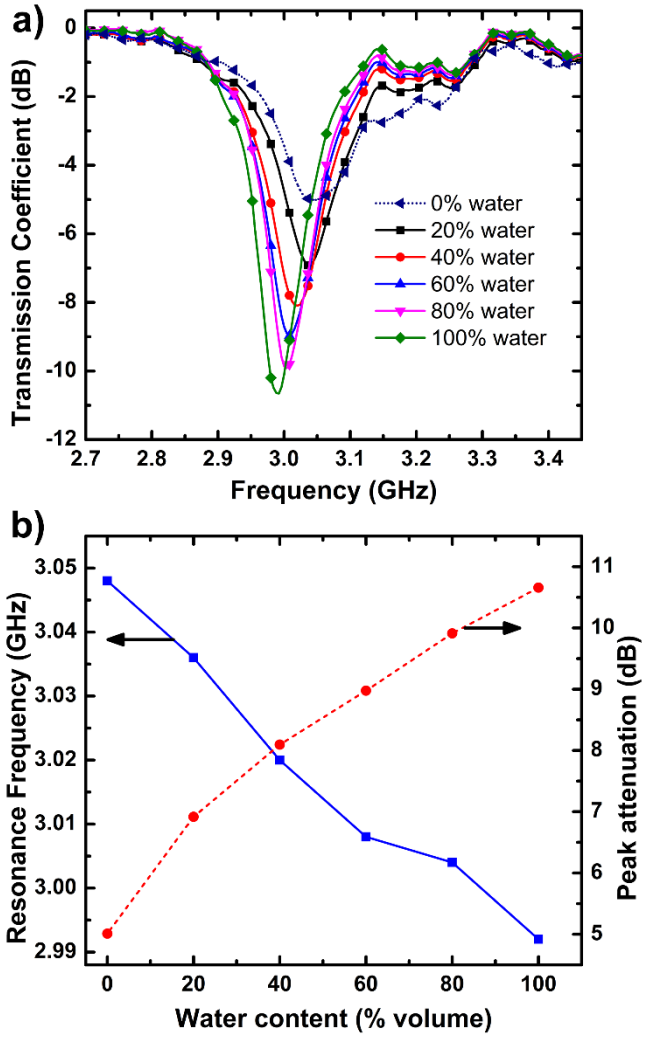

Figure 4.14 : The measured transmission response of the water–ethanol test samples for validating of the simplified model. The water volume fraction is changed from 20% to 100% with the step size of 20%. (b) Corresponding resonance frequency and peak attenuation at different steps

The model presented in equation (4.10) is used to determine the $\Delta\varepsilon'$ and $\Delta\varepsilon''$ for each couples of measured resonance frequency and peak attenuation, where 50% water-ethanol mixture is considered as the reference. Then, the complex permittivity of each sample can be calculated as

$$\varepsilon'_{sam} = \varepsilon'_{ref} + \Delta\varepsilon'_{\mathrm{mod}} \tag{4.11}$$

$$\varepsilon''_{sam} = \varepsilon''_{ref} + \Delta\varepsilon''_{\mathrm{mod}} \tag{4.12}$$

with a subscript ‘mod’ for the values obtained from equation (4.10). The attained complex permittivity values of the samples are compared with the literature values as shown in Figure 4.15. The obtained results show a good agreement with the literature [125].

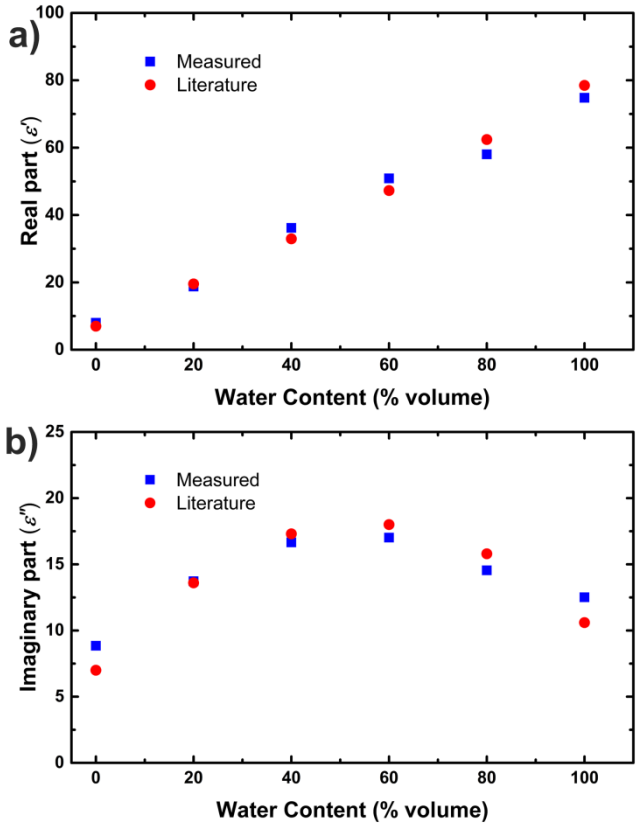

Figure 4.15 : Comparison between the predicted and literature values of complex permittivity for the water–ethanol mixture at around 3 GHz. The volume fraction of water is changed from 0% to 100% with the step size of 20%. (a) Real part of the complex permittivity. (b) Imaginary part of the complex permittivity

Secondly, a mixture of water–methanol is chosen to further validate this model. Pure methanol has the complex permittivity of 20 + 14j at 3 GHz. The transmission response of the sensor for different concentrations of water–methanol mixture was measured, and the resonant frequency and peak attenuation were extracted, as given in Figure 4.16. Similar steps to above are used to determine the $\Delta\varepsilon'$ and $\Delta\varepsilon''$ of these mixtures. The results from the microfluidic sensor measurement are plotted against the literature values [125] as a function of the concentration in Figure 4.17. These results show good accuracy comparing to the literature.

The discrepancies between the measured and literature values of complex permittivity are potentially caused by measurement uncertainties or the simplified linear approximation of the sensing model. The measured results also show the same order of accuracy against the literature values as previously reported results using a similar method [107].

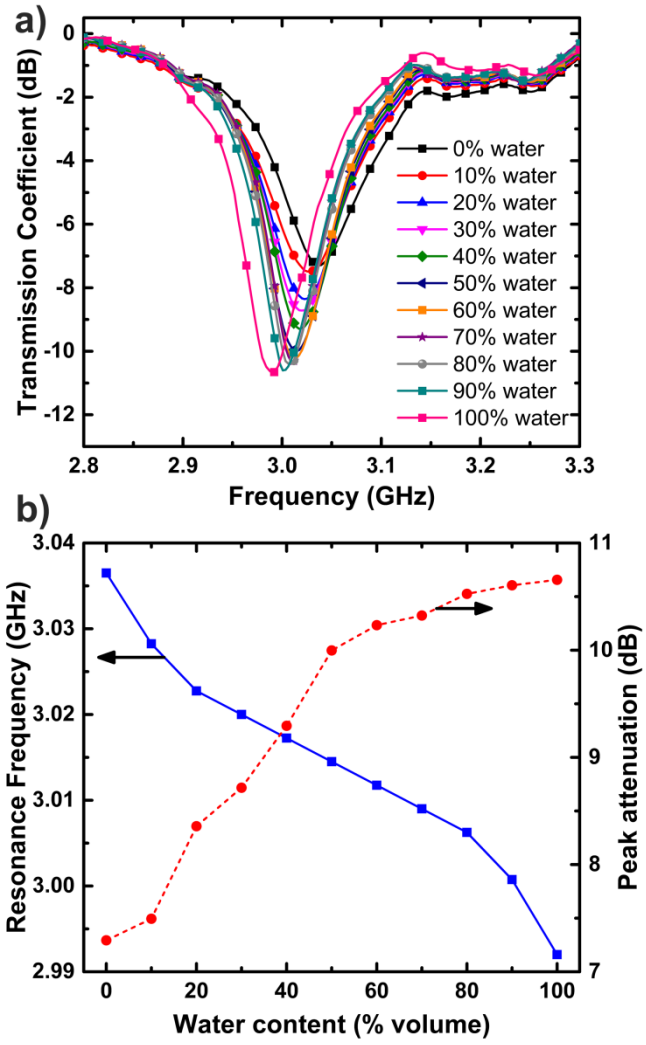

Figure 4.16 : The measured transmission response of the water–methanol test samples for validating of the simplified model. The water volume fraction is changed from 0% to 100% with the step size of 0%. (b) Corresponding resonance frequency and peak attenuation at different steps.

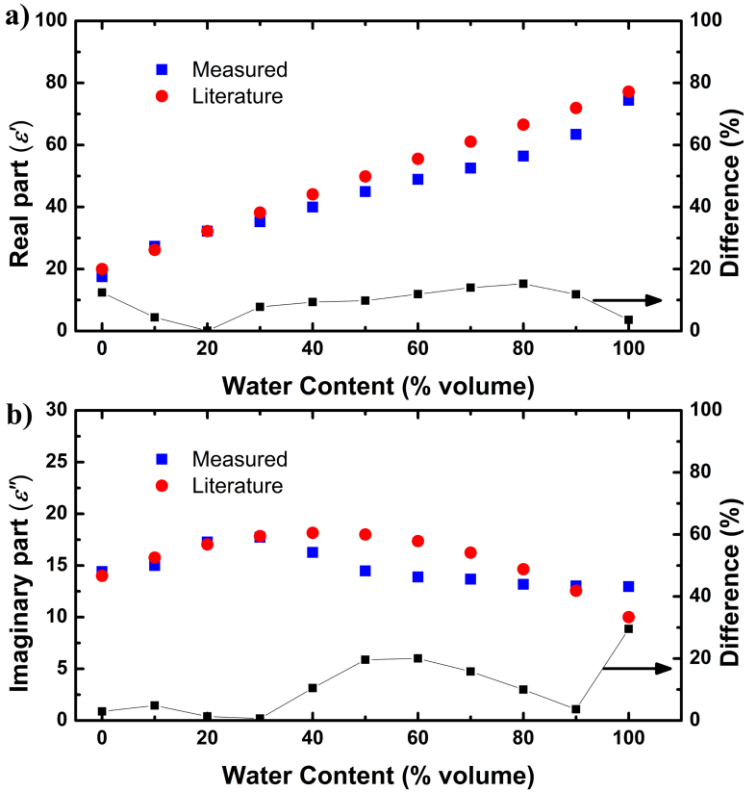

Figure 4.17 : Comparison between the predicted and literature values of complex permittivity for the water–methanol mixture at around 3 GHz. The volume fraction of water is changed from 0% to 100% with the step size of 10%. (a) Real part of the complex permittivity. (b) Imaginary part of the complex permittivity.

To further investigate the complex permittivity of the water–methanol mixtures, the sensor characteristic measurement steps as explained in Section 4.3.3 were again conducted, this time with 10%, 30%, 50%, 70% and 90% water-methanol mixtures as the calibrations mixtures. The details of the sensor characteristic calculation process are discussed in Appendix A. Subsequently, the transmission response for 20%, 40%, 60%, 80% and 100% concentrations of water–methanol mixtures were measured, and using similar steps to above the resonant frequency and peak attenuation were extracted, as given in Figure 4.18. The measured complex permittivity of the water–methanol mixture samples are plotted in Figure 4.19, showing very good congruence with the

literature values [125]. Thus, the results show for accurate characterisation of a particular mixture, calibration with that mixture is optimal.

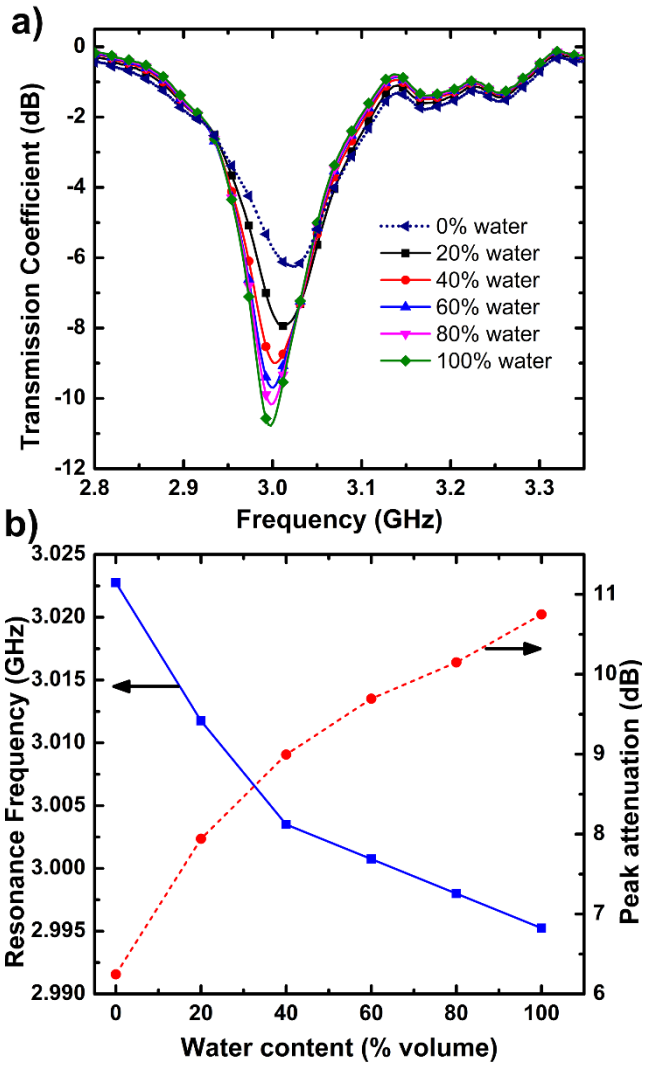

Figure 4.18 : The measured transmission response of the water-methanol test samples for validating of the simplified model. The water volume fraction is changed from 0% to 100% with the step size of 20%. (b) Corresponding resonance frequency and peak attenuation at different steps.

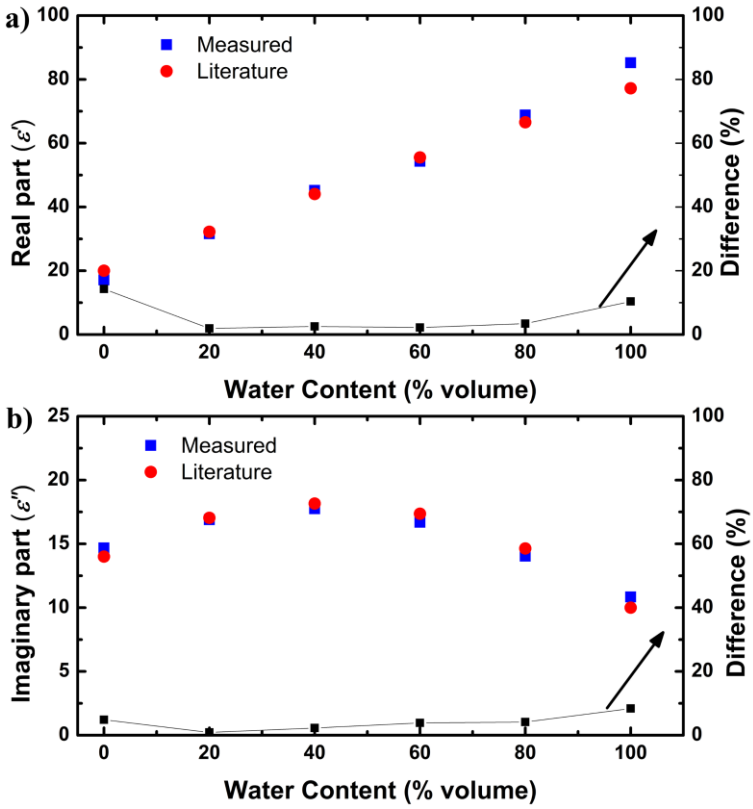

Figure 4.19 : Comparison between the predicted and literature values of complex permittivity for the water-methanol mixture at 3 GHz. The volume fraction of water is changed from 0% to 100% with the step size of 20%. (a) Real part of the complex permittivity. (b) Imaginary part of the complex permittivity

4.4 SUMMARY AND OUTLOOK

In this chapter, a meta-atom dual gap SRR has been proposed which incorporates a narrow microfluidic channel in its highly capacitive region. This modification results into two individual applications: a frequency tunable electromagnetic element and a non-contact dielectric fluid sensor.

A PDMS based microfluidic meta-atom SRR is made tunable using pneumatic air injection/suction. The resulting microchannel expansion/deflation in the gaps of a SRR produced 3% frequency tuning. The proposed method offers an integrated tuning

capability without any DC bias circuits which may interfere with the electromagnetic response of the meta-atom.

A microfluidic meta-atom SRR based sensor is also presented. Injecting liquid samples into a microfluidic sensing channel between the sensitive gaps of a SRR allows the resonator to characterize the dielectric properties of the liquid sample. An empirical model derived from the measured resonance frequency characteristics of the sensor has been established, enabling the dielectric properties of the liquid sample to be determined with good accuracy. For validation, the dielectric properties of binary water-ethanol and water-methanol mixtures are successfully estimated, and are congruent with the literature. The sensor is directly excited by an incident field without physical electrical connections, and the fluid infiltration process is confined in a microfluidic channel. Thus, the proposed microfluidic SRR sensor is well suited to be incorporated in a lab-on-chip system for non-contact liquid dielectric characterisation.

CHAPTER 5

ELASTOMERIC COMPOSITES FOR FLEXIBLE MICROWAVE SUBSTRATES

5.1 INTRODUCTION

In Chapters 3 and 4, the research was focused on realising fluidic SRRs that can exhibit mechanical tolerance, or alternatively for tuning and sensing applications. The fabrication of the proposed SRRs utilised PDMS as flexible substrate. Notably, the PDMS is known for having a considerable dielectric loss tangent which can degrade performance of EM devices.

Manipulating dielectric properties of polydimethylsiloxane (PDMS) is an important consideration for flexible, low-loss microwave devices design. Therefore, in this chapter, a method for reducing dielectric loss (*tan* δ) by forming PDMS composites loaded with either alumina (Al_2O_3) or polytetrafluoroethylene (PTFE) particles has been studied. Different concentrations of alumina or PTFE nano/microparticles are mixed within a PDMS matrix. Their structural, mechanical and microwave properties will be investigated, and the microwave dielectric properties of the composites are measured using a waveguide resonant cavity method at 10 GHz. Theoretical mixing modeling approaches have be used to predict the relative permittivity (ε_r) of PDMS composites, and a comparison is made between the measured ε_r and those of the mixing laws models. The results show that incorporation of either low dielectric loss filler in the PDMS matrix (up to 50 wt% filler loading) significantly reduces the dielectric loss

while maintaining the flexibility of the host matrix. The fillers can also be used to control the dielectric permittivity of the composite, either increasing or decreasing relative permittivity from that of PDMS for a certain filler type and wt%.

The dielectric properties over X-band frequencies (8–12 GHz) have also been investigated using waveguide transmission/reflection measurement method to validate the measured result by the waveguide resonant cavity method, and to examine the variance versus frequency.

5.2 MATERIAL AND COMPOSITE SAMPLE PREPARATIONS

To investigate the impact of the composite fillers on the permittivity and dielectric loss of PDMS, the following preparation process was used. Dow Corning's Sylgard 184^{TM} PDMS with relative permittivity (ε_r) of 2.68 and dielectric loss (tan δ) of 0.00133 at 100 kHz was selected as the host phase, as it has been commonly used in practical applications [1, 45, 78]. The properties of PDMS have been measured using a coaxial dielectric probe (Agilent Technologies, Model 85070E) to give ε_r = 3.0 and tan δ = 0.05 at 3.45 GHz [79]. At frequencies up to 20 GHz, PDMS has the reported properties of ε_r = 2.72 and loss tangent ranging from 0.0366 to 0.0433 (0.055–0.065 dB.cm^{-1}.GHz^{-1}) [45]. The PDMS properties can be dependent on the preparation process. Hence, in this work the composites will be benchmarked against measured values of PDMS prepared in the same fashion. Alumina nanoparticles (average dimension < 50 nm) and PTFE microparticles (average dimension < 10 μm) purchased from Sigma-Aldrich, Australia were used as the filler phase. The alumina nanoparticles were pre-baked at 100 ºC for seven days to remove any additional moisture content which could introduce additional

loss in the resulting composite [62].

The process begins with the preparation of PDMS by adding one part (by weight) of a proprietary curing/crosslinking agent (Sylgard 184, Dow Corning Corporation) to ten parts (by weight) of PDMS pre-polymer. The desired amount of filler particles were added to the PDMS mixture and heavy stirring by hand was applied for 10 min. Because of higher filler loadings (particularly the 50 wt%), a magnetic stirrer or any other controllable stirrer cannot be used as the mixture forms a thick paste. The obtained PDMS composites were degassed in a vacuum oven for ~1 h to remove air bubbles. The resulting fully degassed mixture was molded into a bar-shape of 3.2 mm × 3.2 mm × 10 mm size and cured for solidification at room temperature for ~24 h. Samples with filler concentration of 15 wt% (4.35 vol%), 30 wt% (9.94 vol%), and 50 wt% (20.48 vol%) for PDMS/alumina composites, and 15 wt% (7.80 vol%), 30 wt% (17.03 vol%), and 50 wt% (32.39 vol%) PDMS/PTFE composites were prepared using this method.

The same preparation steps were applied to create samples for tensile strain, moisture absorption, density and swelling measurements. For the tensile stress-strain measurement, a composite sheet of ~2 mm thickness was prepared. The composite sheets were die cut into dumb-bell shapes with an overall length of 75 mm, a 30 mm long narrow section with a width of 4 mm, and gauge width of 12 mm. For the moisture absorption, density and swelling measurements, a sample dimension of 3.2 mm × 3.2 mm × 20 mm size was used as shown Figure 5.1.

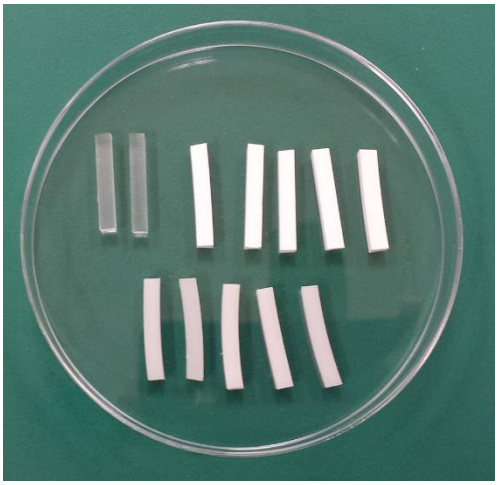

Figure 5.1 : The 3.2 mm × 3.2 mm × 20 mm size of PDMS and PDMS composite samples.

5.3 CHARACTERIZATION METHODS

5.3.1 Scanning Electron Microscope (SEM) measurement

SEM is a common technique to characterise micro/nanomaterials by providing information about the material's surface morphology, topography and composition. The surface of the material is scanned with an electron beam that interacts with the atoms of the material and emits secondary electrons which are detected and monitored. The microstructure of the composites was examined using an environmental scanning electron microscope (ESEM, FEI Quanta 200) at the RMIT Microscopy & Microanalysis Facility (RMMF) (See Figure 5.2).

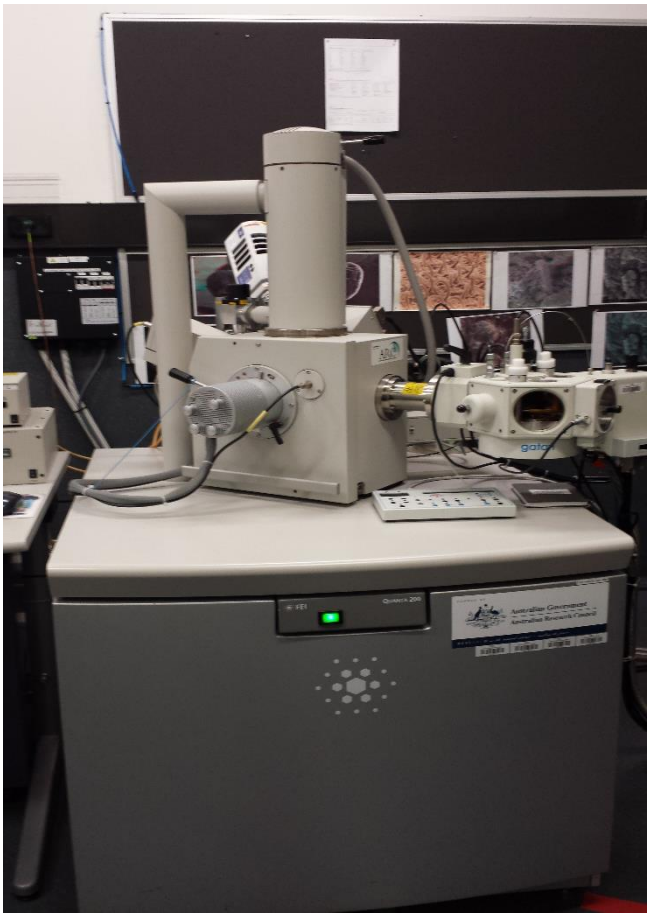

Figure 5.2 : ESEM, FEI Quanta 200

5.3.2 Tensile stress-strain measurement

The tensile stress-strain of pure PDMS, PDMS/alumina nanocomposites and PDMS/PTFE microcomposites were measured using a Universal Testing Machine (UTM; WL 2100; Instron, Norwood, MA) (See Figure 5.3(a)). The specimen stripe used for the testing is shown in Figure 5.3 (b).

Each specimen is locked to a force gauge and can be programmed to move along the vertical axis with a rate of grip separation of 500 mm/min. The force gauge is connected to a computer for real time monitoring of the force. The specimen is slowly stretched until it breaks.

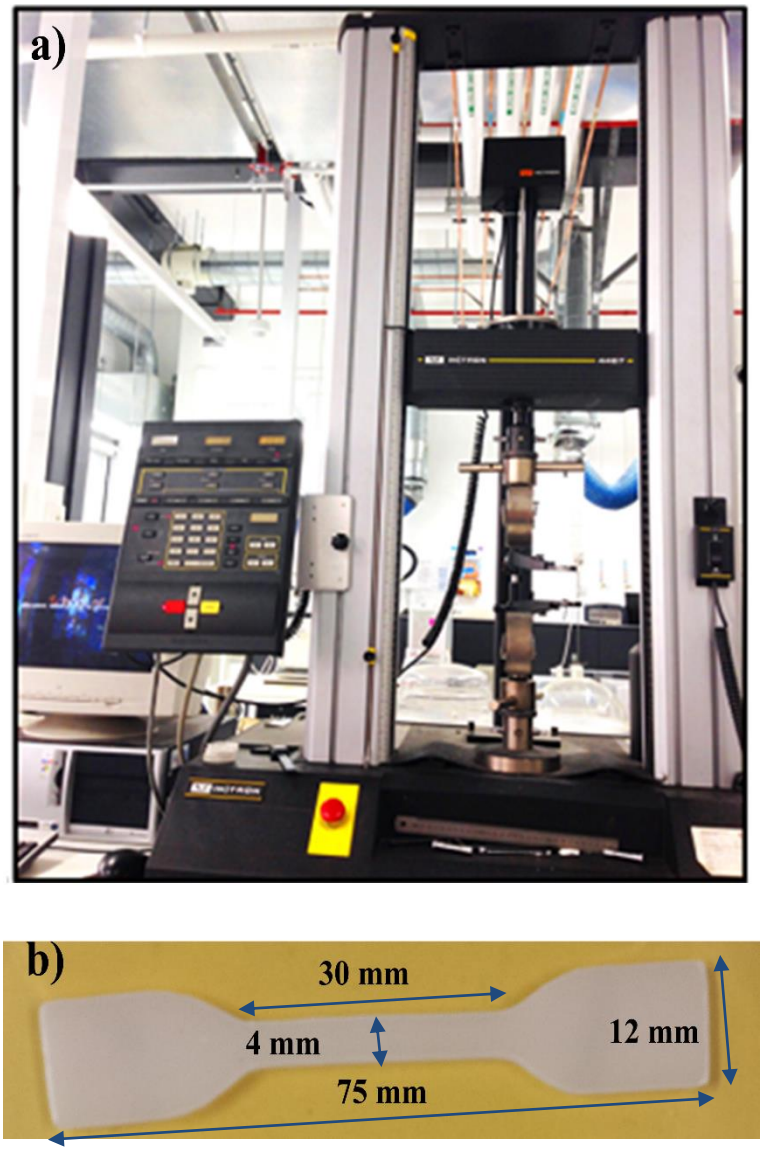

Figure 5.3 : a) Universal testing machine, and b) PDMS composite specimen for strain-stress measurement.

5.3.3 Density measurement

Archimedes' principle was used to determine the density of the composites [126]. The samples were dried for 1 h at 110 ºC in an oven and weighed in air (W_{air}). Then, they were carefully immersed in 2-propanol fluid and immediate weight was taken ($W_{2\text{-propanol}}$). The measured density of the composite was calculated using the following equation:

$$\rho_{mea} = \frac{W_{air}\,\rho_{2-propanol}}{W_{air} - W_{2-propanol}} \tag{5.1}$$

where ρ_{mea} is the measured density of the composite, $\rho_{2-propanol}$ is the density of 2-propanol fluid of 0.789 g/cm^3, W_{air} is the weight of the sample in air and $W_{2\text{-propanol}}$ is the weight of the sample in 2-propanol fluid.

5.3.4 Dielectric property measurement

The dielectric properties of the PDMS composites were measured using a rectangular waveguide cavity resonant method. The cavity was custom-built to resonate at 10 GHz using a section of WR-90 waveguide with irises at either end, as shown in Figure 5.4. Although the results are at single frequency, they should not vary greatly over X-band (8−12 GHz). A bar-shaped sample is located in the position of the maximum electric field for the TE_{107} mode, causing a shift of the resonant frequency and a decrease of the quality factor of the cavity. The real (ε'_r) and imaginary (ε''_r) parts of the PDMS composite permittivity can then be calculated from the changes of the resonant frequency and quality factor of the cavity, respectively[127]. The dielectric loss (tan δ) is the ratio of imaginary part to the real part of the permittivity.

$$\varepsilon'_r = \frac{V_c(f_c - f_s)}{2V_s f_s} + 1 \tag{5.2}$$

$$\varepsilon''_r = \frac{V_c}{4V_s}\left(\frac{1}{Q_s} - \frac{1}{Q_c}\right) \tag{5.3}$$

where f_c and f_s are the resonant frequencies, Q_c and Q_s are the quality factors of the cavity without and with the sample inside the cavity, respectively, and V_c and V_s are the volumes of the cavity and sample, respectively. The validity of the experimental setup is determined by measuring a standard of Rogers RT/Duroid 5880 material. To ensure the repeatability and accuracy of the measurement, five different samples of each individual composite are measured, and the average value of dielectric permittivity and loss tangent was calculated and plotted.

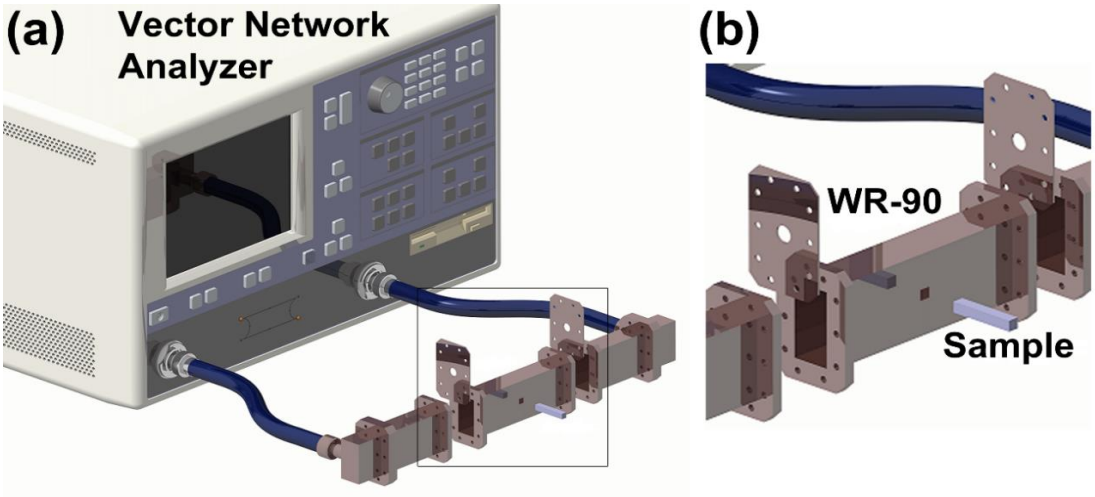

Figure 5.4 : Experimental setup for dielectric property measurement of PDMS composites. (a) The interfacing of the WR-90 waveguide to the vector network analyzer is shown. (b) A magnified view of the boxed region in (a) showing the position of the sample in the waveguide.

For calculating the ε_r using the theoretical mixing laws [66, 128], the volume fraction (V_f) of alumina and PTFE particles for a given weight fraction (W_f) can be determined using the equation:

$$V_f = \frac{W_f}{W_f + W_m(\rho_f/\rho_m)} \tag{5.4}$$

where ρ_f is the density of the filler particles, and W_m and ρ_m are the weight fraction and density of PDMS matrix, respectively.

5.3.5 Moisture absorption measurement

Moisture absorption of the composites was also measured. Test samples were initially desiccated at 110 ºC for 1 h in an oven. Weight of the samples was taken in air and then submerged in deionized water at room temperature 25 ºC for 24 h. The specimens were taken out and the excess water from the surface was removed by carefully wiping with a dry cloth followed by immediate weighing. The water absorption of the composite is calculated from the weight gain.

5.3.6 Solvent Swelling measurement

Solvent swelling measurements were also carried out. Test samples were initially pre-weighed and then totally immersed in pure toluene at room temperature (25 ºC) for 24 h until equilibrium swelling was reached. The swollen samples were then taken out and, after the excess toluene from the surface was carefully removed by wiping with a dry cloth, immediately weighed. To ensure repeatable results, the measurement was repeated three times.

5.4 RESULTS AND DISCUSSION

5.4.1 SEM of the PDMS composites

Figure 5.5 presents the scanning electron micrographs of PDMS/alumina composites for 15, 30 and 50 wt%, respectively. It can be seen that alumina particles are uniformly dispersed throughout the PDMS matrix, validating the effectiveness of the manual

stirring method. As the filler content increases, the agglomeration also increases, as evident in Figure 5.5(k) – (o).

In Figure 5.6 the micrographs of PDMS/PTFE composites with different weight fractions of the micro-PTFE filler are shown. Figures 5.6(a) – (e) indicate that PTFE particles have an average size of < 10 μm. As the filler content increases particle agglomeration appears and air inclusions also arise.

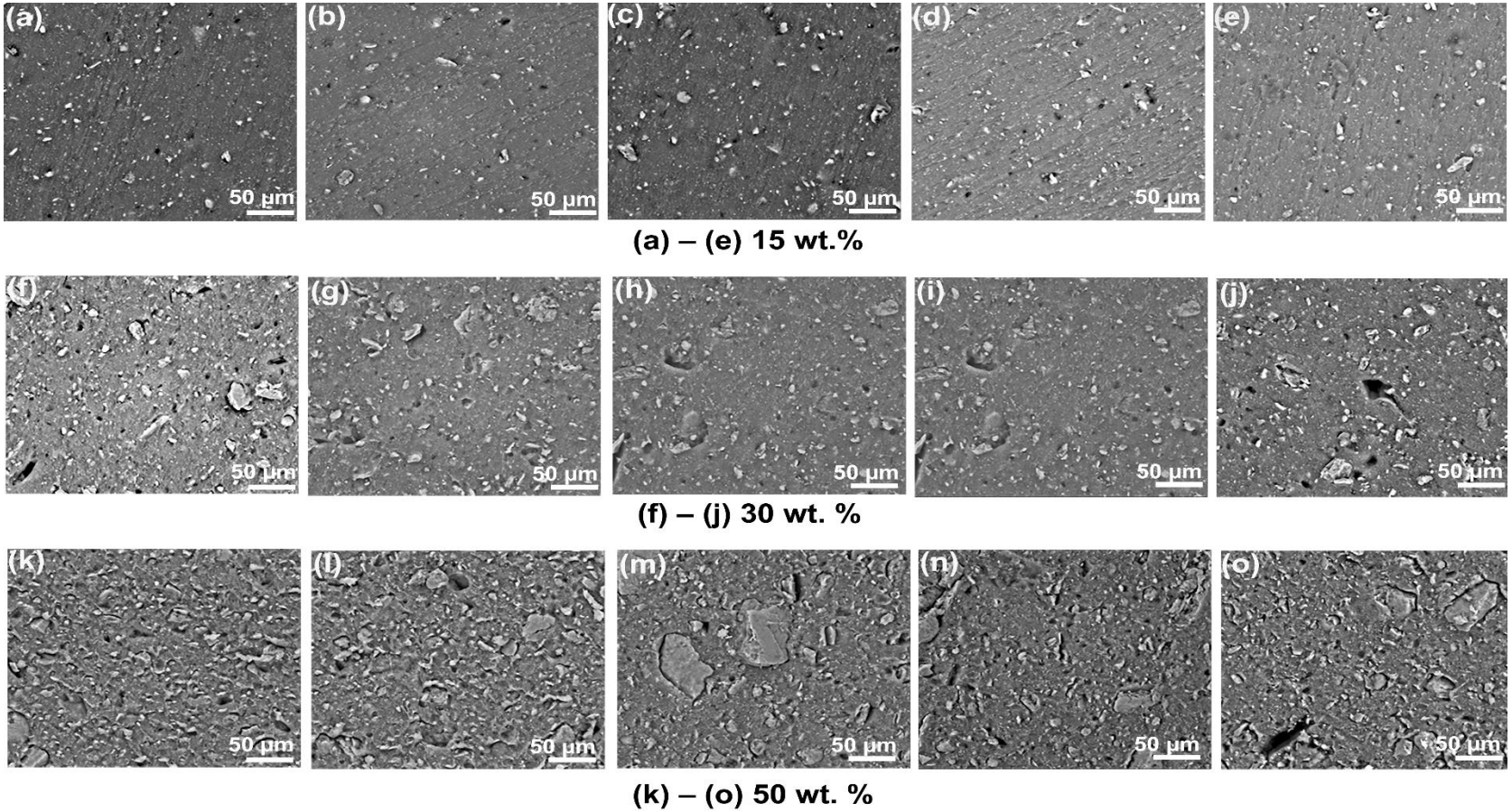

Figure 5.5 : Cross-sectional electron micrographs of PDMS/alumina composites with filler concentrations of: (**a**) – (**e**) 15 wt%, (**f**) – (**j**) 30 wt%, and (**k**) – (**o**) 50 wt%.

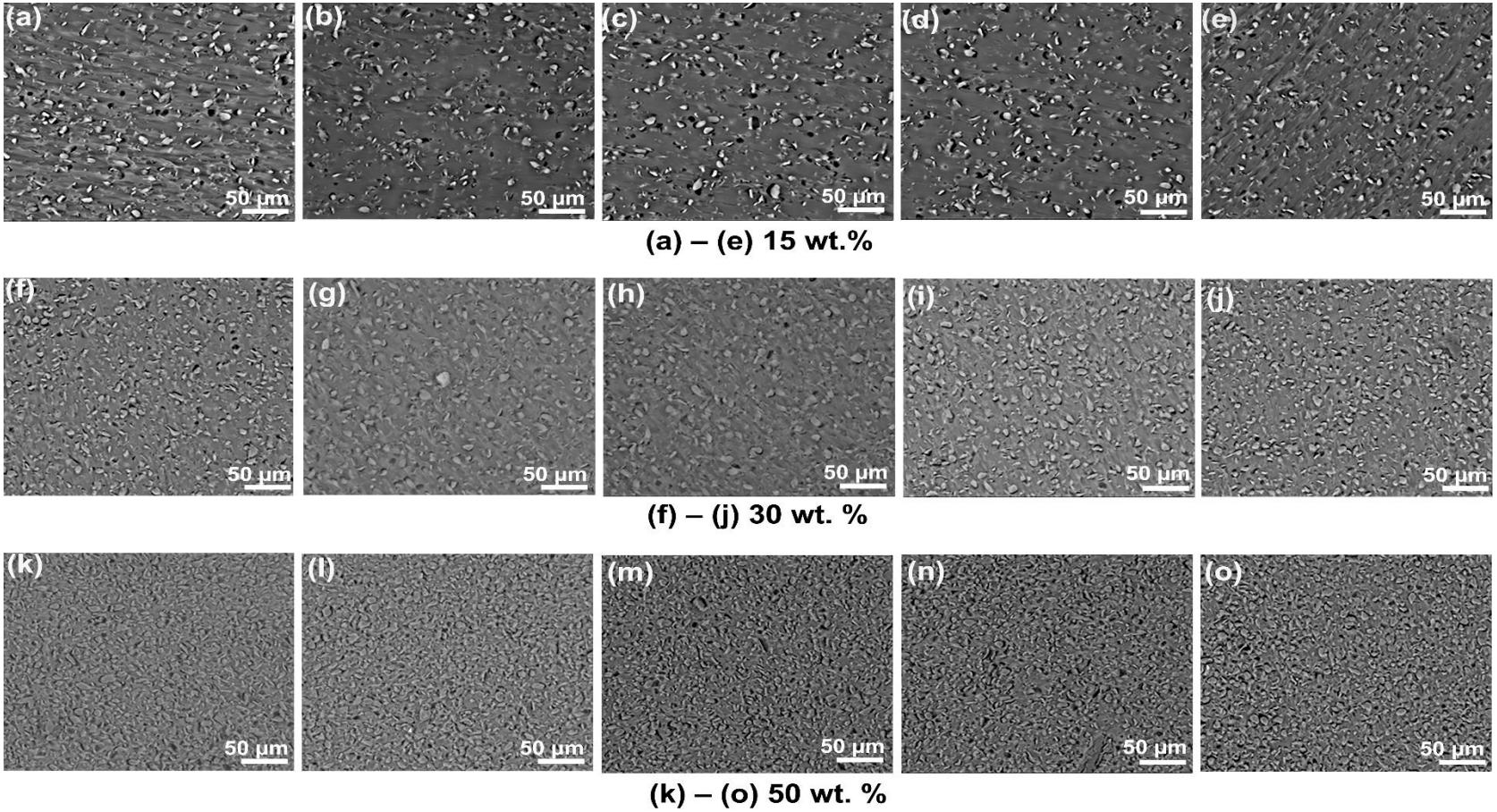

Figure 5.6 : Cross-sectional electron micrographs of PDMS/PTFE composites with filler concentrations of: (**a**) – (**e**) 15 wt%, (**f**) – (**j**) 30 wt%, and (**k**) – (**o**) 50 wt%.

5.4.2 Density and porosity

Figure 5.7 demonstrates the variation in the calculated and measured values of the density for PDMS/alumina and PDMS/PTFE composites verses weight fraction. The uncertainties for the measured density for both composites are around ± 2.5%. The calculated values of the density of composites, ρ_{cal}, are obtained using equation [129]:

$$\rho_{cal} = \rho_f V + \rho_m (1 - V) \tag{5.5}$$

where ρf and ρm are the density of the filler and the matrix, respectively, and V is the volume fraction of the filler.

The values of ρ_{cal} and average measured density (ρ_{mea}) exhibit a similar increasing trend with greater filler loadings, since the density of both alumina (ρ_f = 4 g/cm^3) and PTFE (ρ_f = 2.15 g/cm^3) are higher than that of cured PDMS (ρ_m = 1.03 g/cm^3). However, the ρ_{mea} is smaller than the calculated density at specific weight fractions of the fillers. This is a result of the formation of pores in the composites which is not considered in the calculated values. The porosity, *p*, of composites can be calculated from the measured and calculated density of composites [66]:

$$p = 1 - \frac{\rho_{mea}}{\rho_{cal}} = 1 - \rho_{rel} \tag{5.6}$$

where ρ_{rel} is the relative density of the composites. The porosity of PDMS/alumina composites decreases as filler loading increases indicating the good compatibility and uniform blending between the PDMS matrix and alumina filler as in Figure 5.7(e). However, a contradictory trend is observed for PDMS/PTFE composites which implies the increasing void formation/air inclusion as the PTFE filler loading increases. This

supports the observations of porosity in Figure 5.7(f). A ~7.3 % porosity can be seen for 50 wt% of PTFE filler loading.

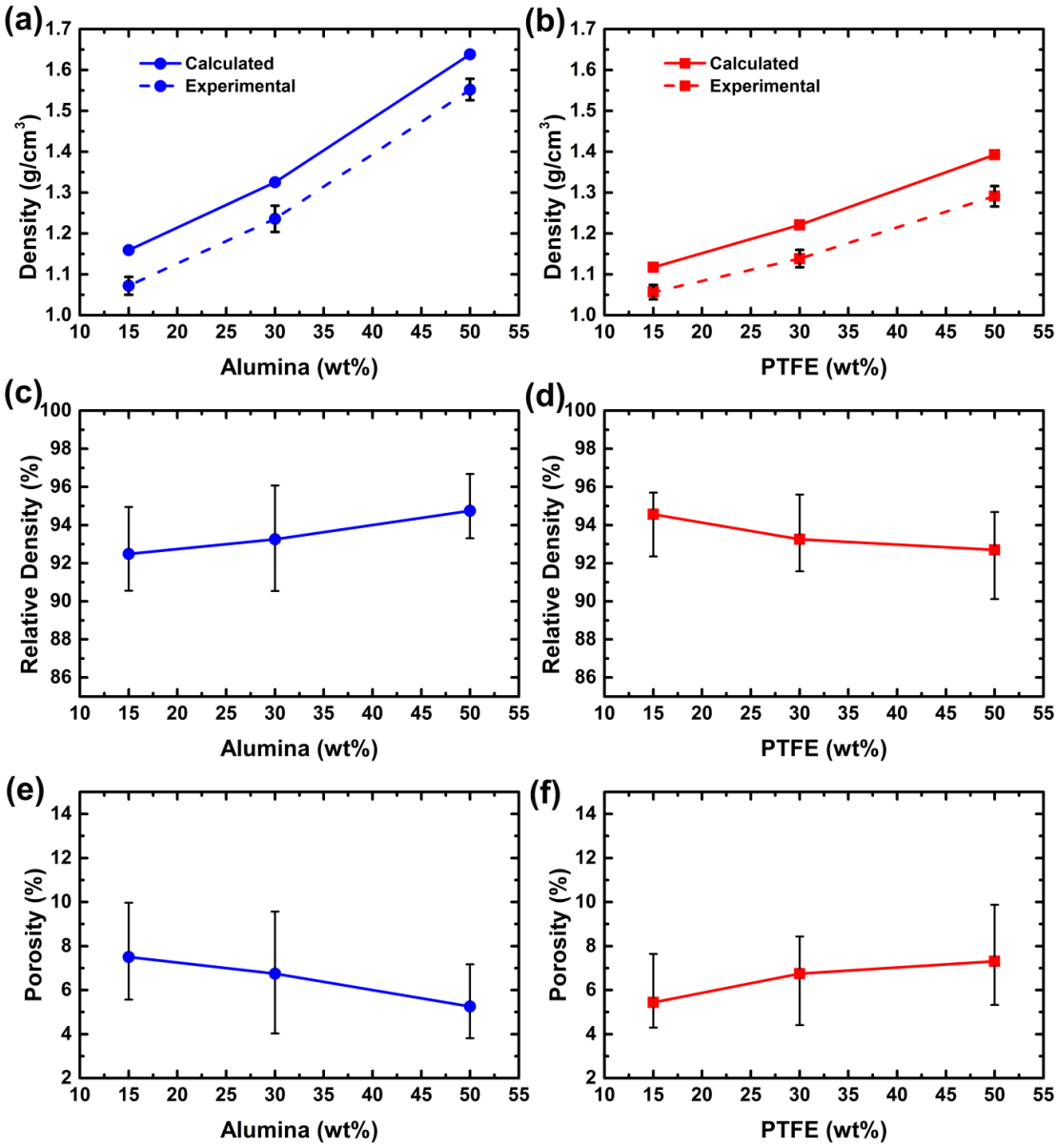

Figure 5.7 : (**a**) and **(b)** Measured and calculated density of composites at different weight fractions of filler. **(c)** and **(d)** Calculated relative density of PDMS/alumina composites and PDMS/PTFE composites, respectively. (**e**) and **(f)** Calculated porosity of PDMS/alumina composites and PDMS/PTFE composites.

5.4.3 Dielectric properties of the composites at microwave frequencies

The variation in relative permittivity and loss tangent of the composites as a function of alumina and PTFE filler loading in the PDMS matrix is shown in Figure 5.8. As ε_r of the alumina filler is higher than the PDMS matrix, the ε_r of PDMS/alumina composites shows an increasing trend with filler loading. A contrasting trend can be seen for the PDMS/PTFE composites due to slightly lower relative permittivity of PTFE compared to the PDMS matrix.

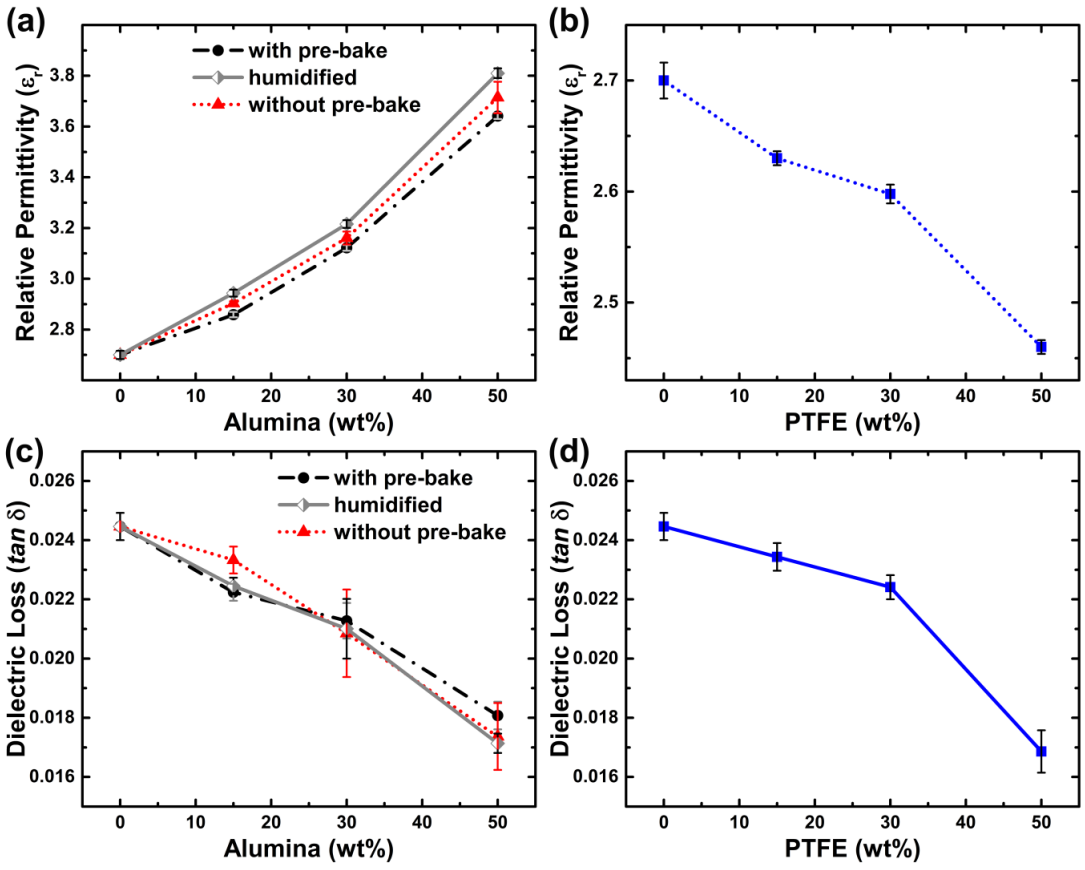

Figure 5.8 : (a) and (b) Variation of relative permittivity of composites with respect to the filler loading at 10 GHz. (c) and (d) Variation of loss tangent of composites with respect to the filler loading at 10 GHz.

The dielectric loss of PDMS/alumina and PDMS/PTFE composites decreases as the filler weight fraction increases is shown in Figure 5.8. The lowest dielectric loss is achieved for 50 wt% PDMS/alumina and 50 wt% PDMS/PTFE composites, showing loss tangents of 0.018 and 0.017, respectively. We hypothesize that this is due to the lower dielectric loss of filler compared to the PDMS matrix at microwave frequencies. The decreasing trend of dielectric loss with the increment fillers loading up to 50 wt% opposes the previous findings for the silicone-rubber/nano-alumina composites as reported by Namitha *et al.*[62] To further investigate and clarify this, two additional experiments were carried out. First, preparation of the PDMS-alumina composites without any pre-bake process; and second, the nano-alumina particles were purposely left in a humid environment for 5 hrs to force the particles to absorb as much water as possible. The composites were then prepared and the dielectric properties measured using the same method as describe in experimental section. In both cases, the measured of dielectric loss exhibits similar reduction trends with the incremental filler loading as the prolonged pre-bake findings, as can be seen in the Figure 5.8(a). Even in the extreme case of deliberately humidifying the filler particles, we have been unable to reproduce the increase in loss reported by Namitha *et al.*, which they attributed to water absorption of the filler. This enhancement indicates that the incorporated PDMS composites are suitable to be implemented as microwave substrate for applications with the requirement for low dielectric loss.

The uncertainty of the resulting relative permittivity and loss tangent using the waveguide resonant cavity approach are calculated at ± 2% and ± 0.06% respectively. These values are congruent with other reported results for this method [64, 130].

Figure 5.8 also highlights that the highest standard deviation of relative permittivity and loss tangent for PDMS/alumina composites without the pre-bake process. Hence, the uncertainty of the water content in the non-prebaked alumina filler has an impact on the characterization accuracy of the dielectric properties.

The following dielectric mixing law models are used to calculate the effective relative permittivity of PDMS-composites at 10 GHz.

Maxwell-Garnett model [66]:

$$\frac{\varepsilon_{eff}-\varepsilon_m}{\varepsilon_{eff}+\varepsilon_m} = V_f \frac{\varepsilon_f-\varepsilon_m}{\varepsilon_f+\varepsilon_m} \quad (5.7)$$

Lichtenecker model [128]:

$$\ln \varepsilon_{eff} = V_f \ln \varepsilon_f + (1 - V_f) \ln \varepsilon_m \quad (5.8)$$

Effective Medium Theory (EMT) model [131]:

$$\varepsilon_{eff} = \varepsilon_m \left[1 + \frac{V_f(\varepsilon_f-\varepsilon_m)}{\varepsilon_m+n(1-V_f)(\varepsilon_f-\varepsilon_m)}\right] \quad (5.9)$$

where ε_{eff}, ε_f and ε_m arerelative permittivity of composite, filler and matrix, respectively V_f is the volume fraction of the filler and *n* is the morphology/shape factor. For the EMT model, the *n* is determined by empirical calculation where lower values signify filler particles of a near-spherical shape.

The predicted values of relative permittivity for PDMS/alumina and PDMS/PTFE composites are compared to the experimental results in Figure 5.9. For PDMS/alumina composites, the EMT model was found to have good agreement with the experimental results at *n* of 0.275. However, for Maxwell-Garnett and Lichtenecker theoretical models match closely with experimental values at lower weight fractions of filler. Beyond 15 wt%, the experimental relative permittivity slightly deviates from the

theoretically predicted models. This can be attributed to the agglomeration of alumina particles at higher filler loading [62].

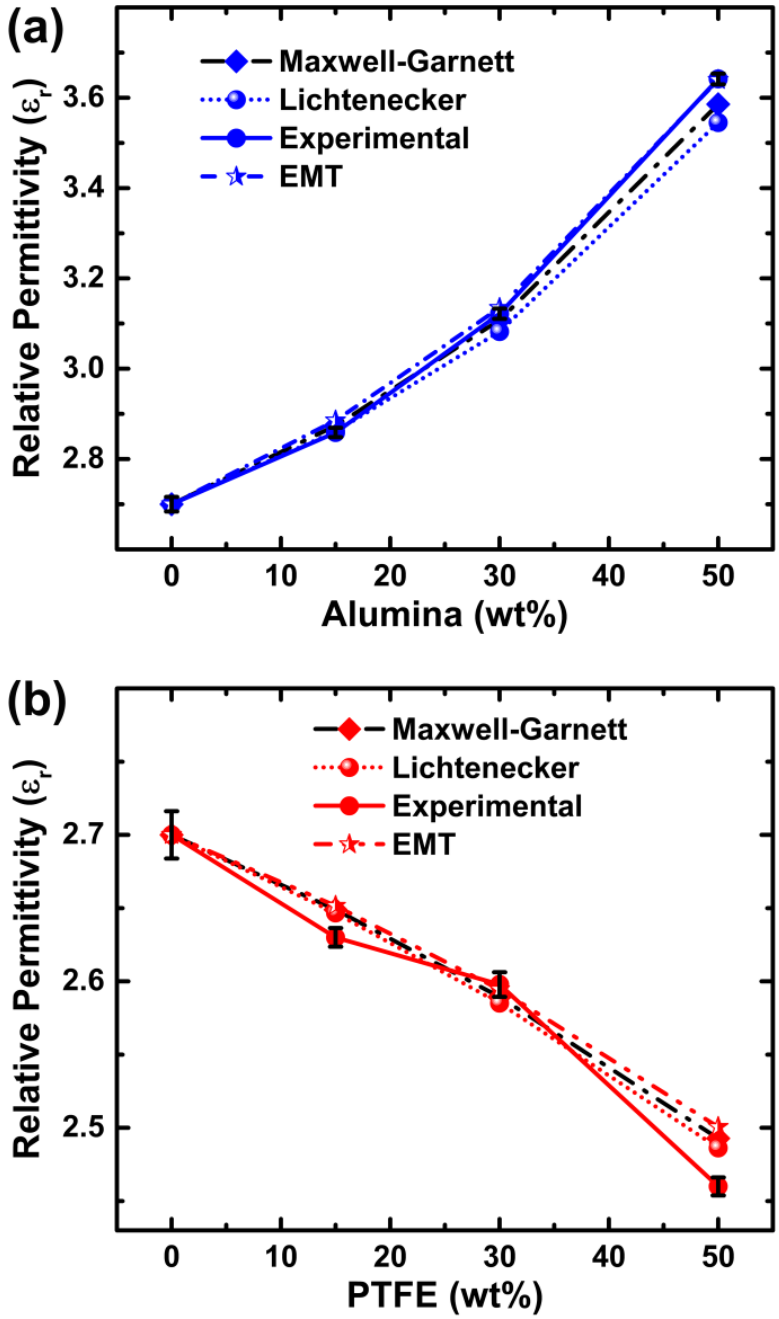

Figure 5.9 : Comparison of experimental and theoretical relative permittivity with respect to the filler loading. (a) PDMS/alumina composites, and (b) PDMS/PTFE composites.

For PDMS/PTFE composites, the experimental values present a small deviation from the predictions by all the theoretical models. This again may be due to the increase in agglomeration as a result of higher filler loading in the PDMS matrix. However, the relative deviation between predicted and experimental values for both composites is < 2%. Both composites exhibit small deviations at higher filler loading, due to agglomeration/air inclusions [131, 132], therefore all the theoretical models used should only be considered as a rough estimator of relative permittivity for higher loadings.

5.4.4 Stress-strain measurement results

The characteristics stress-strain data of Figure 5.10 show that the tensile stress drops significantly with addition of fillers to the PDMS matrix. Increasing the alumina concentrations also decrease the elasticity/flexibility of PDMS/alumina composites as the presence of the alumina particles weaken the filler-matrix mixture interface. In the worst case approximately 100% strain can be applied to 50 wt% of PDMS/alumina composite before it breaks.

In contrast, the PDMS/PTFE composites exhibit an increasing flexibility for 15 wt% and 30 wt% of PTFE concentration as depicted in Figure 5.10. A strain of ~500% can be applied for 15 wt% concentration, exceeding the 350% for pure PDMS. However, as the filler contents increases the agglomerations also increase which may be the reason why less flexibility occurs at the higher filler loading (50 wt%).

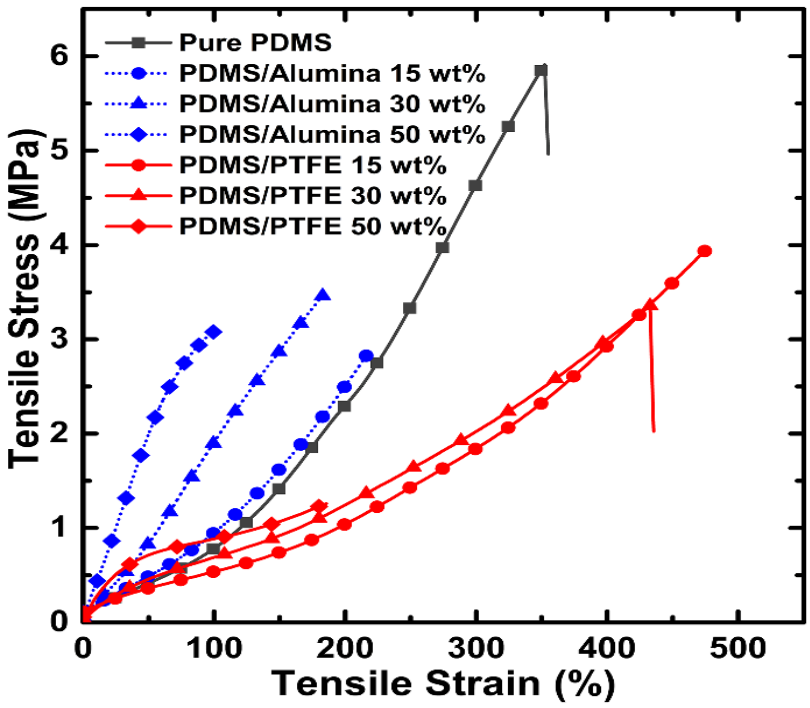

Figure 5.10 : Stress-strain relationship of PDMS composites.

5.4.5 Moisture absorption

Moisture absorption is a major concern in microwave circuit applications since water will degrade the dielectric properties of composites substrate material, and may cause damage to metallic tracks and other circuitry. Figure 5.11 indicates that as the filler loading increases, moisture absorption also increases. The highest deviation of moisture absorption is measured at higher filler loadings, with only ± 0.1% variation. At 50 wt% filler loading, PDMS/alumina composite and PDMS/PTFE composite have a moisture absorption of 0.20% and 0.45%, respectively. For the PDMS/alumina composites, the slightly increased moisture absorption is due to agglomeration and hydrophilic nature of ceramic fillers. However, for the PDMS/PTFE composites which exhibit superhydrophobic behavior [133], the increasing trend of moisture absorption with respect to filler loading concentrations, is likely due to increase of porosity/air inclusions in the microstructure which has been identified by examining the composite

density in Figure 5.7 (f).

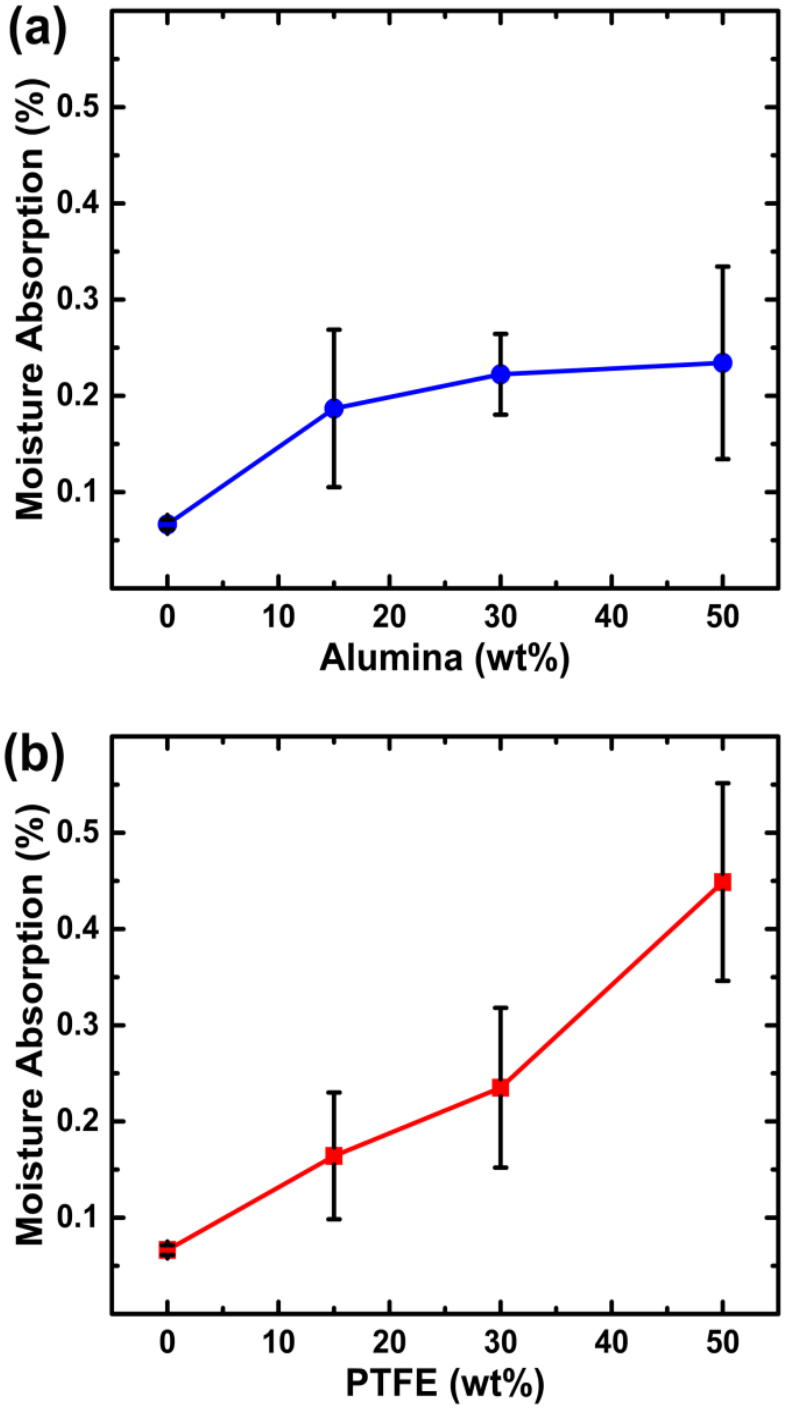

Figure 5.11 : Moisture absorption of the composites with respect to the filler loading. (a) PDMS/alumina composites, and (b) PDMS/PTFE composites.

5.4.6 Swelling measurements

Equilibrium swelling measurements of the composite were investigated and compared to a pristine PDMS reference to evaluate any changes in cross-linking density [134]. The solvent uptake, or mass swelling degree (MSD), is presented in Figure 5.12. The MSD of pristine PDMS published in previous studies are in agreement with the obtained result [135, 136].

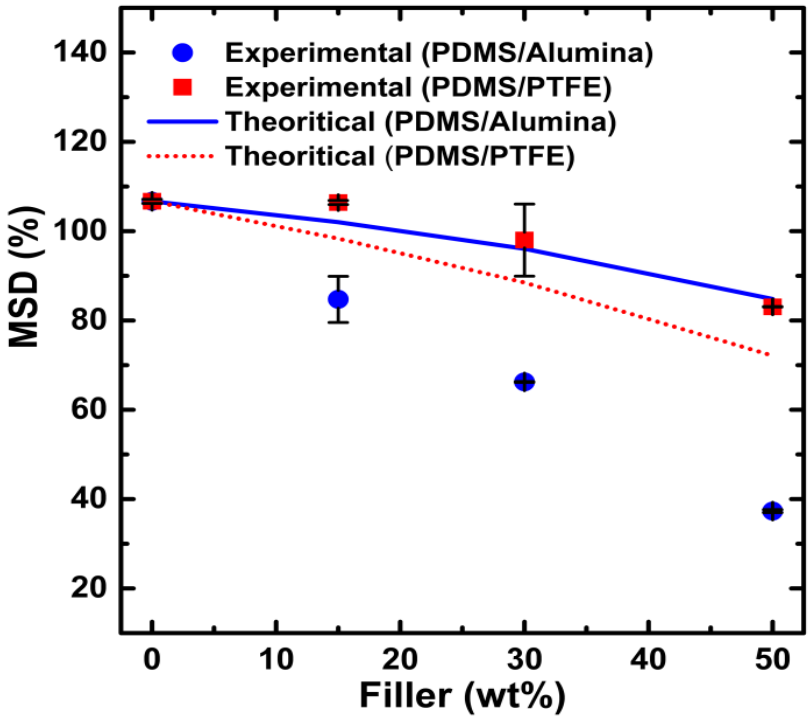

Figure 5.12 : Cross-linking study of the PDMS/alumina and PDMS/PTFE composites at different weight fractions of filler based on mass swelling degree (MSD).

Figure 5.12 shows the MSD decreases with the increase of alumina or PTFE filler loadings. It also reveals a steep decrease in the MSD for PDMS/alumina composites compared to PDMS/PTFE composites at the same weight fraction loading. At a filler loading of 50 wt%, a decrease in MSD of approximately 65% and 22% are observed for PDMS/alumina and PDMS/PTFE composites, respectively.

The reduction of MSD implies an increasing cross linking density which is associated with a decreasing chain length between the cross-links within the polymer [137].

The MSD of PDMS/alumina composites in Figure 5.12 shows a large difference/reduction with respect to what the theoretical calculation of MSD would be if the crosslinking density of the PDMS remained constant. The substantial reduction of MSD was associated with higher cross linking density, producing shorter chain length and therefore a tighter polymeric matrix. This also causes a reduction in the elasticity/flexibility of PDMS/alumina composites, as confirmed through the stress-strain measurements seen in Figure 5.9.

The PDMS/PTFE composites show a contrasting result for MSD implying a reduction in crosslinking density of the base PDMS. The measured MSD is slightly higher than the theoretical MSD which can be ascribed to a reduction in crosslinking density, creating a looser polymeric matrix. Consequently, the PDMS/PTFE composites (15 wt% and 30 wt%) are more flexible than pure PDMS as verified by the tensile strain of Figure 5.10. However, the lower flexibility the 50 wt% of PDMS/PTFE composite can be attributed to particle agglomeration as confirmed in SEM image of Figure 5.6(k)-(o).

5.5 BROADBAND FREQUENCY INVESTIGATION OF DIELECTRIC PROPERTIES

The limitation of the waveguide resonant cavity technique used in the previous sections is this method only can measure the dielectric properties at one specific frequency. Therefore, a rectangular waveguide transmission/reflection technique is also employed to study the dielectric properties of the PDMS composites over a broadband frequency reance, in this case at X-band (8 to 12 GHz). Although the accuracy is not as good as

the resonant cavity method for very low loss materials, the results can be used as validation and can provide general information on how the dielectric properties change verses frequency.

5.5.1 Sample preparation

The sample preparation process is similar as described in Section 5.2, however different size samples of 2.286 cm × 1.016 cm × 0.600 cm were formed using a mould from the sections of X-band waveguide as shown in Figure 5.13. The dimensions enable the cured PDMS composite to be inserted snugly into a standard WR-90 rectangular waveguide. The PDMS composites mixtures in the mould were degassed in a vacuum oven for ~3 h to remove air bubbles. Subsequently, the fully degassed samples were slowly pressed into the mould and left to dry at room temperature for ~24 h. For this measurement method, samples with filler concentrations of 15 wt%, 30 wt%, and 50 wt% for both PDMS/alumina and PDMS/PTFE composites were prepared.

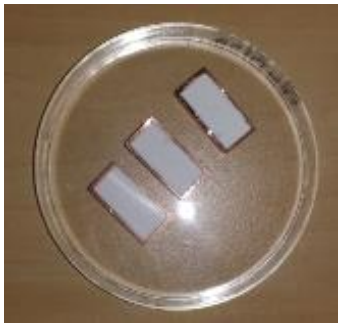

Figure 5.13 : The PDMS composite samples in mould.

5.5.2 Measurement procedure:

An X-band waveguide calibration process was completed before the cured PDMS composite was inserted and transmission/reflection measurements taken. The calibration process and the measurement set-up are presented in Figure 5.14(a). The figure illustrates the overall process required to carry out a full 12-term thru–line–reflect (TRL) calibration on a vector network analyser (VNA). The ‘thru’ measurement is carried out by keeping a straight transmission measurement between the waveguides. Subsequently, a length of ‘line’ which is exactly a guided quarter wavelength at the mid-band frequency of the waveguides is inserted on the sample holder in between the waveguides. Finally, the waveguide is shorted by placing a metal plate on the sample holder in between the waveguides and the ‘reflect’ measurement is taken. Once the calibration is completed, the sample can be measured by placing it in the flange holder (Figure 5.14(d)).

The dielectric properties of the PDMS composites were calculated using the Nicholson–Ross–Weir (NRW) complex dielectric formulas [138, 139]. The details of this process are discussed in Appendix B. Validation of measurement system was carried out by measuring the complex permittivity of a Rogers RT/duroid 5880 substrate inserted in the waveguide, which also appears in Appendix B.

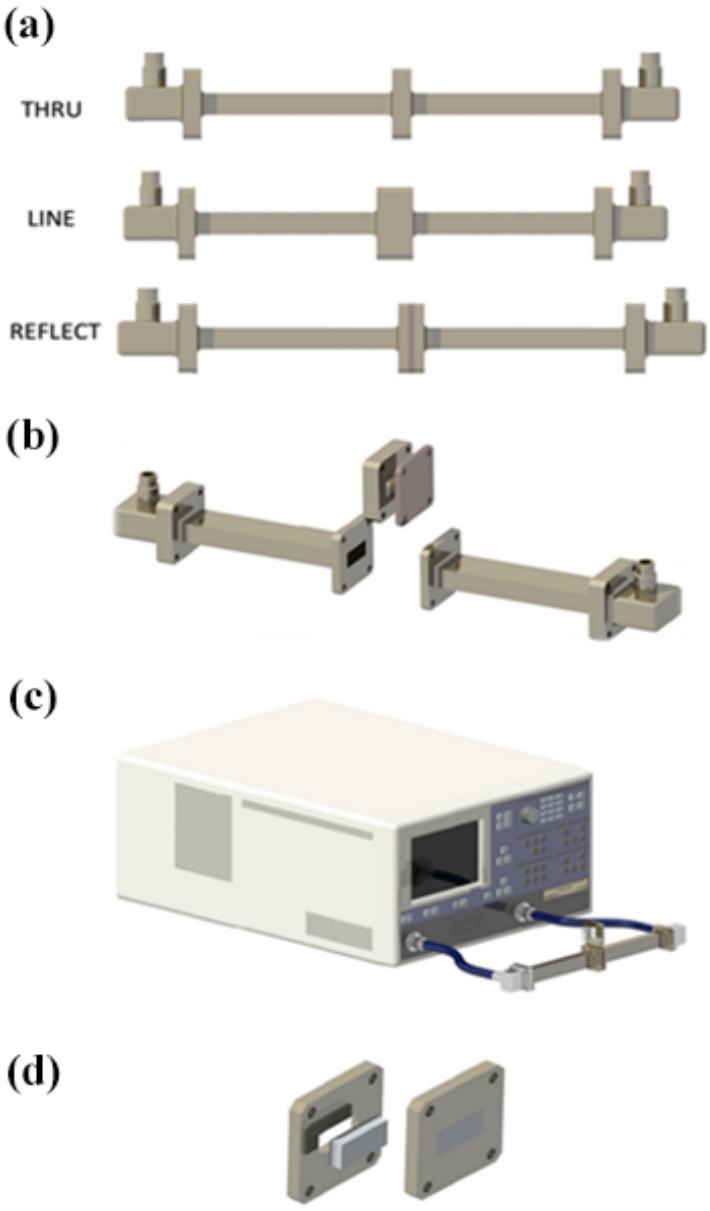

Figure 5.14 : Calibration and measurement setup of waveguide transmission/reflection method: (a) calibration steps, (b) setup detail, (c) VNA connection, and (d) sample and holder.

5.5.3 Results and discussion:

Figure 5.15 shows the measured relative permittivity of pristine PDMS, PDMS/Alumina and PDMS/PTFE composites over X-band frequencies. A comparison of the measured relative permittivity at 10 GHz with the mixing model predictions and the previous resonant cavity method measurements are summarized in Table 5.1. Very good agreement is observed between the measured ε_r using waveguide transmission/reflection method and the resonant cavity method. They also show good congruence with the calculations for all mixing laws models. Only one slightly abnormal value resulted for PDMS with 30 %wt of alumina composite, with a maximum 6.8% difference seen. However, this anomalous result appears to be a trait of the fluctuation in permittivity measured for higher percentage PDMS/Alumina samples, which can occur in broadband measurement methods. Hence, these results verify the resonant cavity method results presented earlier in the chapter as accurate dielectric permittivity characterizations of PDMS composites. They also imply the expectation that the permittivity of the composites does not vary rapidly with frequency is valid.

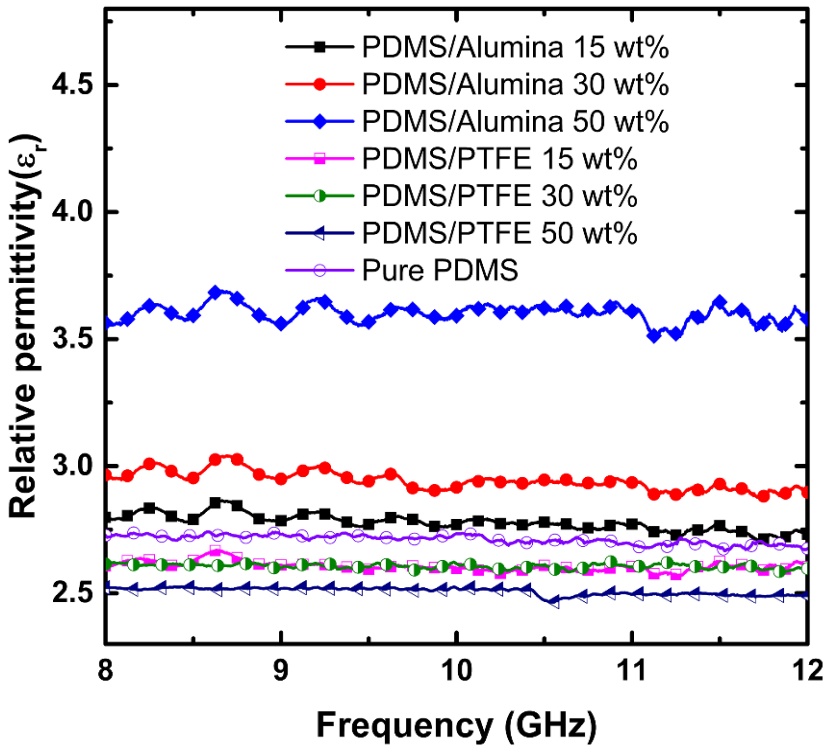

Figure 5.15 : Measured ε_r at X-band for PDMS and PDMS composites

Table 5.1 : Measurement and Calculation of ε_r at 10 GHz

Samples	**Measurement Results**		**Mixing Law Calculation of ε_r**		
	Waveguide	**Resonant**	**Maxwell**	**Lichtenecker**	**EMT**
PDMS	2.72	2.70	-	-	-
PDMS/Alumina 15 wt.%	2.77	2.86	2.87	2.86	2.89
PDMS/Alumina 30 wt.%	2.92	3.12	3.11	3.08	3.13
PDMS/Alumina 50 wt.%	3.59	3.64	3.57	3.54	3.64
PDMS/ PTFE 15 wt.%	2.67	2.63	2.65	2.65	2.64
PDMS/ PTFE 30 wt.%	2.62	2.60	2.59	2.59	2.57
PDMS/PTFE 50 wt.%	2.52	2.46	2.49	2.49	2.47

Figure 5.16 shows the measured loss tangent of pristine PDMS, PDMS/Alumina and PDMS/PTFE composites at X-band frequencies. The results highlight the severe variability due to the limited accuracy of this method for low loss characterisation, which leads to inconclusive analysis of the samples. The limitations of the waveguide transmission/reflection method in characterising loss amount from the factors:

- The test sample must be machined/fabricated so as to fit in the waveguide cross section with negligible air gaps.
- Thickness uniformity is also difficult to achieve in practice and the NRW extraction is highly dependent on accurate knowledge of sample thickness.
- The composites mixtures are inhomogeneous due to variations in the moulding process.
- The presence of uncontrolled bubbling during curing process due to the thicker sample blocks is also noticeable.

These reasons are the major contributors to the large changes/fluctuations in the measurement results of loss tangent as presented in Figure 5.16.

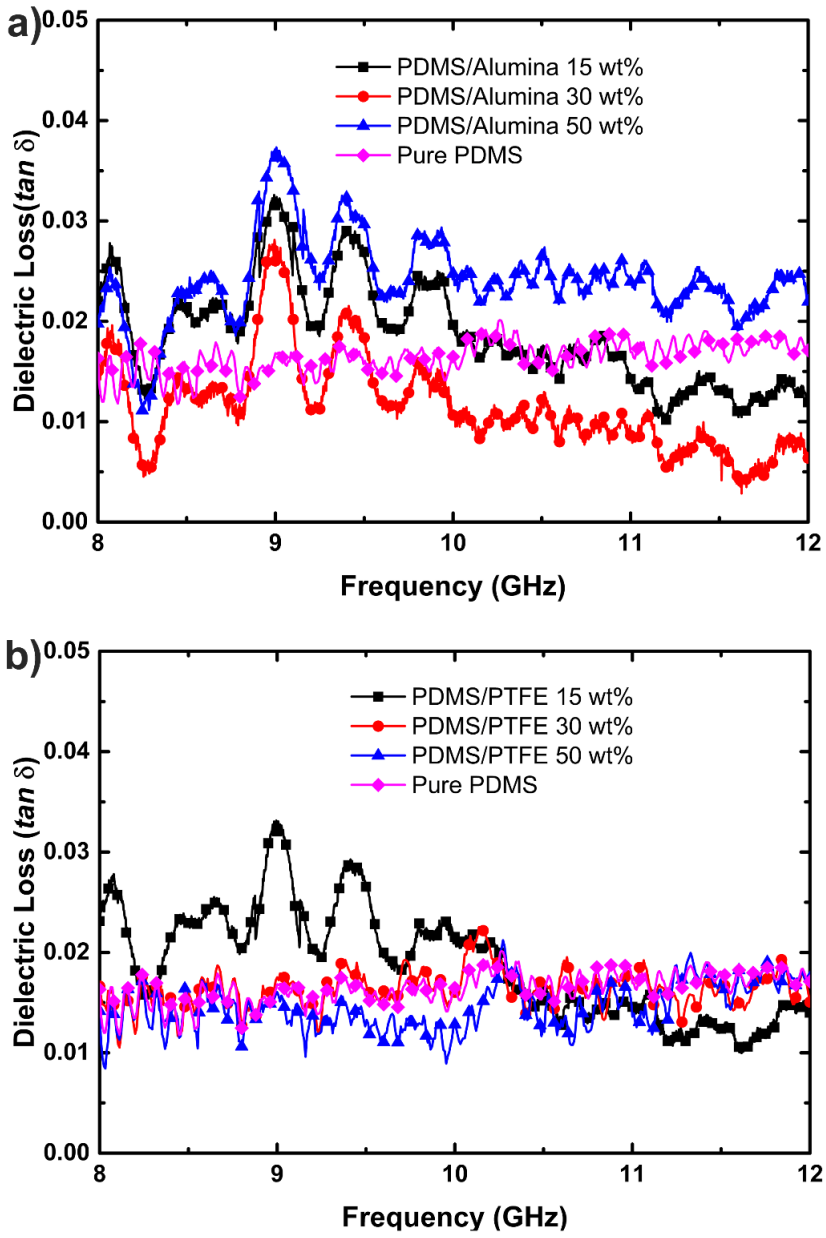

Figure 5.16 : Measured loss tangent at X-band of (a) PDMS/alumina composites, and (b) PDMS/PTFE composites.

5.6 SUMMARY AND OUTLOOK

In this chapter, the properties of PDMS/alumina and PDMS/PTFE composites have been examined in terms of their structural, dielectric and mechanical properties. Scanning electron micrographs reveal an occurrence of agglomeration and air inclusions with increasing of filler loadings for both composites, in particular the

PDMS/PTFE composites. The density was measured and the porosity calculated as confirmation. The experimental relative permittivity of both composites exhibits control over the dielectric properties, and is in good agreement with the predicted theoretical models. Increases/decreases in relative permittivity corresponded to the addition of more alumina/PTFE into the PDMS as hypothesized. Dielectric loss tangent was also shown to decrease with filler loading. At 50 wt% filler loading, the loss tangent was 0.018 and 0.017 for PDMS/alumina and PDMS/PTFE composites, respectively. The PDMS/PTFE composites exhibited higher flexibility/elasticity compared to PDMS/alumina composite as supported by mass swelling degree results. However, both composites had an increasing trend of moisture absorption with respect to the filler loading.

To further validate the dielectric property measurements, the investigation of the PDMS composites over a broad frequency range was carried out using a waveguide transmission/reflection method with NRW extraction. The relative permittivity results are congruent with the theoretical models and resonant cavity characterisation. However, the loss tangent shows inconsistence with large fluctuations over the broadband frequency range, generating inconclusive results. This highlights the limitation of this method for loss characterisation and validates the choice of the resonant cavity method for the analysis of PDMS composites, and also indicates that their permittivity will not vary rapidly with frequency. The studies in this chapter show that PDMS/alumina and PDMS/PTFE composites can offer a viable solution for flexible microwave substrate applications.

CHAPTER 6

CONCLUSION AND FUTURE WORKS

6.1 CONCLUDING REMARKS

The vision for this thesis involved developing EM resonators utilising elastomeric substrates and liquid metal, with the potential to make them tunable and control/modify their electromagnetic characteristics. The implementation of flexible PDMS substrates and liquid metal Galinstan to realise meta-atom SRR evolved into the key conceptual theme. The ability of Galinstan to conform to any shape inside the PDMS microfluidic channels whilst the structure remained mechanically stable was exploited to demonstrate mechanically tolerance, tuning via air pressure, and fully integrated microfluidic dielectric sensing. The study also extends to producing PDMS micro/nanocomposites by mixing the polymer with either alumina or PTFE particles to reduce the dielectric loss (*tan* δ).

During the course of this research, the available literature on SRRs and their applications, metamaterial and microfluidic concepts, tuning and sensing techniques, and flexible micro-nanocomposites substrates at microwave frequencies have been studied. The review on these topics is presented in Chapter 2 of this thesis.

A detailed summary of the results and outlook is presented at the end of each of the respective chapters. This chapter provides a brief summary of the research outcomes obtained in this thesis. These outcomes highlight that there is scope for further investigation of flexible EM components for tuning and sensing applications. The scope of such future work will also be discussed.

6.1.1 Mechanically tolerant SRR

A meta-atom fluidic SRR that has capability to withstand mechanical strain whilst maintaining electrical performance has been developed. An SRR with a wider than standard gap is shown to be more tolerant to mechanical deformation than a more conventional sized gap. This behaviour was confirmed through simulation using CST Microwave Studio software. Such an SRR made from encapsulated liquid metal Galinstan in PDMS elastomeric substrate layers was subjected to bending, repeatable stretching and twisting. Under this severe mechanical deformation, the SRR exhibited no significant degradation of the transmission coefficient response. This work meets Objective 1 of Section 1.2.

6.1.2 SRRs for tunability and sensing

The meta-atom fluidic SRR with a confined microfluidic channel in between its gaps is implemented for tuning and sensing applications. The gaps of SRR are very sensitive to any physical/electric field changes. Tuning is demonstrated via air pressure/vacuum in the microfluidic channel which results in expansion/deflation of the gaps, thus creating a frequency shift. Transforming the microfluidic channel to dual inlets/outlets makes the SRR capable of delivering a liquid sample into the sensitive gap area.

Exploiting this feature, a microfluidic SRR sensor for dielectric property characterization was demonstrated. This work meets Objective 2 and 3 of Section 1.2.

6.1.3 PDMS composites for microwave applications

A method for reducing dielectric loss of flexible substrates by forming PDMS composites loaded with various concentrations of either Alumina or PTFE particles has been demonstrated. The PDMS composites were fully characterized to reveal their structural, mechanical and dielectric properties. Good congruence between the measured results and theoretical mixing models was achieved. The incorporation of either low dielectric loss filler in the PDMS matrix (up to 50 wt% filler loading) is shown to reduce the dielectric loss while maintaining flexibility in the host matrix. The fillers can also control the permittivity of the composite, either increasing or decreasing relative permittivity from that of PDMS. This work meets Objective 4 of Section 1.2.

6.2 RECOMMENDATIONS FOR FUTURE WORK

Significant progress has been made in the development of electromagnetic structures on flexible PDMS substrates using liquid metal Galinstan in this research, as well as investigations into producing low-loss PDMS composites. However, numerous opportunities for continuing research in alignment with those presented in this thesis still exist. A list of potential future work is as follows:

- As a meta-atom SRR, the mechanical tolerant SRR structure can be used in a host of applications such as filters, switches and all kinds of devices where an insensitive response to strain and changing conditions is required.

- The mechanically tolerant SRR, pneumatically tunable SRR and microfluidic SRR sensor can extend to an array of SRR elements to enhance the resonant response.
- There are several future research possibilities for the proposed tunable SRR. The tuning range can be improved by modifying the side walls of the microfluidic channel in between the SRR gaps, or by applying a multilayer resonator structure. To realize this, increased complexity in the design and fabrication process are expected.
- Extend the functionality of the fully integrated microfluidic sensor to other potential applications not limited to dielectric characterization. For example, in biomedical/lab-on-a-chip applications to detect or measure glucose concentrations for diabetes diagnosis.
- The low-loss dielectric and excellent mechanical properties of the PDMS-Alumina and PDMS-PTFE composites opens up a new paradigm to exploit these alternative flexible materials. Further investigations into the increased flexibility of the PDMS-PTFE composites compared to neat PDMS (or potentially other polymer/polymer composites) could lead to new ultra-flexible materials.

In general, several specific potential areas are identified for future research as listed below:

- Wireless sensing and lab-on-chip applications
- On-body EM device implementation (could be wound or woven into devices/ electronic fabric)
- Micro/nanocomposites EM devices
- Micro/nanocomposites flexible microwave substrates.

APPENDIX A

SENSOR CHARACTERISTICS USING WATER–METHANOL MIXTURES

To further validate and characterize the complex permittivity of the DI water-methanol samples, a set of calibration experiments has been performed using similar binary mixtures of DI water-methanol. The dielectric properties water-methanol mixtures studied in [125] are used as reference. Figure A1 depicts the complex permittivity of the water–methanol mixtures at 3 GHz obtained by curve fitting to the literature values in [125]. Dispersion is not taken into account, since the resonance shift is within a narrow frequency band.

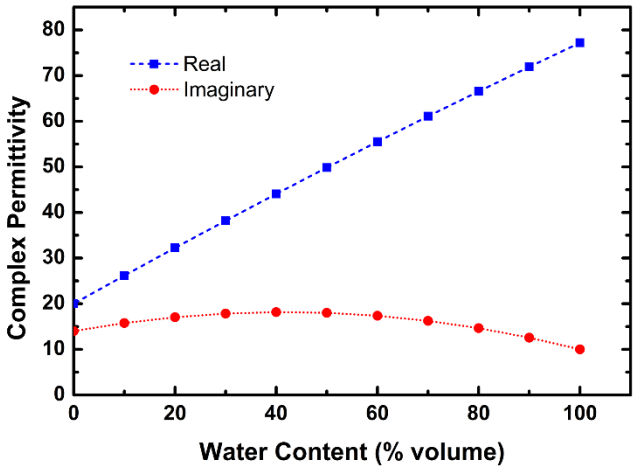

Figure A1**:** Complex permittivity of water–methanol mixture. The mixture permittivity at 3 GHz is shown as a function of the water content. The values are taken from [125] with polynomial fitting to smooth the curves within the confidence interval.

In similar manner [107, 108], the simplified model that relates changes in the complex permittivity to variations in the resonance frequency and peak attenuation can be expressed in the matrix form as:

$$\begin{bmatrix} \Delta f_0 \\ \Delta|S_{21}| \end{bmatrix} = \begin{bmatrix} m_{11} & m_{12} \\ m_{21} & m_{22} \end{bmatrix} \begin{bmatrix} \Delta\varepsilon'_{sam} \\ \Delta\varepsilon''_{sam} \end{bmatrix} \quad \text{(A1)}$$

where $\Delta\varepsilon'_{sam} = \varepsilon'_{sam} - \varepsilon'_{ref}$, $\Delta\varepsilon''_{sam} = \varepsilon''_{sam} - \varepsilon''_{ref}$, $\Delta f_{Osam} = f_{Osam} - f_{Oref}$, and $\Delta|S_{21}| = |S_{21}|_{sam} - |S_{21}|_{ref}$, with the subscript 'sam' for the sample and 'ref' for the reference mixture. Here, the mixture with a 50% water fraction is considered as the reference. The complex permittivity values of the test fluid samples extracted from Figure A1 are summarized in Table A1.

Table A1:

Complex permittivity of the water–methanol mixture at 3 GHz [125]. The volume fraction of water is changed from 10% to 90% for device testing.

Water Fraction %	ε'	ε''	Δε'	Δε''
10	26.2	15.8	-23.7	-2.2
30	38.2	17.8	-11.6	-0.2
50	49.8	18.0	0.0	0.0
70	61.1	16.2	11.2	-1.8
90	71.9	12.6	22.1	-5.4

For the first set of measurements, the volume fraction of water is changed from 10% to 90% with a step size of 20% and at each step, the resonance frequency and peak attenuation of the sensor are recorded giving a data set of 5 samples. The measurement results of the resonance frequency and maximum attenuation for the 5 test samples are shown in Figure A2. The resonance frequency is shifted from 3.017 GHz down to 2.998 GHz as the water volume fraction increases from 10% to 90%. The peak attenuation will be minimum for pure methanol, or when the water volume fraction is 0%.

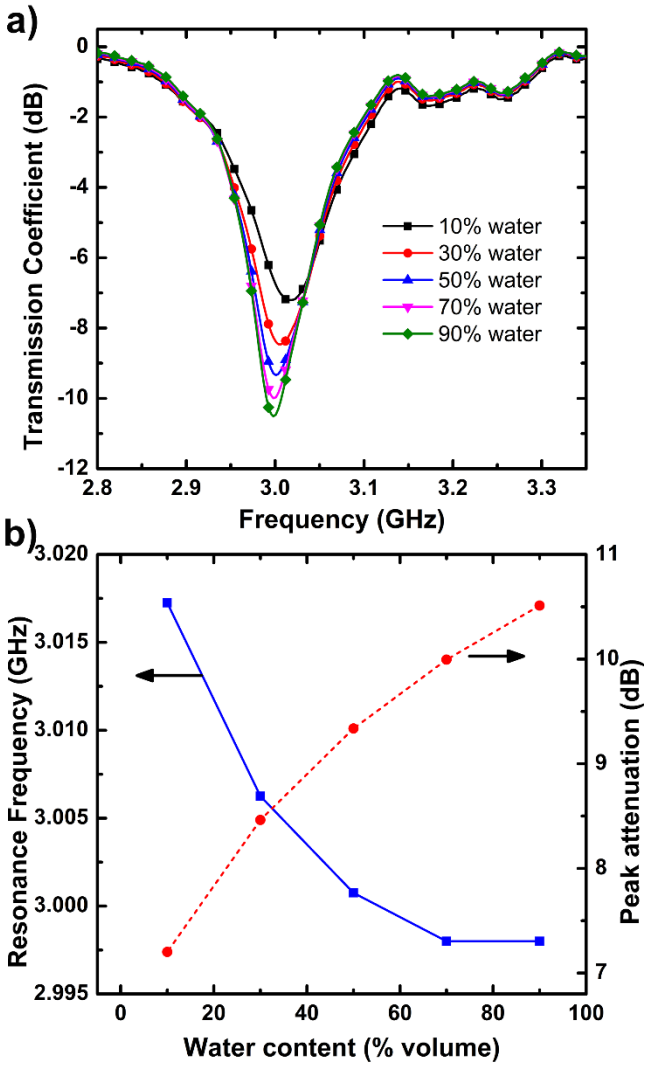

Figure A2: The measured transmission response of the water–methanol test samples for calibration of the sensor. The water volume fraction is changed from 10% to 90% with the step size of 20%. (b) Corresponding resonance frequency and peak attenuation at different steps.

The unknown coefficients of the model in equation (A1) are over determined by test datasets. The least-squares method explained in Ref. [107] can be used to approximate the unknown coefficients. The benefit of this model is that all the fabrication tolerances of the device are fully taken into account. Three matrices are set up from the reported complex permittivity in Table A1 [125], measured resonance frequency, and measured S_{21}, as:

$$X = \begin{bmatrix} \Delta\varepsilon'_{sam1} & \Delta\varepsilon''_{sam1} \\ \Delta\varepsilon'_{sam2} & \Delta\varepsilon''_{sam2} \\ \vdots & \vdots \\ \Delta\varepsilon'_{sam5} & \Delta\varepsilon''_{sam5} \end{bmatrix}, Y_1 = \begin{bmatrix} \Delta f_1 \\ \Delta f_2 \\ \vdots \\ \Delta f_5 \end{bmatrix} \; and \; Y_2 = \begin{bmatrix} \Delta|S_{21}|_{sam1} \\ \Delta|S_{21}|_{sam2} \\ \vdots \\ \Delta|S_{21}|_{sam5} \end{bmatrix} \tag{A2}$$

The unknown coefficients can be calculated from:

$$[m_{11} \quad m_{12}]^T = (X^T X)^{-1} X^T Y_1 \tag{A3}$$

$$[m_{21} \quad m_{22}]^T = (X^T X)^{-1} X^T Y_2 \tag{A4}$$

These equations yield the characteristic matrix that relates the complex permittivity of the liquid under test with the resonance properties as:

$$\begin{bmatrix} \Delta f_0 \\ \Delta|S_{21}| \end{bmatrix} = \begin{bmatrix} -0.0005 & 0.0017 \\ -0.0496 & -0.4421 \end{bmatrix} \begin{bmatrix} \Delta\varepsilon'_{sam} \\ \Delta\varepsilon''_{sam} \end{bmatrix} \tag{A5}$$

The sensor module can be exclusively described by this set of equations, which fully takes into account deviations in the dimensions and properties of constructing materials. Through the matrix inversion, equation (A5) yields:

$$\begin{bmatrix} \Delta\varepsilon'_{sam} \\ \Delta\varepsilon''_{sam} \end{bmatrix} = \begin{bmatrix} -3233.3897 & 12.4333 \\ 362.7687 & -3.6568 \end{bmatrix} \begin{bmatrix} \Delta f_0 \\ \Delta|S_{21}| \end{bmatrix} \tag{A6}$$

This empirical model can be used to determine the complex permittivity of unknown liquid samples just simply measuring the resonance characteristics.

APPENDIX B

NICHOLSON-ROSS-WEIR (NRW) COMPLEX DIELECTRIC CALCULATION

The complex permittivity, ε, and permeability, μ, of material-under-test (MUT) using Nicholson-Ross-Weir (NRW) waveguide method [138] can be summarized as in flowchart of Figure B1.

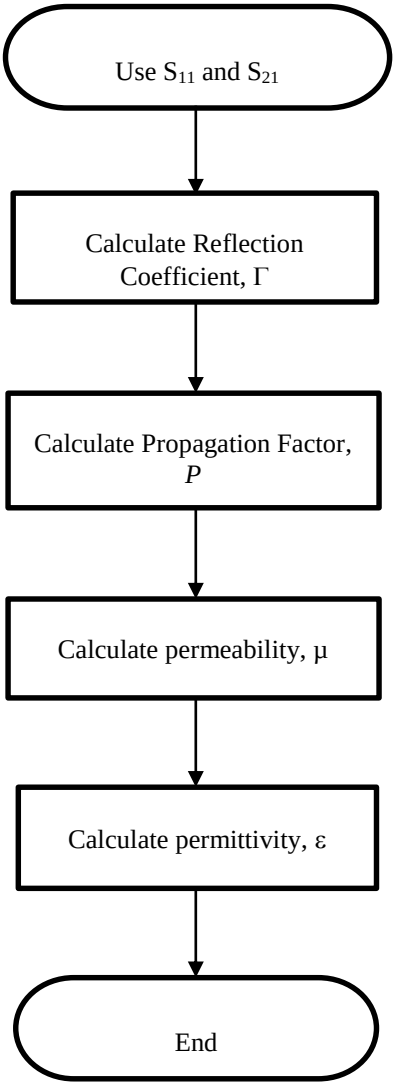

Figure B1: The process for the NRW method

The transmission (S_{21}) and reflected (S_{11}) Scattering parameters for the MUT can be obtained directly from the vector network analyser. The reflection coefficient, Γ can be defined as:

$$\Gamma = X \pm \sqrt{X^2 - 1} \tag{B1}$$

Where,

$$X = \frac{S_{11}^2 - S_{21}^2 + 1}{2S_{11}} \tag{B2}$$

The propagation factor is given by:

$$P = \frac{S_{11} + S_{21} - \Gamma}{1 - (S_{11} + S_{21})\Gamma} \tag{B3}$$

Finally, the permittivity and permeability can be calculated:

$$\mu_r = \frac{1 + \Gamma}{\Lambda(1 - \Gamma)\sqrt{\frac{1}{\lambda_0^2} - \frac{1}{\lambda_c^2}}} \tag{B4}$$

$$\varepsilon_r = \frac{\lambda_0^2}{\mu_r}\left(\frac{1}{\lambda_c^2} - \left[\frac{1}{2\pi L}\ln\left(\frac{1}{P}\right)\right]^2\right) \tag{B5}$$

where, L is sample length, λ_0 is free space wavelength, λ_c is waveguide cut-off frequency and

$$\frac{1}{\Lambda^2} = -\left(\frac{1}{2\pi L}\ln\left(\frac{1}{P}\right)\right)^2 \tag{B6}$$

Note: Due to the complex nature of the propagation factor, the number of roots for a complex natural log is infinite (i.e., j+2πn). Therefore, a branching index n needs to be defined in order to correct the function (see [138, 140] for further details).

The loss tangent can be then calculated by:

$$\tan\delta = \frac{\varepsilon''}{\varepsilon'} \tag{B7}$$

where ε' is the magnitude of the real part, and ε" is the magnitude of the imaginary part.

To validate the extracted complex permittivity using the NRW method, a Rogers RT/duroid 5880 substrate was used and the complex permittivity has been calculated as presented in Figure B2. The mid-band relative permittivity was extracted to be $\varepsilon_r = 2.24$. The extracted relative permittivity is in accordance with the Rogers RT/duroid 5880 datasheet (*https://www.rogerscorp.com/documents/606/acm/RT-duroid-5870-5880-Data-Sheet.pdf*).

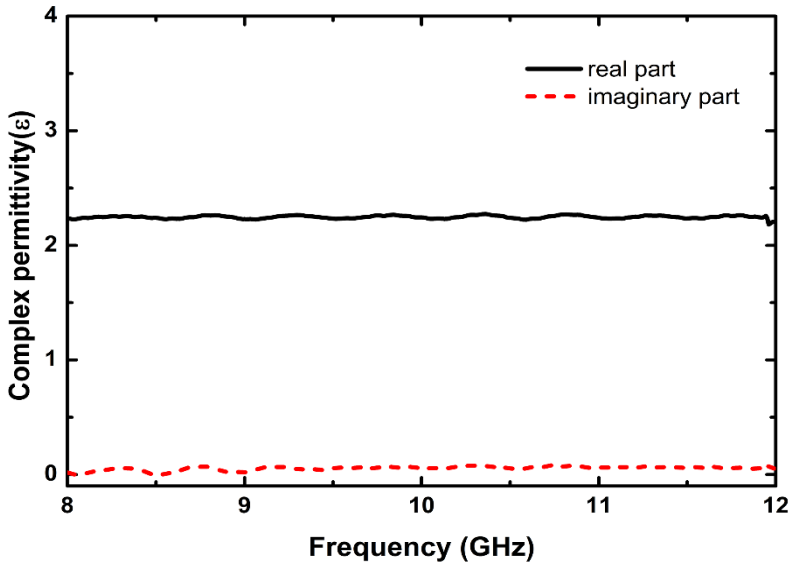

Figure B2: Relative complex permittivity for the Rogers RT/duroid 5880 substrate.

REFERENCES

[1] M. Kubo, X. Li, C. Kim, M. Hashimoto, B. J. Wiley, D. Ham, *et al.*, "Stretchable microfluidic radiofrequency antennas," *Adv Mater*, vol. 22, pp. 2749-52, Jul 6 2010.

[2] F. C. Krebs, S. A. Gevorgyan, and J. Alstrup, "A roll-to-roll process to flexible polymer solar cells: model studies, manufacture and operational stability studies," *Journal of Materials Chemistry*, vol. 19, pp. 5442-5451, 2009.

[3] G. H. Gelinck, H. E. A. Huitema, E. van Veenendaal, E. Cantatore, L. Schrijnemakers, J. B. P. H. van der Putten, *et al.*, "Flexible active-matrix displays and shift registers based on solution-processed organic transistors," *Nat Mater*, vol. 3, pp. 106-110, 02//print 2004.

[4] V. J. Lumelsky, M. S. Shur, and S. Wagner, "Sensitive skin," *IEEE Sensors Journal*, vol. 1, pp. 41-51, 2001.

[5] Y. Zhang, R. Chad Webb, H. Luo, Y. Xue, J. Kurniawan, N. H. Cho, *et al.*, "Theoretical and Experimental Studies of Epidermal Heat Flux Sensors for Measurements of Core Body Temperature," *Advanced Healthcare Materials*, vol. 5, pp. 119-127, 2016.

[6] J. A. Rogers, "Toward Paperlike Displays," *Science*, vol. 291, pp. 1502-1503, 2001-02-23 00:00:00 2001.

[7] Y. Zhang, Y. Huang, and J. A. Rogers, "Mechanics of stretchable batteries and supercapacitors," *Current Opinion in Solid State and Materials Science*, vol. 19, pp. 190-199, 6// 2015.

[8] A. Koh, S. R. Gutbrod, J. D. Meyers, C. Lu, R. C. Webb, G. Shin, *et al.*, "Ultrathin Injectable Sensors of Temperature, Thermal Conductivity, and Heat Capacity for Cardiac Ablation Monitoring," *Advanced Healthcare Materials*, vol. 5, pp. 373-381, 2016.

[9] M. Klopfer, C. Cordonier, K. Inoue, G. P. Li, H. Honma, and M. Bachman, "Flexible, transparent electronics for biomedical applications," in *2013 IEEE 63rd Electronic Components and Technology Conference*, 2013, pp. 494-499.

[10] G. A. Salvatore, M. N, x00Fc, nzenrieder, C. Zysset, T. Kinkeldei, *et al.*, "High performance flexible electronics for biomedical devices," in *2014 36th Annual International Conference of the IEEE Engineering in Medicine and Biology Society*, 2014, pp. 4176-4179.

[11] J. A. Rogers, T. Someya, and Y. Huang, "Materials and mechanics for stretchable electronics," *Science*, vol. 327, pp. 1603-7, Mar 26 2010.

[12] P. Alitalo and S. Tretyakov, "Electromagnetic cloaking with metamaterials," *Materials Today*, vol. 12, pp. 22-29, 3// 2009.

[13] S. Linden, C. Enkrich, M. Wegener, J. Zhou, T. Koschny, and C. M. Soukoulis, "Magnetic Response of Metamaterials at 100 Terahertz," *Science,* vol. 306, pp. 1351-1353, 2004-11-19 00:00:00 2004.

[14] H. Torun, F. Cagri Top, G. Dundar, and A. D. Yalcinkaya, "An antenna-coupled split-ring resonator for biosensing," *Journal of Applied Physics,* vol. 116, p. 124701, 2014.

[15] M. Schueler, C. Mandel, M. Puentes, and R. Jakoby, "Metamaterial Inspired Microwave Sensors," *IEEE Microwave Magazine,* vol. 13, pp. 57-68, 2012.

[16] H.-J. Lee, J.-H. Lee, H.-S. Moon, I.-S. Jang, J.-S. Choi, J.-G. Yook, *et al.*, "A planar split-ring resonator-based microwave biosensor for label-free detection of biomolecules," *Sensors and Actuators B: Chemical,* vol. 169, pp. 26-31, 7/5/ 2012.

[17] I. E. Khodasevych, I. V. Shadrivov, D. A. Powell, W. S. T. Rowe, and A. Mitchell, "Pneumatically switchable graded index metamaterial lens," *Applied Physics Letters,* vol. 102, p. 031904, 2013.

[18] J. B. Pendry, "Negative Refraction Makes a Perfect Lens," *Physical Review Letters,* vol. 85, pp. 3966-3969, 10/30/ 2000.

[19] Z. H. Jiang, S. Yun, F. Toor, D. H. Werner, and T. S. Mayer, "Conformal Dual-Band Near-Perfectly Absorbing Mid-Infrared Metamaterial Coating," *ACS Nano,* vol. 5, pp. 4641-4647, 2011/06/28 2011.

[20] A. M. Hawkes, A. R. Katko, and S. A. Cummer, "A microwave metamaterial with integrated power harvesting functionality," *Applied Physics Letters,* vol. 103, p. 163901, 2013.

[21] R. A. Shelby, D. R. Smith, and S. Schultz, "Experimental Verification of a Negative Index of Refraction," *Science,* vol. 292, pp. 77-79, 2001-04-06 00:00:00 2001.

[22] M. Barbuto, A. Monti, F. Bilotti, and A. Toscano, "Design of a Non-Foster Actively Loaded SRR and Application in Metamaterial-Inspired Components," *IEEE Transactions on Antennas and Propagation,* vol. 61, pp. 1219-1227, 2013.

[23] Y. Yang, X. Zhu, and N. C. Karmakar, "Microstrip lowpass filter based on split ring and complementary split ring resonators," *Microwave and Optical Technology Letters,* vol. 54, pp. 1723-1726, 2012.

[24] K. Fuchi, A. R. Diaz, E. J. Rothwell, R. O. Ouedraogo, and J. Tang, "An origami tunable metamaterial," *Journal of Applied Physics,* vol. 111, p. 084905, 2012.

[25] M. Durán-Sindreu, J. Naqui, J. Bonache, and F. Martín, "Split rings for metamaterial and microwave circuit design: A review of recent developments (Invited paper)," *International Journal of RF and Microwave Computer-Aided Engineering,* vol. 22, pp. 439-458, 2012.

[26] K. Aydin and E. Özbay, "Experimental and numerical analyses of the resonances of split ring resonators," *Physica Status Solidi B-Basic Solid State Physics,* vol. 244, pp. 1197-1201, Apr 2007.

[27] J. D. Baena, J. Bonache, F. Martin, R. M. Sillero, F. Falcone, T. Lopetegi, *et al.*, "Equivalent-circuit models for split-ring resonators and complementary split-ring resonators coupled to planar transmission lines," *IEEE Transactions on Microwave Theory and Techniques,* vol. 53, pp. 1451-1461, Apr 2005.

[28] P. Gay-Balmaz and O. J. F. Martin, "Electromagnetic resonances in individual and coupled split-ring resonators," *Journal of Applied Physics,* vol. 92, pp. 2929-2936, Sep 1 2002.

[29] A. K. Horestani, C. Fumeaux, S. F. Al-Sarawi, and D. Abbott, "Displacement Sensor Based on Diamond-Shaped Tapered Split Ring Resonator," *IEEE Sensors Journal,* vol. 13, pp. 1153-1160, Apr 2013.

[30] P. Liu, S. Yang, A. Jain, Q. Wang, H. Jiang, J. Song, *et al.*, "Tunable meta-atom using liquid metal embedded in stretchable polymer," *Journal of Applied Physics,* vol. 118, p. 014504, 2015.

[31] Y. Huang, Y. Wang, L. Xiao, H. Liu, W. Dong, and Z. Yin, "Microfluidic serpentine antennas with designed mechanical tunability," *Lab on a Chip,* vol. 14, pp. 4205-4212, 2014.

[32] S. Cheng, Z. Wu, P. Hallbjorner, K. Hjort, and A. Rydberg, "Foldable and Stretchable Liquid Metal Planar Inverted Cone Antenna," *IEEE Transactions on Antennas and Propagation,* vol. 57, pp. 3765-3771, 2009.

[33] Y. J. Yoo, H. Y. Zheng, Y. J. Kim, J. Y. Rhee, J.-H. Kang, K. W. Kim, *et al.*, "Flexible and elastic metamaterial absorber for low frequency, based on small-size unit cell," *Applied Physics Letters,* vol. 105, p. 041902, 2014.

[34] P. M. Ragi, K. S. Umadevi, P. Nees, J. Jose, M. V. Keerthy, and V. P. Joseph, "Flexible split-ring resonator metamaterial structure at microwave frequencies," *Microwave and Optical Technology Letters,* vol. 54, pp. 1415-1416, 2012.

[35] W. S. Cai, U. K. Chettiar, A. V. Kildishev, and V. M. Shalaev, "Optical cloaking with metamaterials," *Nature Photonics,* vol. 1, pp. 224-227, Apr 2007.

[36] Z. Jakšić, S. Vuković, J. Matovic, and D. Tanasković, "Negative Refractive Index Metasurfaces for Enhanced Biosensing," *Materials,* vol. 4, p. 1, 2011.

[37] S. Yang, P. Liu, M. Yang, Q. Wang, J. Song, and L. Dong, "From Flexible and Stretchable Meta-Atom to Metamaterial: A Wearable Microwave Meta-Skin with Tunable Frequency Selective and Cloaking Effects," *Scientific Reports,* vol. 6, p. 21921, 02/23/online 2016.

[38] M. Durán-Sindreu, J. Naqui, F. Paredes, J. Bonache, and F. Martín, "Electrically Small Resonators for Planar Metamaterial, Microwave Circuit and Antenna Design: A Comparative Analysis," *Applied Sciences,* vol. 2, p. 375, 2012.

[39] D.-H. Kim and J. A. Rogers, "Stretchable Electronics: Materials Strategies and Devices," *Advanced Materials,* vol. 20, pp. 4887-4892, 2008.

[40] M. Walther, A. Ortner, H. Meier, U. Löffelmann, P. J. Smith, and J. G. Korvink, "Terahertz metamaterials fabricated by inkjet printing," *Applied Physics Letters,* vol. 95, p. 251107, 2009.

[41] H. Tao, C. Bingham, A. Strikwerda, D. Pilon, D. Shrekenhamer, N. Landy, *et al.*, "Highly flexible wide angle of incidence terahertz metamaterial absorber: Design, fabrication, and characterization," *Physical Review B,* vol. 78, 2008.

[42] K. In Kwang and V. V. Varadan, "Flexible isotropic antenna using a split ring resonator on a thin film substrate," in *Antennas and Propagation (APSURSI), 2011 IEEE International Symposium on*, 2011, pp. 3333-3335.

[43] Z. C. Chen, N. R. Han, Z. Y. Pan, Y. D. Gong, T. C. Chong, and M. H. Hong, "Tunable resonance enhancement of multi-layer terahertz metamaterials fabricated by parallel laser micro-lens array lithography on flexible substrates," *Optical Materials Express,* vol. 1, pp. 151-157, Jun 1 2011.

[44] N. R. Han, Z. C. Chen, C. S. Lim, B. Ng, and M. H. Hong, "Broadband multi-layer terahertz metamaterials fabrication and characterization on flexible substrates," *Optics Express,* vol. 19, pp. 6990-6998, Apr 11 2011.

[45] C. M. Shah, S. Sriram, M. Bhaskaran, M. Nasabi, T. G. Nguyen, W. S. T. Rowe, *et al.*, "Elastomer-Based Pneumatic Switch for Radio Frequency Microdevices," *Journal of Microelectromechanical Systems,* vol. 21, pp. 1410-1417, Dec 2012.

[46] S. p. P. Lacour, D. Chan, S. Wagner, T. Li, and Z. Suo, "Mechanisms of reversible stretchability of thin metal films on elastomeric substrates," *Applied Physics Letters,* vol. 88, p. 204103, 2006.

[47] "Sylgard 184 Silicone Elastomer Kit Product Datasheet."

[48] D. Wolfe, D. Qin, and G. Whitesides, "Rapid Prototyping of Microstructures by Soft Lithography for Biotechnology," in *Microengineering in Biotechnology*. vol. 583, M. P. Hughes and K. F. Hoettges, Eds., ed: Humana Press, 2010, pp. 81-107.

[49] S. Walia, C. M. Shah, P. Gutruf, H. Nili, D. R. Chowdhury, W. Withayachumnankul, *et al.*, "Flexible metasurfaces and metamaterials: A review of materials and fabrication processes at micro- and nano-scales," *Applied Physics Reviews,* vol. 2, p. 011303, 2015.

[50] T. Chretiennot, D. Dubuc, and K. Grenier, "A Microwave and Microfluidic Planar Resonator for Efficient and Accurate Complex Permittivity Characterization of Aqueous Solutions," *IEEE Transactions on Microwave Theory and Techniques,* vol. 61, pp. 972-978, 2013.

[51] J. A. Byford, K. Y. Park, and P. Chahal, "Metamaterial inspired periodic structure used for microfluidic sensing," in *Electronic Components and Technology Conference (ECTC) , 2015 IEEE 65th*, 2015, pp. 1997-2002.

[52] T. Chretiennot, D. Dubuc, and K. Grenier, "Double stub resonant biosensor for glucose concentrations quantification of multiple aqueous solutions," in *Microwave Symposium (IMS), 2014 IEEE MTT-S International*, 2014, pp. 1-4.

[53] A. Ebrahimi, W. Withayachumnankul, S. F. Al-Sarawi, and D. Abbott, "Microwave microfluidic sensor for determination of glucose concentration in water," in *Microwave Symposium (MMS), 2015 IEEE 15th Mediterranean*, 2015, pp. 1-3.

[54] S. Koulouridis, G. Kiziltas, Y. J. Zhou, D. J. Hansford, and J. L. Volakis, "Polymer-Ceramic Composites for Microwave Applications: Fabrication and Performance Assessment," *IEEE T. Microw. Theory*, vol. 54, pp. 4202-4208, Dec 2006.

[55] J. Chameswary, L. K. Namitha, M. Brahmakumar, and M. T. Sebastian, "Material Characterization and Microwave Substrate Applications of Alumina-Filled Butyl Rubber Composites," *Int. J. Appl. Ceram. Tec.*, vol. 11, pp. 919-926, Sep-Oct 2014.

[56] Y. Yuan, S. R. Zhang, X. H. Zhou, and E. Z. Li, "$MgTiO_3$ Filled PTFE Composites for Microwave Substrate Applications," *Mater. Chem. Phys.*, vol. 141, pp. 175-179, 8/15/ 2013.

[57] T. Li, J. Chen, H. Dai, D. Liu, H. Xiang, and Z. Chen, "Dielectric Properties of $CaCu_3Ti_4O_{12}$–Silicone Rubber Composites," *J. Mater. Sci.: Mater. Electron.*, vol. 26, pp. 312-316, 2015/01/01 2015.

[58] Y. Yuan, Y. R. Cui, K. T. Wu, Q. Q. Huang, and S. R. Zhang, "TiO_2 and SiO_2 Filled PTFE Composites for Microwave Substrate Applications," *J. Polym. Res.*, vol. 21, p. 366, Jan 31 2014.

[59] K. P. Murali, S. Rajesh, O. Prakash, A. R. Kulkarni, and R. Ratheesh, "Preparation and Properties of Silica Filled PTFE Flexible Laminates for Microwave Circuit Applications," *Compos. Part a-Appl. S.*, vol. 40, pp. 1179-1185, Aug 2009.

[60] Y. C. Chen, H. C. Lin, and Y. D. Lee, "The Effects of Filler Content and Size on the Properties of PTFE/SiO_2 Composites," *J. Polym. Res.-Taiwan*, vol. 10, pp. 247-258, 2003/12/01 2003.

[61] K. P. Murali, S. Rajesh, O. Prakash, A. R. Kulkarni, and R. Ratheesh, "Comparison of Alumina and Magnesia Filled PTFE Composites for Microwave Substrate Applications," *Mater. Chem. Phys.*, vol. 113, pp. 290-295, Jan 15 2009.

[62] L. K. Namitha, J. Chameswary, S. Ananthakumar, and M. T. Sebastian, "Effect of Micro- and Nano-fillers on the Properties of Silicone Rubber-alumina Flexible Microwave Substrate," *Ceram. Int.*, vol. 39, pp. 7077-7087, Aug 2013.

[63] D. H. Im, C. J. Jeon, and E. S. Kim, "$MgTiO_3$/polystyrene composites with low dielectric loss," *Ceramics International*, vol. 38, pp. S191-S195, 2012.

[64] G. Subodh, M. Joseph, P. Mohanan, and M. T. Sebastian, "Low Dielectric Loss Polytetrafluoroethylene/TeO2 Polymer Ceramic Composites," *J. Am. Ceram. Soc.*, vol. 90, pp. 3507-3511, Nov 2007.

[65] L. K. Namitha and M. T. Sebastian, "Microwave dielectric properties of flexible silicone rubber – Ba(Zn1/3Ta2/3)O3 composite substrates," *Materials Research Bulletin*, vol. 48, pp. 4911-4916, 11// 2013.

[66] Y. Hu, Y. Zhang, H. Liu, and D. Zhou, "Microwave Dielectric Properties of PTFE/$CaTiO_3$ Polymer Ceramic Composites," *Ceram. Int.*, vol. 37, pp. 1609-1613, Jul 2011.

[67] T. Hu, J. Juuti, H. Jantunen, and T. Vilkman, "Dielectric properties of BST/polymer composite," *Journal of the European Ceramic Society*, vol. 27, pp. 3997-4001, // 2007.

[68] M. Amjadi, A. Pichitpajongkit, S. Lee, S. Ryu, and I. Park, "Highly Stretchable and Sensitive Strain Sensor Based on Silver Nanowire–Elastomer Nanocomposite," *ACS Nano*, vol. 8, pp. 5154-5163, 2014/05/27 2014.

[69] P. Yi, R. A. Awang, W. S. T. Rowe, K. Kalantar-zadeh, and K. Khoshmanesh, "PDMS Nanocomposites for Heat Transfer Enhancement in Microfluidic Platforms," *Lab. Chip.*, vol. 14, pp. 3419-3426, Sep 7 2014.

[70] M. A. Ali, S. Srivastava, P. R. Solanki, V. Reddy, V. V. Agrawal, C. Kim, *et al.*, "Highly Efficient Bienzyme Functionalized Nanocomposite-Based Microfluidics Biosensor Platform for Biomedical Application," *Sci. Rep.*, vol. 3, p. 2661, 09/27/online 2013.

[71] M. Nour, K. Berean, S. Balendhran, J. Z. Ou, J. Du Plessis, C. McSweeney, *et al.*, "CNT/PDMS Composite Membranes for H_2 and CH_4 Gas Separation," *Int. J. Hydrogen Energ.*, vol. 38, pp. 10494-10501, 8/21/ 2013.

[72] J.-W. Zha, Z.-M. Dang, W.-K. Li, Y.-H. Zhu, and G. Chen, "Effect of Micro-Si_3N_4–Nano-Al_2O_3 Co-filled Particles on Thermal Conductivity, Dielectric and Mechanical Properties of Silicone Rubber Composites," *IEEE T. Dielect. El. In.*, vol. 21, pp. 1989-1996, 2014.

[73] L. Song, A. C. Myers, J. J. Adams, and Y. Zhu, "Stretchable and reversibly deformable radio frequency antennas based on silver nanowires," *ACS Appl Mater Interfaces*, vol. 6, pp. 4248-53, Mar 26 2014.

[74] J. N. Li, C. M. Shah, W. Withayachumnankul, B. S. Y. Ung, A. Mitchell, S. Sriram, *et al.*, "Mechanically tunable terahertz metamaterials," *Applied Physics Letters,* vol. 102, p. 121101, Mar 25 2013.

[75] S. P. Lacour, S. Wagner, Z. Huang, and Z. Suo, "Stretchable gold conductors on elastomeric substrates," *Applied Physics Letters,* vol. 82, pp. 2404-2406, 2003.

[76] M. D. Dickey, "Emerging applications of liquid metals featuring surface oxides," *ACS Appl Mater Interfaces,* vol. 6, pp. 18369-79, Nov 12 2014.

[77] T. Liu, P. Sen, and C.-J. Kim, "Characterization of Nontoxic Liquid-Metal Alloy Galinstan for Applications in Microdevices," *Journal of Microelectromechanical Systems,* vol. 21, pp. 443-450, 2012.

[78] J.-H. So, J. Thelen, A. Qusba, G. J. Hayes, G. Lazzi, and M. D. Dickey, "Reversibly Deformable and Mechanically Tunable Fluidic Antennas," *Advanced Functional Materials,* vol. 19, pp. 3632-3637, 2009.

[79] G. J. Hayes, J. H. So, A. Qusba, M. D. Dickey, and G. Lazzi, "Flexible Liquid Metal Alloy (EGaIn) Microstrip Patch Antenna," *IEEE Transactions on Antennas and Propagation,* vol. 60, pp. 2151-2156, May 2012.

[80] G. Mumcu, A. Dey, and T. Palomo, "Frequency-Agile Bandpass Filters Using Liquid Metal Tunable Broadside Coupled Split Ring Resonators," *IEEE Microwave and Wireless Components Letters,* vol. 23, pp. 187-189, 2013.

[81] M. R. Khan, G. J. Hayes, S. Zhang, M. D. Dickey, and G. Lazzi, "A Pressure Responsive Fluidic Microstrip Open Stub Resonator Using a Liquid Metal Alloy," *IEEE Microwave and Wireless Components Letters,* vol. 22, pp. 577-579, 2012.

[82] K. Aydin and E. Ozbay, "Capacitor-loaded split ring resonators as tunable metamaterial components," *Journal of Applied Physics,* vol. 101, p. 024911, 2007.

[83] T. Hand and S. Cummer, "Characterization of Tunable Metamaterial Elements Using MEMS Switches," *Antennas and Wireless Propagation Letters, IEEE,* vol. 6, pp. 401-404, 2007.

[84] S. Sam and S. Lim, "Tunable Band-Pass Filters Based on Varactor-Loaded Complementary Split-Ring Resonators on Half-Mode Substrate Integrated Waveguide," *Microwave and Optical Technology Letters,* vol. 55, pp. 2458-2460, 2013.

[85] I. Gil, J. Bonache, J. Garcia-Garcia, and F. Martin, "Tunable metamaterial transmission lines based on varactor-loaded split-ring resonators," *Microwave Theory and Techniques, IEEE Transactions on,* vol. 54, pp. 2665-2674, 2006.

[86] A. Velez, J. Bonache, and F. Martin, "Varactor-Loaded Complementary Split Ring Resonators (VLCSRR) and Their Application to Tunable Metamaterial Transmission Lines," *IEEE Microwave and Wireless Components Letters,* vol. 18, pp. 28-30, 2008.

[87] T. Nesimoglu and C. Sabah, "A Tunable Metamaterial Resonator Using Varactor Diodes to Facilitate the Design of Reconfigurable Microwave Circuits," *IEEE Transactions on Circuits and Systems II: Express Briefs,* vol. 63, pp. 89-93, 2016.

[88] S. Zhu, D. G. Holtby, K. L. Ford, A. Tennant, and R. J. Langley, "Compact Low Frequency Varactor Loaded Tunable SRR Antenna," *IEEE Transactions on Antennas and Propagation,* vol. 61, pp. 2301-2304, 2013.

[89] D. Bouyge, A. Crunteanu, A. Pothier, P. O. Martin, P. Blondy, A. Velez, *et al.*, "Reconfigurable 4 pole bandstop filter based on RF-MEMS-loaded split ring resonators," in *Microwave Symposium Digest (MTT), 2010 IEEE MTT-S International*, 2010, pp. 588-591.

[90] B. Pradhan and B. Gupta, "Ka-Band Tunable Filter Using Metamaterials and RF MEMS Varactors," *Journal of Microelectromechanical Systems,* vol. 24, pp. 1453-1461, 2015.

[91] Y. Luo, Z. Han, K. Kikuta, T. Takahashi, A. Hirose, H. Fujita, *et al.*, "An active metamaterials antenna controleld by RF-MEMS switches," in *2015 Transducers - 2015 18th International Conference on Solid-State Sensors, Actuators and Microsystems (TRANSDUCERS)*, 2015, pp. 303-306.

[92] I. V. Shadrivov, D. A. Powell, S. K. Morrison, Y. S. Kivshar, and G. N. Milford, "Scattering of electromagnetic waves in metamaterial superlattices," *Applied Physics Letters,* vol. 90, p. 201919, 2007.

[93] M. Lapine, D. Powell, M. Gorkunov, I. Shadrivov, R. Marqués, and Y. Kivshar, "Structural tunability in metamaterials," *Applied Physics Letters,* vol. 95, p. 084105, 2009.

[94] G. M. Whitesides, "The origins and the future of microfluidics," *Nature,* vol. 442, pp. 368-73, Jul 27 2006.

[95] A. Q. Liu, W. M. Zhu, Q. H. Song, R. F. Huang, S. K. Ting, J. H. Teng, *et al.*, "Microfluidic tunable metamaterial for gigahertz filter array," in *Solid-State Sensors, Actuators and Microsystems (TRANSDUCERS & EUROSENSORS XXVII), 2013 Transducers & Eurosensors XXVII: The 17th International Conference on*, 2013, pp. 2481-2484.

[96] I. E. Khodasevych, W. S. T. Rowe, and A. Mitchell, "Reconfigurable fishnet metamaterial using pneumatic actuation," *Progress In Electromagnetics Research B,* vol. 38, pp. 57-70, 2012.

[97] H.-J. Lee and J.-G. Yook, "Biosensing using split-ring resonators at microwave regime," *Applied Physics Letters,* vol. 92, p. 254103, 2008.

[98] K. Jaruwongrungsee, U. Waiwijit, W. Withayachumnankul, T. Maturos, D. Phokaratkul, A. Tuantranont, *et al.*, "Microfluidic-based Split-Ring-Resonator Sensor for Real-time and Label-free Biosensing," *Procedia Engineering,* vol. 120, pp. 163-166, // 2015.

[99] A. K. Horestani, Z. Shaterian, D. Abbott, and C. Fumeaux, "Application of metamaterial-inspired resonators in compact microwave displacement sensors," in *Microwave Symposium (AMS), 2014 1st Australian*, 2014, pp. 19-20.

[100] M. Labidi, J. B. Tahar, and F. Choubani, "Meta-materials applications in thin-film sensing and sensing liquids properties," *Optics Express,* vol. 19, pp. A733-A739, 2011/07/04 2011.

[101] I. A. I. Al-Naib, C. Jansen, and M. Koch, "Thin-film sensing with planar asymmetric metamaterial resonators," *Applied Physics Letters,* vol. 93, p. 083507, 2008.

[102] R. Melik, E. Unal, N. K. Perkgoz, C. Puttlitz, and H. V. Demir, "Metamaterial-based wireless RF-MEMS strain sensors," in *Sensors, 2010 IEEE*, 2010, pp. 2173-2176.

[103] R. Melik, E. Unal, N. K. Perkgoz, B. Santoni, D. Kamstock, C. Puttlitz, *et al.*, "Nested Metamaterials for Wireless Strain Sensing," *IEEE Journal of Selected Topics in Quantum Electronics,* vol. 16, pp. 450-458, 2010.

[104] H.-J. Lee, H.-S. Lee, K.-H. Yoo, and J.-G. Yook, "DNA sensing using split-ring resonator alone at microwave regime," *Journal of Applied Physics,* vol. 108, p. 014908, 2010.

[105] V. Rawat, S. Dhobale, and S. N. Kale, "Ultra-fast selective sensing of ethanol and petrol using microwave-range metamaterial complementary split-ring resonators," *Journal of Applied Physics,* vol. 116, p. 164106, 2014.

[106] J. A. Gordon, C. L. Holloway, J. Booth, S. Kim, Y. Wang, J. Baker-Jarvis, *et al.*, "Fluid interactions with metafilms/metasurfaces for tuning, sensing, and microwave-assisted chemical processes," *Physical Review B,* vol. 83, p. 205130, 05/25/ 2011.

[107] W. Withayachumnankul, K. Jaruwongrungsee, A. Tuantranont, C. Fumeaux, and D. Abbott, "Metamaterial-based microfluidic sensor for dielectric characterization," *Sensors and Actuators A: Physical,* vol. 189, pp. 233-237, 1/15/ 2013.

[108] A. Ebrahimi, W. Withayachumnankul, S. Al-Sarawi, and D. Abbott, "High-Sensitivity Metamaterial-Inspired Sensor for Microfluidic Dielectric Characterization," *Sensors Journal, IEEE,* vol. 14, pp. 1345-1351, 2014.

[109] A. A. Abduljabar, D. J. Rowe, A. Porch, and D. A. Barrow, "Novel Microwave Microfluidic Sensor Using a Microstrip Split-Ring Resonator," *IEEE Transactions on Microwave Theory and Techniques,* vol. 62, pp. 679-688, 2014.

[110] "Agilent Basics of Measuring the Dielectric Properties of Materials: Application notes.."

[111] S. Jyh, "Comparisons of microwave dielectric property measurements by transmission/reflection techniques and resonance techniques," *Measurement Science and Technology,* vol. 20, p. 042001, 2009.

[112] J. Sheen, "Amendment of cavity perturbation technique for loss tangent measurement at microwave frequencies," *Journal of Applied Physics,* vol. 102, p. 014102, 2007.

[113] J. A. Rogers and R. G. Nuzzo, "Recent progress in soft lithography," *Materials Today,* vol. 8, pp. 50-56, Feb 2005.

[114] H. Tao, J. J. Amsden, A. C. Strikwerda, K. Fan, D. L. Kaplan, X. Zhang, *et al.*, "Metamaterial silk composites at terahertz frequencies," *Advanced materials,* vol. 22, pp. 3527-31, Aug 24 2010.

[115] L. Gao, L. Lin, J. Hao, W. Wang, R. Ma, H. Xu, *et al.*, "Fabrication of split-ring resonators by tilted nanoimprint lithography," *Journal of colloid and interface science,* vol. 360, pp. 320-3, Aug 1 2011.

[116] J. C. McDonald and G. M. Whitesides, "Poly(dimethylsiloxane) as a Material for Fabricating Microfluidic Devices," *Accounts of Chemical Research,* vol. 35, pp. 491-499, 2002/07/01 2002.

[117] T. Weiland, R. Schuhmann, R. B. Greegor, C. G. Parazzoli, A. M. Vetter, D. R. Smith, *et al.*, "Ab initio numerical simulation of left-handed metamaterials: Comparison of calculations and experiments," *Journal of Applied Physics,* vol. 90, pp. 5419-5424, Nov 15 2001.

[118] C. C. Chen, A. Ishikawa, Y. H. Tang, M. H. Shiao, D. P. Tsai, and T. Tanaka, "Uniaxial-isotropic Metamaterials by Three-Dimensional Split-Ring Resonators," *Advanced Optical Materials,* vol. 3, pp. 44-48, Jan 2015.

[119] B. Vasić, M. M. Jakovljević, G. Isić, and R. Gajić, "Tunable metamaterials based on split ring resonators and doped graphene," *Applied Physics Letters,* vol. 103, p. 011102, 2013.

[120] J. B. Pendry, A. J. Holden, D. J. Robbins, and W. J. Stewart, "Magnetism from conductors and enhanced nonlinear phenomena," *IEEE Transactions on Microwave Theory and Techniques,* vol. 47, pp. 2075-2084, Nov 1999.

[121] O. Sydoruk, E. Tatartschuk, E. Shamonina, and L. Solymar, "Analytical formulation for the resonant frequency of split rings," *Journal of Applied Physics,* vol. 105, p. 014903, Jan 1 2009.

[122] K. Aydin, I. Bulu, K. Guven, M. Kafesaki, C. M. Soukoulis, and E. Ozbay, "Investigation of magnetic resonances for different split-ring resonator parameters and designs," *New Journal of Physics,* vol. 7, pp. 168-168, 2005.

[123] M. Shamonin, "Properties of a metamaterial element: Analytical solutions and numerical simulations for a singly split double ring," *Journal of Applied Physics*, vol. 95, p. 3778, 2004.

[124] R. A. Awang, T. Baum, M. Nasabi, S. Sriram, and W. S. T. Rowe, "Mechanically Tolerent Fluidic Split Ring Resonator," *Smart Materials and Structures*, vol. in press, 2016.

[125] J. Z. Bao, M. L. Swicord, and C. C. Davis, "Microwave dielectric characterization of binary mixtures of water, methanol, and ethanol," *The Journal of Chemical Physics*, vol. 104, pp. 4441-4450, 1996.

[126] N. S. Broyles, K. N. E. Verghese, S. V. Davis, H. Li, R. M. Davis, J. J. Lesko, *et al.*, "Fatigue Performance of Carbon fibre/vinyl ester Composites: the Effect of Two Dissimilar Polymeric Sizing Agents," *Polymer*, vol. 39, pp. 3417-3424, Jul 1998.

[127] M. Lin and M. N. Afsar, "A New Cavity Perturbation Technique for Accurate Measurement of Dielectric Parameters," *IEEE MTT.-S. Int. Microw. Symp.*, pp. 1630-1633, 2006.

[128] S. Thomas, V. Deepu, S. Uma, P. Mohanan, J. Philip, and M. T. Sebastian, "Preparation, Characterization and Properties of $Sm_2Si_2O_7$ Loaded Polymer Composites for Microelectronic Applications," *Mater. Sci. Eng. B.-Adv.*, vol. 163, pp. 67-75, 2009.

[129] L. Ramajo, M. Reboredo, and M. Castro, "Dielectric Response and Relaxation Phenomena in Composites of Epoxy Resin with $BaTiO_3$ Particles," *Compos. Part A-Appl. S.*, vol. 36, pp. 1267-1274, 2005.

[130] D. C. Dube, M. T. Lanagan, J. H. Kim, and S. J. Jang, "Dielectric measurements on substrate materials at microwave frequencies using a cavity perturbation technique," *J. Appl. Phys.*, vol. 63, pp. 2466-2468, Apr 1 1988.

[131] Y. Rao, J. Qu, T. Marinis, and C. P. Wong, "A precise numerical prediction of effective dielectric constant for polymer-ceramic composite based on effective-medium theory," *IEEE T. Compon. Pack. T.*, vol. 23, pp. 680-683, 2000.

[132] P. S. Anjana, V. Deepu, S. Uma, P. Mohanan, J. Philip, and M. T. Sebastian, "Dielectric, Thermal, and Mechanical Properties of CeO2-Filled HDPE Composites for Microwave Substrate Applications," *J. Polym. Sci. Pol. Phys.*, vol. 48, pp. 998-1008, May 1 2010.

[133] A. Tropmann, L. Tanguy, P. Koltay, R. Zengerle, and L. Riegger, "Completely Superhydrophobic PDMS Surfaces for Microfluidics," *Langmuir*, vol. 28, pp. 8292-5, Jun 5 2012.

[134] W. Chassé, M. Lang, J.-U. Sommer, and K. Saalwächter, "Cross-Link Density Estimation of PDMS Networks with Precise Consideration of Networks Defects," *Macromolecules*, vol. 45, pp. 899-912, 2012/01/24 2012.

[135] K. J. Berean, J. Z. Ou, M. Nour, M. R. Field, M. M. Y. A. Alsaif, Y. Wang, *et al.*, "Enhanced Gas Permeation through Graphene Nanocomposites," *J. Phys. Chem. C*, vol. 119, pp. 13700-13712, 2015/06/18 2015.

[136] S. H. Yoo, C. Cohen, and C.-Y. Hui, "Mechanical and swelling properties of PDMS interpenetrating polymer networks," *Polymer*, vol. 47, pp. 6226-6235, 8/9/ 2006.

[137] S. Candau, J. Bastide, and M. Delsanti, "Structural, Elastic, and Dynamic Properties of Swollen Polymer Networks," *Adv. Polym. Sci.*, vol. 44, pp. 27-71, 1982.

[138] W. B. Weir, "Automatic measurement of complex dielectric constant and permeability at microwave frequencies," *Proceedings of the IEEE*, vol. 62, pp. 33-36, 1974.

[139] T. Baum, L. Thompson, and K. Ghorbani, "Complex Dielectric Measurements of Forest Fire Ash at X-Band Frequencies," *IEEE Geoscience and Remote Sensing Letters*, vol. 8, pp. 859-863, 2011.

[140] A. M. Nicolson and G. F. Ross, "Measurement of the Intrinsic Properties of Materials by Time-Domain Techniques," *IEEE Transactions on Instrumentation and Measurement*, vol. 19, pp. 377-382, 1970.